A First-Principles Based Multiscale Approach from the Electronic to the Continuum Regime: CO Oxidation at $RuO_2(110)$

vorgelegt von
Diplom-Ingenieur
Sebastian Matera
aus Berlin

Von der Fakultät II - Mathematik und Naturwissenschaften
der Technischen Universität Berlin
zur Erlangung des akademischen Grades
Doktor der Naturwissenschaften
Dr. rer. nat.

genehmigte Dissertation

Promotionsausschuss:

Vorsitzender: Prof. Dr. Mario Dähne
Berichter: Prof. Dr. Eckehard Schöll, PhD
Berichter: Prof. Dr. Karsten Reuter

Tag der wissenschaftlichen Aussprache: 12.11.2010

Berlin 2010

D 83

Abstract

A first-principles based multiscale modeling approach to heterogeneous catalysis is presented, that integrates first-principles kinetic Monte Carlo simulations of the surface reaction chemistry into a fluid dynamical treatment of the macro-scale transport in the reactor. Using the CO oxidation at $RuO_2(110)$ as representative example the relevance of first-principles kinetic Monte Carlo is demonstrated by the comparison with the commonly employed, but less accurate rate equation based approach to surface chemistry. Huge differences between both approaches in the predicted reactivity and qualitatively wrong predictions on the ongoing surface dynamics disqualify the latter approach for the use with first principles input. An efficient general purpose methodology is developed, which allows for simulations of macroscopic catalytic reactors with the same speed as mentioned empirical approaches, but retains the sound electronic basis and the accurate treatment of surface chemistry by kinetic Monte Carlo simulations. As a simple showcase the developed method is applied to stagnation flow fields in front of a $RuO_2(110)$ single crystal surface. The simulation results show how heat and mass transfer effects can readily affect the observed catalytic function at gas-phase conditions typical for modern *in situ* experiments. For a range of gas-phase conditions we furthermore obtain multiple steady-states that arise solely from the coupling of gas-phase transport and surface kinetics. This additional complexity needs to be accounted for when aiming to use dedicated *in situ* experiments to establish an atomic-scale understanding of the function of heterogeneous catalysts at technologically relevant gas-phase conditions.

Zusammenfassung

Ein Multiskalen-Modellierungs-Ansatz basierend auf *ab-initio* Berechnungen für die heterogene Katalyse wird vorgestellt, der “first-principles” kinetische Monte-Carlo-Simulationen für die Oberflächenchemie in eine fluiddynanische Behandlung des makroskopischen Transports im Reaktor integriert. Exemplarisch wird die CO Oxidation an $RuO_2(110)$ betrachtet. Die Relevanz von “first-principles” kinetische Monte-Carlo-Simulationen wird durch den Vergleich mit dem gemeinhin verwendeten, allerdings weniger genauen, ratengleichungsbasierten Zugang für die Oberflächenchemie demonstriert. Große Unterschiede bzgl. der berechneten Reaktivität und eine qualitativ falsche Vorhersage der tatsächlichen Oberflächendynamik machen den letzteren Ansatz untauglich für die Benutzung mit Elektronenstrukturinput. Es wird eine effiziente, allgemein anwendbare Methodik entwickelt, welche es erlaubt, makroskopische, katalytische Reaktoren mit der gleichen Geschwindigkeit wie mit empirischen Ansätzen zu simulieren, wobei allerdings die gut fundierte, elektronische Basis und die akkurate Behandlung der Oberflächenchemie durch kinetische Monte-Carlo-Verfahren beibehalten wird. Als einfaches Beispiel wird die entwickelte Methode auf eine Staupunktströmung gegen eine $RuO_2(110)$-Einkristall-Oberfläche angewendet. Die Simulationsergebnisse zeigen, wie Wärme- und Massentransport die beobachtete katalytische Funktion für Gasphasenbedingungen beeinflussen, die typisch sind für moderne *in situ* Experimente. Desweiteren erhalten wir für einen Bereich von Gasphasenbedingungen mehrere stationäre Zustände, die nur durch die Kopplung von Gasphasentransport und Oberflächenchemie auftreten. Diese zusätzliche Komplexität muss in Betracht gezogen werden, wenn versucht wird durch dedizierte *in situ* Experimente ein atomares Verständnis der heterogenen Katalyse bei technologisch relevanten Gasphasenbedingungen zu etablieren.

Contents

List of Figures

List of Tables

List of Abbreviations

UHV	ultra high vacuum
1p	first principles
MSM	Multiscale Modeling
1p-kMC	first-principles kinetic Monte Carlo
BE	Boltzmann equation
LJ	Lennard-Jones interaction
LMA	Low-Mach-Number Approximation
CTC	continuous temperature condition
BC	boundary condition
NSBC	non-slip boundary condition
TOF	turnover frequency
PK	phenomenological kinetics
kMC	kinetic Monte Carlo
PES	potential energy surface
ME	Master equation
RC	rate constant
DRC	Degree of Rate Control
hTST	harmonic Transition State Theory
TS	transition state
SE	Schrödinger equation
DFT	Density Functional Theory
MFA	mean-field approximation
MaS	majority species
MiS	minority species
MPK	modified phenomenological kinetics
CFD	Computational Fluid Dynamics
RE	rate equation
DAE	differential-algebraic equations
BL	boundary layer

Chapter 1

Introduction

Much of our atomic scale understanding of heterogeneous catalysis stems from ultra high vacuum (UHV) studies of single crystal surfaces [53, 74]. In practice catalysts must contrariwise operate at very different conditions with pressures in the order of atmospheres and elevated temperatures. In order to bridge this “pressure gap” *in situ* techniques have been developed, which are capable to deliver the targeted atomic scale understanding of such model catalysts for technologically relevant gas phase conditions [109]. The focus is on identifying a possibly different surface chemistry, when crossing the “pressure gap”, and on establishing a relation between structure, reactivity, and gas phase conditions. This approach is in some sense half way between surface science, i.e. single crystals in UHV, and the 'real' catalysis with ambient pressures and elevated temperatures, but also with the morphologically much more complex practical catalyst. Due to this complexity at the micro-structural level the targeted structure/reactivity relation is hardly accessible. The concentration on single crystals removes this complexity, thereby (hopefully) enabling a first atomic scale understanding. Yet, other complexities remain; for instance the determination of the reaction mechanism and its kinetic parameters is still a demanding task. Also different from low-conversion operation in UHV is, that in an *in situ* experiment with much higher, achievable conversion rates macroscopic heat and mass transfer effects become increasingly important. This concerns for instance the transport of products away from the active surface or the dissipation of heat generated by exothermic surface reactions. Especially for the often investigated CO oxidation - being the fruit fly of surface science catalysis [31, 28, 30, 47] - high conversions are reported, and mass and heat transfer effects as commonly observed in applied catalysis [24] must also be expected for the single crystal experiments. Being interested in the intrinsic properties of the catalyst we are faced with the fact that mass, heat and momentum transport are strongly influenced by e.g. the reaction chamber geometry or the total throughput rate. Thus most measured quantities in *in situ* experiments will reflect the properties of the combined catalyst-reactor system, not the actual properties of the catalyst itself [78].

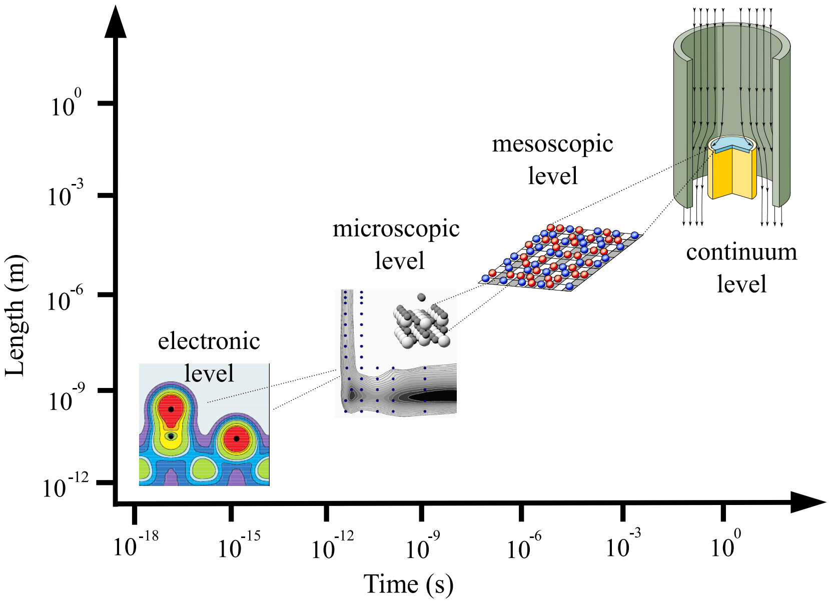

Figure 1.1: The different scales in heterogenous catalysis: At the lowest length and time scales, the electronic level (represented by a electron density plot for co-adsorbed CO and oxygen on a Ru(0001) surface, taken from [108]), the evolution of electrons and nuclei can be described with first-principles electronic structure theories. The next higher scale will be called the microscopic level, where the electronic degrees of freedom are only considered in their average effect on the nuclei (represented by the potential energy plot for the oxygen dissociation on a $RuO_2(110)$ surface, taken from [97]). The motion of the atoms is coarse grained to rare events, i.e. chemical reactions, at the mesoscopic level of description. Here the systems hops from one discrete state to another (represented by a lattice; the balls represent a possible occupation of the (active) lattice site). At the highest here considered length and time scales, in the continuum level, the state of the considered system is described by three-dimensional fields like density or temperature (represented by a sketch of a stagnation flow reactor).

The traditional modeling approach to macroscopic mass, heat and momentum transfer is phenomenological rather than atomistic. The gas phase is described by the Navier-Stokes equations complemented with species and energy balance equations [9]. The surface chemistry is modeled by rate equations[1] [27, 17] based on a more or less guessed reaction mechanism and the kinetic parameters are then fitted to experimental reaction rates. With such a top-down approach one can therefore very efficiently describe the macroscopic behavior of the combined reactor catalyst system, but an atomic scale understanding can not be established in general. Thus we are not much closer to the targeted rational catalyst design than before. In the other extreme and at the lowest relevant length and time scales, see fig. 1.1, we have first principles (1p) approaches, treating the electrons and nuclei explicitly. This kind of modeling definitely allows to tackle the influence of the micro-structure, but mostly on microscopic measures like spectra. Due to the limited size of the systems which can be modeled with such 1p methods, there is no hope that 1p approaches will be ever able to describe macroscopic problems.

Bridging this “theories gap” is highly desirable, promising to combine the atomistic insight by 1p methods with the ability to treat macroscopic transport by continuum mechanics. Such a Multiscale Modeling (MSM) approach is going to be developed in this thesis. Multiscale problems involve a number of different time and length scales, each equipped with their own theory, and the theories are more accurate but also computationally more complex the smaller the scale. Generally a method suitable for a certain scale is cheap compared to the next smaller level, i.e. it allows for the simulation of larger systems compared to the lower levels’ theories, but is very expensive on the next larger level. The idea behind the so-called sequential or hand-shaking approaches in MSM is to obtain the input for each theory from the underlying lower level by appropriate coarse graining, thereby minimizing the necessary low level simulations. Heterogenous (surface) catalysis has an immanent multiscale character, as it is depicted in figure 1.1. At the lowest level, the level of bond making and bond breaking, the motion of even the electrons is resolved. At this electronic level the equation of motion, the quantum mechanical Schrödinger equation, is known and not a single experimental parameter is needed in so-called first principles (ab-initio) electronic structure methods[111]. With the existing first principles methods system sizes up to a few hundred atoms can be tackled on modern parallel computing architectures with sufficient accuracy to yield a predictive-quality for the simulations. Typical time scales for electron dynamics are atto- to femtoseconds. At the next, the microscopic scale the problem is solely described by the motion of the atoms, the electron motion is not considered here. Its effect on the atomic motion is only via the interaction forces between the atoms. In heterogeneous catalysis, especially for the here considered metals, there exist no reliable interaction models, which are able to capture the crucial bond making and bond breaking with sufficient accuracy. Therefore extensive dynamical simulations are prohibitive, since the necessary input from the computationally

---

[1] also often termed phenomenological kinetics in this thesis

much more expensive electronic structure methods needs to be provided 'on the fly'. As this so-called ab-initio Molecular Dynamics [76] can only be applied to relatively small systems, it is hard to access the statistical averages needed as the input for the next larger, mesoscopic scale. In heterogeneous catalysis one therefore needs to resort to approximative methods, which allow to obtain the necessary statistics from just a minimum of information on the interaction between the atoms. Because of this avoidance of detailed microscopic level simulations this approach is often considered as a direct coarse-graining from the electronic to the mesoscopic level. In contrast the existing Force Fields [119] provide a reasonable accuracy in the context of biochemical simulations and can be parametrized beforehand, so that system sizes of millions of atoms can be simulated with the typical time scale for atomic motion in the range of picoseconds to nanoseconds. This allows to obtain the necessary statistics from direct simulations on the microscopic scale. This difference between heterogeneous catalysis and bio-chemistry is one of the reasons why MSM is further developed in the fields of bio- and macro-molecular simulations. Yet, there is another reason for the avoidance of direct microscopic simulations for MSM in heterogeneous catalysis. The barriers between different metastable states are relatively high, in the order of 1 eV. With an average thermal energy per degree of freedom in the order of 1/20 eV a process crossing such a barrier, i.e. a chemical reaction, occurs very rarely and prohibitive long simulations times are needed to obtain the necessary statistics for these rare events. Mostly because of the still short time scales on the microscopic level the continuous atomic motion needs to be further coarse-grained to the rare events. At the mesoscopic level all the detailed motion of the atoms is only considered in its average effect on the rare events. This restriction to rare events allows to account for much longer, often macroscopic times scales. Yet, the typical system size, which can be approached with mesoscopic simulation methods, is still quite limited. At the largest here considered scale, the continuum scale, the atom-resolved description is therefore given up and the state of the system is described by three dimensional continuous fields like temperature and density [114, 126]. The mature computational methods developed for this level allow for the simulation of a whole reaction chamber (or even larger) with a complex geometry and the corresponding long time spans.

In the last years a number of different approaches have been developed bridging the gap(s) between the electronic and the mesoscopic scale. These first principles statistical mechanics techniques range from ab-initio thermodynamics [96] to first-principles based mikrokinetic modeling [83]. Among these modeling approaches latest first-principles kinetic Monte Carlo (1p-kMC) simulations even allow to accurately account for the spatial arrangement and interactions of the adsorbed chemicals [94, 45, 100]. In order to achieve the same predictive-quality description of the detailed surface reaction chemistry as for UHV experiments [95, 99], a technique like 1p-kMC must then be complemented by an appropriate treatment of the macroscopic heat and mass transfer in the gas-surface system. Relatively few approaches exist for such a coupling of the mesoscopic to the continuum level beyond common empirical rate equations. Inderwildi [54] has obtained kinetic parameters from first principles and used them in the otherwise unaltered rate equation approach. Vlachos [118] and Kissel-Osterrieder, Behrendt et al. [62, 7, 61] have developed coupling schemes for the integration of kinetic Monte Carlo and fluid flow simulations, but used empirical mechanisms and kinetic parameters. Majumder and Broadbelt [73] extended the there employed direct coupling methods to two-dimensional problems, but for a generic reaction mechanism[2]. There is not a single study really performing the coarse graining all the way from the lowest electronic to the continuum level.

This is precisely the topic of this work and the focus of this thesis will specifically be on the transition between the mesoscopic and the continuum scale, i.e. to integrate a fully first principles based surface chemistry into a fluid flow simulation. A first-principles treatment of the gas-phase and the solid parts of a reaction chamber is in principle possible, but also needless for the system at hand, since all transport and thermophysical properties have been determined experimentally long before. We will develop this general-purpose methodology using the CO oxidation at a $RuO_2(110)$ surface as a showcase. This reaction is in itself not interesting because of its technological importance; industrial catalysts use different elements for CO oxidation. Still the (0001) face of a ruthenium single crystal shows an interesting behavior, that has attracted a lot of interest in the past. Being hardly active in UHV (compared to other transition metal surfaces) its catalytic function supersedes that of other transition metal surfaces at ambient pressures and elevated temperatures. On explanation is that a thin oxide film develops at the surface under operation conditions, namely a few layers of $RuO_2(110)$. The CO oxidation at $RuO_2(110)$ has therefore been investigated for many years, both experimentally [122, 85] and theoretically [98]. These studies have led to a thorough understanding of the oxide, surface structure and its active sites, as well as to a well established microkinetic model. This makes this system particularly appealing for this project with its focus on the integration of a 1p microkinetic description into a fluid dynamical simulation. We stress that for simplicity we treat the $RuO_2(110)$ surface to be unaffected by the reaction condition, except for the adsorption and desorption of gas phase species and employ the microkinetic model by Reuter and Scheffler for $RuO_2(110)$ throughout[97]. If this oxide can be assumed to be stable under realistic reaction conditions or maybe a different surface termination forms is a highly debated question [41, 86, 42]. Especially at high CO and low oxygen partial pressures the oxide will be reduced, and different models for the structure of the active state during *in situ* operation have been proposed, e.g. the pristine metal surface [87] or a reduced surface oxide [85]. Addressing this stability and the nature of the active surface is a formidable problem of its own, and we will not address it here. Instead we couple the $RuO_2(110)$ surface model into the fluid flow simulations. If future work leads to a new (refined) model, it could equally be integrated into the here developed methodology.

We nevertheless note that in all debates on the active state of the surface

---

[2] The coupling of kMC and fluid flow simulations is maybe a little more spread in modeling of crystal growth, also the extension to two-dimensional problems appeared earlier (see e.g. [56, 117]).

(oxide or not), the important aspect of macroscopic transport was not considered. With the high conversion rates observed in CO oxidation heat and mass transport depend sensitively on reactor geometry and flow conditions. The surface will probably see a very different gas phase in a different reaction chamber, although the same nominal reaction conditions have been applied at the inlet of the reactor. Thus the results obtained from different experimental setups can not be directly compared for such high conversion reactions like CO oxidation at late transition metals. This reactor dependence may possibly account for some of the controversies in the present discussion.

From a theoretical point of view the $RuO_2(110)$ surface exhibits the interesting property of only small lateral interactions, which means there is not thermodynamical driving force for segregation and correlation. The classical mean-field based phenomenological kinetics should work the best for such kind of systems.

The study starts with chapter 2 describing the continuum mechanical foundations for modeling a chemical reactor on a macroscopic scale. In chapter 3 the first principles statistical mechanics approach to surface chemistry is introduced. The mean-field based phenomenological kinetics and kinetic Monte Carlo simulations are compared in both predicted reactivity and rate determining steps. Making use of the Degree of Rate Control [79] we correlate the observed failure of the phenomenological kinetic to the description of certain reaction steps in the rate equations. On basis of this knowledge a modified phenomenological model is developed, that leads to an improved description for some gas phase conditions, but still fails as a universal microkinetic model. In chapter 4 an efficient approach is developed, which allows to integrate 1p-kMC into an existing software environment for the treatment of heat, mass and momentum transfer problems at the continuum level. Making use of the different time and length scales on which mesoscopic surface chemistry and macroscopic gas flow evolve this approach allows to perform flow simulations with nearly no computational overhead compared to the rate equation based approaches while maintaining the physically sound first-principles basis with correct account for the spatial arrangement of adsorbates. In chapter 5 we apply the developed integrated model to a stagnation flow geometry as a representative example for the discussion of transport effects in *in situ* experiments. The effects on the observed catalytic function by the reactor geometry, flow conditions (e.g. the though-put rate) and the degree of heat dissipation through sample and sample holder are investigated in detail. The observed strong deviation from the ideal behavior without transport effects and the dependence on the peculiarities of the reactor geometry and flow conditions are explained in terms of a boundary layer. Based on this boundary layer concept a simplified theory is developed for a rough first estimation of the magnitude of mass and heat transfer effects. The observed bi-stability clearly shows that if these effects are not appropriately accounted for in both experiment and theory, even qualitatively wrong conclusions may easily arise, which then block the envisioned route towards a rational design of future improved catalysts.

Chapter 2

Continuum modeling of the reactor scale

In this chapter we introduce the continuum mechanical model of a catalytic reactor. For this purpose we draw a volume around the reactor (depicted as dashed line in figure 2.1). We choose the volume such that we can provide values for composition, density, temperature and velocity or the corresponding fluxes at its boundaries. We then need a theory for the matter enclosed in this volume. A reaction chamber contains usually a number of different materials. These are the reactor walls, the sample, the sample holder and the gas mixture. Continuum mechanics can generally handle only homogeneous materials, i.e. the material response, e.g. the relation between heat flux and temperature gradient,

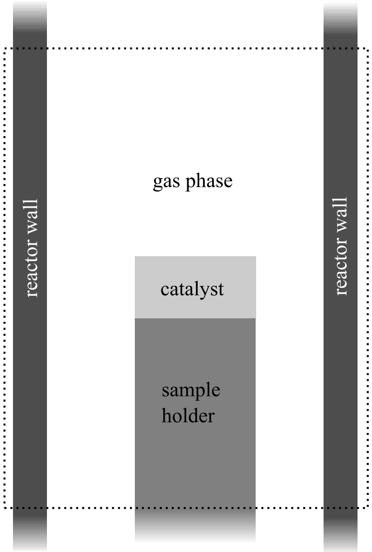

Figure 2.1: Schematic view of a catalytic reactor: The modeled volume (enclosed in the dashed line) contains a number of different materials. These are the gas mixture, the catalyst sample, the reactor walls and the sample holder. Each part needs its own continuum mechanical model. These models need to be complemented by appropriate jump conditions for the investigated fields at the interfaces between different materials.

should not explicitly depend on the position[69]. Therefore the modeled volume needs to be divided into different 3-dimensional spatial regions, each enclosing only one type of material (depicted in figure 2.1 with different gray scales for different solid materials and with white for the gas phase). Within these regions all fields such as density ρ, velocity $\underline{v}$, mass fractions Y^{α}, and temperature T are assumed to be continuous and differentiable. At the interfaces no fields need to be continuous a priori and we must propose so-called jump conditions, which determine the behavior of the fields at the interfaces[125]. For a reactor we therefore need three different kinds of material models, one for the the gas flow, one for the solid bulk materials and one for the reactive catalyst's surface. If more than catalyst bulk is to be modeled, e.g. the sample holder, these parts generally require an independent treatment because they do not obey the same macroscopic material law as the sample, e.g. due to a different thermal conductivity. Note that in this case also a solid/solid interface has to be taken into account in addition to the reactive surface.

We start with the model for the gas mixture and its foundations. The solid phase model, which essentially needs only to allow for heat conduction, is described next. We proceed with the continuum mechanical consideration of a catalytic surface. Starting with suitable balance equations for surfaces we outline the considerations and approximation which lead to practical jump conditions. Finally we present the necessary parameters for the investigated CO oxidation at $RuO_2(110)$.

2.1 Gas flow

In this section we introduce the gas phase model. We introduce the necessary balance equations and motivate the commonly employed diffusion theories from the (rational) theory of mixtures[113, 114]. The gas phase material laws are presented next for a general gas mixture. Finally we introduce the Low-Mach-Number approximation, which is a suitable simplification for the modeling of low velocity reactive flow, and give a summary of the equations of motion for the gas phase transport.

2.1.1 Balance Equations

Modeling on a continuum mechanical basis usually starts with appropriate balance equations, based on the requirement that a quantity Φ (e.g. mass or momentum) is additive on macroscopic length scales. The basic idea in deriving local balance equation is to consider an arbitrary volume V and to express its content and the flux through its boundary in terms of fields. Taking the limit $V \to 0$ and with some other presuppositions the local balance equation reads[69]

$$\frac{\partial}{\partial t}\phi + \nabla \cdot (\phi \underline{v} + \underline{\Upsilon}_{\Phi}) = \sigma_{\Phi}. \qquad (2.1)$$

Here ϕ is the density of Φ. The divergence term represents the flux of Φ trough the boundary of the considered infinitesimal volume $V \to 0$, where $\phi\underline{v}$ is the convective flux and $\underline{\Upsilon}_\Phi$ is the non-convective flux. The source term σ_Φ represents the production and annihilation of Φ within V. Transferring this to the conserved quantities in our context, total mass, total momentum and total energy we arrive at the following balance equations.

Total mass:

$$\frac{\partial}{\partial t}\rho + \nabla \cdot \rho\underline{v} = 0, \tag{2.2}$$

Momentum:

$$\frac{\partial}{\partial t}\rho\underline{v} + \nabla \cdot (\rho\underline{v}\underline{v} - \underline{\underline{T}}) = \rho\underline{g}, \tag{2.3}$$

Total energy:

$$\partial_t\rho(e + \frac{1}{2}v^2) + \nabla \cdot [\rho(e^{+}\frac{1}{2}v^2)\underline{v} - \underline{\underline{T}} \cdot \underline{v} + \underline{q}] = \rho\underline{g} \cdot \underline{v}, \tag{2.4}$$

where $\underline{\underline{T}}$ is the stress tensor, $\underline{g}$ is the gravitational acceleration, e is the specific internal energy, $\underline{q}$ is the heat flux. Note that the only external field we are considering is gravity, else there must be extra source terms in the momentum and energy balances accounting for this. Equations 2.2 to 2.4 are not sufficient for modeling a mixture with N_{spec} constituents, if each species is allowed to move differently. Only the motion of the mixture as a whole is described by the above equations, i.e. we need to complement eq. 2.2 to 2.4 with so-called partial balance equations for the mass, the momentum and the energy of each constituent (for details see Truesdell [114]). For mass and momentum this is straightforward, since the mass and the momentum of a single species are simply the summed up masses and momenta of all molecules of that species. Partial mass and momentum are therefore additive and must obey a separate balance equation. For the partial energy this is not such an easy task, since there might be interactions between different species and a decomposition of the total energy into contributions of different species is not straightforward. However, for gases we are on the safe side, since the interaction energy is negligible and the partial energy is almost exactly given the sum over the energies of the different molecules similar to the case of mass and momentum. We can therefore assign to each species α a mass density ρ^α, a velocity $\underline{v}^\alpha$ and an internal energy e^α. Note that the velocity $\underline{v}^\alpha$ is distinct from the diffusion velocity $\underline{u}^\alpha$ defined by

$$\underline{u}^\alpha = \underline{v}^\alpha - \underline{v} \tag{2.5}$$

The partial balances for the constituent α read

Partial mass:

$$\partial_t \rho^\alpha + \nabla \cdot \rho^\alpha \underline{v}^\alpha = \tau^\alpha \ , \tag{2.6}$$

Partial momentum:

$$\partial_t \rho^\alpha \underline{v}^\alpha + \nabla \cdot [\rho^\alpha \underline{v}^\alpha \underline{v}^\alpha - \underline{\underline{T}}^\alpha] = \rho^\alpha \underline{g} + \underline{b}^\alpha \ , \tag{2.7}$$

Partial energy:

$$\partial_t \rho^\alpha (e^\alpha + \frac{1}{2} v^{\alpha 2}) + \nabla \cdot [\rho^\alpha (e^\alpha + \frac{1}{2} v^{\alpha 2}) \underline{v}^\alpha - \underline{\underline{T}}^\alpha \cdot \underline{v}^\alpha + \underline{q}^\alpha] = \rho^\alpha \underline{g} \cdot \underline{v}^\alpha + \varepsilon^\alpha \tag{2.8}$$

where τ^α is the production of mass by chemical reactions, $\underline{b}^\alpha$ is the interaction force or the production of momentum and ε^α is the production of energy of the constituent α by interaction with other constituents. The partial stress is denoted by $\underline{\underline{T}}^\alpha$ and the partial heat flux by $\underline{q}^\alpha$. The partial mass balance is often written in terms of

$$\text{mass fraction: } Y^\alpha = \frac{\rho^\alpha}{\rho} \text{ and diffusive mass flux: } \underline{j}^\alpha = \rho^\alpha u^\alpha \tag{2.9}$$

instead of partial mass density and diffusion velocity. Summing over all species we must arrive at the equations 2.2-2.4, since total mass, total momentum and total energy must be the sum of their constituent specific counterparts. Thus total and partial balances are linear dependent. The fact, that the total mass, the total momentum and the total energy are conserved, is reflected in the following constraints for the source terms

$$\sum_\alpha^{N_{\text{spec}}} \tau^\alpha = 0, \quad \sum_\alpha^{N_{\text{spec}}} \underline{b}^\alpha = 0, \quad \sum_\alpha^{N_{\text{spec}}} \varepsilon^\alpha = 0. \tag{2.10}$$

Further, it is found that partial and total quantities obey the relations

$$\rho = \sum_\alpha^{N_{\text{spec}}} \rho^\alpha, \tag{2.11}$$

$$\rho \underline{v} = \sum_\alpha^{N_{\text{spec}}} \rho^\alpha \underline{v}^\alpha, \tag{2.12}$$

$$\rho e = \sum_\alpha^{N_{\text{spec}}} \rho^\alpha (e^\alpha + \frac{1}{2} u^{\alpha 2}), \tag{2.13}$$

$$\underline{\underline{T}} = \sum_\alpha^{N_{\text{spec}}} \underline{\underline{T}}^\alpha - \rho^\alpha \underline{u}^\alpha \underline{u}^\alpha, \tag{2.14}$$

$$\underline{q} = \sum_\alpha^{N_{\text{spec}}} \underline{q}^\alpha + \rho^\alpha (e^\alpha + \frac{1}{2} u^{\alpha 2}) \underline{u}^\alpha - \underline{\underline{T}}^\alpha \cdot \underline{u}^\alpha. \tag{2.15}$$

Mass density ρ and momentum density $\rho\underline{v}$ obey the expected sum rules, but internal energy e and stress contain extra terms which are quadratic in the diffusion velocities. Partial mass balances are commonly considered in practice, also termed species balances in chemical engineering[57, 9]. This is not the case for partial momentum and energy balances, the use of which is mostly restricted to theoretical continuum mechanics and non-equilibrium thermodynamics[124, 103, 104, 81]. Consequently the diffusion contributions to internal energy, stress etc. are typically not discussed in standard textbooks[57, 9] on modeling reactive flow.

For heterogeneous catalysis at ambient pressures neglecting the non-linear contributions in the diffusion velocity introduces a negligible error with those extra terms being much smaller than variations in partial internal energy and partial stress. At ambient pressures we have stresses and densities of internal energy in the range of atmospheres. Even with ridiculously high diffusion velocities in the range of m/s these extra terms will not exceed an value of a few Pascal. As a consequence we can use similar sum rules for the stress and the internal energy as for the mass and momentum density. With the same arguments as before we can also remove the non-linear terms in the heat flux in eq. 2.15. For further discussion it is useful to introduce the intrinsic heat flux $\underline{q}_{\mathrm{intr}} = \sum_{\alpha}^{N_{\mathrm{spec}}} \underline{q}^{\alpha}$ [82].

Because of the afore mentioned lack of some partial balances one considers in practice not the full set of partial balances but rather only mass, momentum and energy balance for the whole mixture 2.2-2.4 plus $N_{\mathrm{spec}}-1$ partial mass balances [23]. The total mass balance can obviously replace one partial mass balance due to the linear dependence. Due to the frequent collision between molecules at ambient pressures different species will adapt fast to one common temperature and partial energy balances describing multiple temperatures are simply not necessary. However, why can we drop the partial momentum balances? First we are not only interested in the concentrations of different species but also in their motion. Further the partial momentum density $\rho^{\alpha}\underline{v}^{\alpha}$ is needed in the partial mass balance. Obviously we must assume that the diffusion velocity is a so-called constitutive quantity, that is it is a function of ρ, T, $\underline{v}$ and Y^{α} and their derivatives. More generally constitutive quantities are those fields for which we do not want to establish an equation of motion, and therefore we must assume that they depend on those fields for which we have equations of motion (the so-called basic fields). In order to motivate this simplification we consider the partial momentum balance. Obviously it can not be easily inverted with respect to the diffusion velocities. We want to go a step back and regard the diffusion velocities as basic fields. For a theory appropriate for the here investigated fluid mixtures with such a choice of the basic fields, see Samohyl[102]. We rewrite the partial momentum balance with help of the partial mass balance.

$$\rho^{\alpha}\frac{d^{\alpha}\underline{v}^{\alpha}}{dt} - \nabla\cdot\underline{\underline{T}}^{\alpha} = \underline{c}^{\alpha} + \rho^{\alpha}\underline{g}, \tag{2.16}$$

where the operation $\frac{d^{\alpha}}{dt} = \frac{\partial}{\partial t} + \underline{v}^{\alpha}\cdot\nabla$ is the material time derivative of species

α and so $\frac{d^\alpha \underline{v}^\alpha}{dt}$ is the acceleration of this species[125, 126]. $\underline{c}^\alpha = \underline{b}^\alpha - \tau^\alpha \underline{v}^\alpha$ was introduced for convenience. If we now subtract the balance of total momentum weighted with the appropriate mass fraction we obtain

$$\rho^\alpha \left(\frac{d^\alpha \underline{v}^\alpha}{dt} - \frac{d\underline{v}}{dt}\right) - (\nabla \cdot \underline{\underline{T}}^\alpha - Y^\alpha \nabla \cdot \underline{\underline{T}}) = \underline{c}^\alpha \tag{2.17}$$

where $\frac{d}{dt} = \frac{\partial}{\partial t} + \underline{v} \cdot \nabla$ is the common material derivative of the mixture[69, 57]. At ambient pressure and temperature any extra acceleration of one species relative to the mixture's motion will be strongly damped out and the difference between species' and mixture's acceleration can be neglected compared to the other terms in the above equation. Since the diffusion velocities are usually small we want to assume that the dependence of $\underline{\underline{T}}^\alpha$, $\underline{\underline{T}}$ and $\underline{c}^\alpha$ on $\underline{u}^\alpha$ is linear. As a consequence $\underline{\underline{T}}^\alpha$ and $\underline{\underline{T}}$ can only depend on the gradients or higher derivatives of $\underline{u}^\alpha$[102], which we want to neglect here. By using the decomposition $\underline{c}^\alpha = \underline{\bar{c}}^\alpha + \sum_\beta^{N_\mathrm{spec}-1} B^{\alpha\beta} \underline{u}^\beta$ we arrive at

$$\sum_\beta^{N_\mathrm{spec}-1} B^{\alpha\beta} \underline{u}^\beta = (\nabla \cdot \underline{\underline{T}}^\alpha - Y^\alpha \nabla \cdot \underline{\underline{T}}) - \underline{\bar{c}}^\alpha \tag{2.18}$$

where the right hand side does not depend on $\underline{u}^\beta$. Thus the above equation reduces to a linear set of equations for the diffusion velocities and these can indeed be modeled as constitutive quantities. The typical linear relation between diffusion velocities and the gradients of density, composition and temperature arises, if we can assume that $\underline{\underline{T}}$ and $\underline{\underline{T}}^\alpha$ are simple functions of ρ, Y^α, and T, and a linear dependence of $\underline{\bar{c}}^\alpha$ on the respective gradients. Due to this property of $\underline{u}^\beta$ the balance equations

Total mass:

$$\frac{\partial}{\partial t}\rho + \nabla \cdot \rho \underline{v} = 0, \tag{2.19}$$

Species mass:

$$\frac{\partial}{\partial t} Y^\alpha \rho + \nabla \cdot (Y^\alpha \rho \underline{v} + \underline{j}^\alpha) = \tau^\alpha, \tag{2.20}$$

Momentum:

$$\frac{\partial}{\partial t}\rho \underline{v} + \nabla \cdot (\rho \underline{v}\underline{v} - \underline{\underline{T}}) = \rho \underline{g}, \tag{2.21}$$

Internal energy:

$$\frac{\partial}{\partial t}\rho e + \nabla \cdot [\rho e \underline{v} + \underline{q}] = \underline{\underline{T}} \cdot \cdot \nabla \underline{v}, \tag{2.22}$$

will serve as basis for the equations of motion for the basic fields ρ, $\underline{v}$, T and Y^α ($\alpha \in [1, N_{\text{spec}} - 1]$). Since the diffusion velocities can be modeled as constitutive quantities, they do not need an independent equation of motion but can be determined from the fields.

2.1.2 Constitutive Relations

As mentioned in the last section the balance equations (2.19-2.22) contain more unknown fields than there are balance equations. We must assume that the knowledge of the basic fields (in our case ρ, $\underline{v}$, T and Y^α) allows to completely determine the constitutive quantities (e, $\underline{\underline{T}}$, $\underline{q}$, $\underline{j}^\alpha$, $\underline{\underline{T}}^\alpha$, and τ^α). In principle this can be a functional dependence, where the value of a constitutive quantity at a certain point $\underline{x}$ depends on the values of the basic fields at all other spatial points at the current and all former times. Of course, deriving such a functional relation rigorously is completely hopeless. Rather one will make use of the understanding that at macroscopic length and time scales only the close vicinity of a point $\underline{x}$ and its very recent history will have an influence on the value of the constitutive quantity at this point. Using a suitably truncated Taylor expansion (in space and time) at the point $\underline{x}$ for the basic fields the problem of finding the functional dependence reduces to finding a (constitutive) function with the basic fields and their derivatives (at $\underline{x}$) as arguments. The most applied theories for fluid mixtures can be represented using the state space[23, 9]

$$Z = [\rho, \nabla\rho, \underline{v}, \nabla\underline{v}, T, \nabla T, Y^\alpha, \nabla Y^\alpha], \tag{2.23}$$

that is all constitutive functions are allowed to depend Z. For the very most cases it is sufficient to consider only a linear dependence on the non-scalar quantities in Z. With this state space the requirement, that the constitutive relation must be invariant under a transformation of the frame of reference, the fact, that fluids are isotropic, and the entropy principle (loosely spoken the second law of thermodynamics)[102, 103, 82] lead to the constitutive relations

$$e = e(\rho, T, Y^\alpha) \tag{2.24}$$

$$\underline{\underline{T}} = -p\underline{\underline{1}} + \mu(\nabla\underline{v} + (\nabla\underline{v})^T) - (\frac{2}{3}\mu - \nu)(\nabla \cdot \underline{v})\underline{\underline{1}}, \tag{2.25}$$

$$\underline{\underline{T}}^\alpha = -p^\alpha\underline{\underline{1}} + \mu^\alpha_{\text{mix}}(\nabla\underline{v} + (\nabla\underline{v})^T) - (\frac{2}{3}\mu^\alpha_{\text{mix}} - \nu^\alpha_{\text{mix}})(\nabla \cdot \underline{v})\underline{\underline{1}}, \tag{2.26}$$

$$\underline{q}_{\text{intr}} = -\kappa\nabla T - \kappa_p\nabla p - \sum_\alpha \kappa_\alpha \nabla Y^\alpha \tag{2.27}$$

$$\underline{q} = \underline{q}_{\text{intr}} + \sum_\alpha h^\alpha \underline{j}^\alpha \tag{2.28}$$

$$\underline{j}^\alpha = -\sum_\beta D^{\alpha\beta}\nabla Y^\beta - D^\alpha_T \nabla T - D^\alpha_p \nabla p, \tag{2.29}$$

where we have eliminated all non-linear terms in u^α in the internal energy, total stress and heat flux. Note that the second law of thermodynamics is only needed only for eq. 2.24, where it removed the dependence on $\nabla \cdot \underline{v}$. Due to the linear dependence on all non-scalar fields in Z the scalar coefficients

$$p, p^\alpha, h^\alpha, \mu, \mu^\alpha_{\text{mix}}, \nu, \nu^\alpha_{\text{mix}}, -\kappa, \kappa_p, \kappa^\alpha_Y, D^{\alpha\beta}, D^\alpha_T, D^\alpha_\rho \tag{2.30}$$

solely depend on ρ, T, Y^β. Here p is the total pressure and p^α are the partial pressures, h^α are the specific partial enthalpies and defined by

$$\rho^\alpha h^\alpha = \rho^\alpha e^\alpha + p^\alpha. \tag{2.31}$$

p, p^α, h^α, e, and e^α are called thermophysical quantities. The transport coefficients are the (shear) viscosity μ, the bulk viscosity ν, the thermal (or heat) conductivity κ. We will call $D^{\alpha\beta}$ diffusion coefficient. Since κ^α_Y is connected with composition-gradient driven heat conduction (Dufour effect), it will be called Dufour coefficient. Analogously we will call D^α_T Soret coefficient, because it must be non-zero when we observe thermal-gradient driven diffusion (Ludwig-Soret effect). D^α_p and κ_p will be called pressure diffusion coefficient and pressure conduction coefficient, respectively[1].

Having a closer look at equations 2.15 and 2.28 for the heat flux we can see that the partial stress $\underline{\underline{T}}^\alpha$ in the more general equation 2.15 has been replaced by its velocity independent part $-p^\alpha \underline{\underline{1}}$. Mathematically this is a consequence of the assumed linear relations between heat flux and all derivatives in Z. Since u^α is already proportional to some gradients, the gradient dependent part of $\underline{\underline{T}}^\alpha$ must be neglected. Physically this also makes some sense, since those velocity dependent parts are usually much smaller than the partial pressure. Since the partial stresses occur only in the heat flux, eq. 2.15, we do not need to determine μ^α_{mix} and ν^α_{mix}, but only the partial pressures.

We did not specify the results for the chemical source term τ^α yet. Since we are not going to deal with gas phase chemical conversion in the context of low temperature CO oxidation we can set $\tau^\alpha = 0$. The (continuum mechanical) theory for such source terms is detailed in [102, 114] and the necessary further refinement is discussed in the chemical engineering literature, e.g. [57, 23].

Up to now we have not made use of the fact that we are considering a mixture of gases. The above considerations apply for a fairly large class of fluids and microscopic input was not needed. However, for an equation of motion we need specific formulas for the coefficients, eq. 2.30, describing their dependence on density composition and temperature. This dependence can be measured but already for mixtures with a moderate number of constituents the number of necessary measurements can become tremendously large. In order to overcome these limitations mesoscopic or microscopic theories need to be employed, either to find further constraints complementary to those obtained by continuum mechanics thereby reducing the number of necessary measurements or even to calculate the coefficients, eq. 2.30. For not too dense gases the multi-component

---

[1] Depending on the field there might be different definitions for κ^α_Y, κ_p, D^α_T, and D^α_p and $D^{\alpha\beta}$[9]. The choice made here simply leads to the shortest notation for the equations of motion.

Boltzmann equation (BE)[15, 29] provides an appropriate mesoscopic basis for such a reduction. The BE originates from a coarse-graining of the microscopic Liouville equation[127, 66] and is based on the assumption that the time in which two molecules interact is much shorter than the average time a molecule does not 'feel' the other molecules. The continuous deterministic microscopic motion is then mapped on a mesoscopic level with only free flights and collisions of two molecules that have a zero duration. The collisions need to be modeled stochastically, since we do not follow the microscopic trajectories anymore. As one might expect the balance equations, eq. 2.2-2.4, and the partial balances, e.g. 2.6-2.8, and their relation to each other can exactly be reproduced by manipulating the BE. This is not the case for the constitutive relations 2.24-2.29. The BE describes the statistical behavior of arbitrarily dilute gases. In a very dilute gas collisions will be so rare, that there is hardly any force which leads to a fast decay of the relative motion of different constituents. Yet, this is one of the prerequisites for the validity of the constitutive equations. Therefore the constitutive relations can only be valid in the limit of only moderately diluted gases. In this limit a Chapman-Enskog expansion can be applied[15, 34, 29]. The Chapman-Enskog expansion develops the solutions of the BE in powers of the inverse collision frequency. Since the collision frequency is high for denser gases and low for dilute gases, only the very first terms will be significant in the targeted limit of only moderately diluted gases. For atmospheric pressures and temperature of the order of a few hundred Kelvin only the first two terms are considered[29, 49, 21]. The important general findings are:

- The constitutive quantities obey laws which are special cases of eq. 2.24-2.29. Especially those terms do not appear, which are not linear in diffusion velocities and gradients.
- The whole dependence of the quantities, eq. 2.30, on ρ, T, and Y^α can be determined for a general gas mixture up to a finite set of functions, which solely depend on temperature.
- The interaction between molecules enters only in these functions, which solely depend on temperature.

We will now discuss the more specific results. In the case of no gas-phase chemical reactions partial and total pressure obey the ideal gas law[2].

$$p^\alpha = \frac{Y^\alpha}{m^\alpha}\rho k_\mathrm{B} T, \quad p = \sum_\alpha p^\alpha, \tag{2.32}$$

where m_α is the mass of species α and k_B is the Boltzmann constant. The specific internal energy is given by

$$e = \sum_\beta Y^\beta e^\beta, \tag{2.33}$$

---

[2] Also with gas chemical conversion the validity of the ideal gas law commonly assumed[23]. See [29] for a discussion of this general case in terms of kinetic gas theory and [102] for a continuum mechanical treatment.

where the partial specific internal energy e^α is given by the usual formulas from equilibrium statistical mechanics of gases and is a function of the temperature only [57, 90]. We consider translational, rotational and vibrational degrees of freedom where we treat the first two in the classical limit and latter in the harmonic approximation. This leads to

$$e^\alpha = \frac{1}{m^\alpha}(E_0^\alpha + \frac{3 + N_{\mathrm{rot}}^\alpha}{2}T + \sum_i^{N_{\mathrm{vib}}^\alpha} \frac{x_i^\alpha/Te^{-x_i^\alpha}}{(1-e^{-x_i^\alpha})^2}), \quad x_i^\alpha = \frac{\hbar\omega_i^\alpha}{k_{\mathrm{B}}T} \tag{2.34}$$

where E_0^α is the electronic ground state energy plus zero point energy correction. N_{rot}^α and N_{vib}^α are the number of rotational and vibrational degrees of freedom in a molecule of species α, respectively. ω_i^α is the vibrational frequency of the i-th vibrational mode. With the equations 2.13, 2.31, and 2.34 all remaining thermophysical properties can be obtained

partial isochoric heat capacity

$$c_v^\alpha = \frac{de^\alpha}{dT} \tag{2.35}$$

partial isobaric heat capacity

$$c_p^\alpha = \frac{dh^\alpha}{dT} \tag{2.36}$$

mixture's isochoric heat capacity

$$c_v = \sum_\beta Y^\beta c_v^\beta \tag{2.37}$$

mixture's isobaric heat capacity

$$c_p = \sum_\beta Y^\beta c_p^\beta \tag{2.38}$$

mixture's enthalpy

$$h = \sum_\beta Y^\beta h^\beta \tag{2.39}$$

In general the transport coefficients, eq. 2.30, need to be determined by solving a linear system [15, 49, 29]. This most exact treatment can be found in [29]. We will instead adapt an approach also used by the Computational Fluid Dynamics program **COYOTE**[18]. We will apply the common approximate mixture averaged formulas[57, 9] for the viscosity and the thermal conductivity, and the Stefan-Maxwell equations for determining the transport coefficients for the mass fluxes, eq. 2.29. This provides a sufficiently accurate description for the purposes we are interested in.

For the shear viscosity μ we make thus use of the semi-empirical Wilke's law [123, 9]

$$\mu = \sum_{\alpha} \frac{X^{\alpha} \mu^{\alpha}}{\sum\limits_{\beta} X^{\beta} \Phi^{\alpha\beta}}, \tag{2.40}$$

with

$$\Phi^{\alpha\beta} = \frac{(1 + (\frac{\mu^{\alpha}}{\mu^{\beta}})^{1/2} (\frac{M^{\beta}}{M^{\alpha}})^{1/4})^2}{8^{1/2} (1 + \frac{M^{\alpha}}{M^{\beta}})^{1/2}}, \tag{2.41}$$

where μ^{α} is the pure species' viscosity, X^{α} is the mole fraction, and M^{α} is the molar mass. Note that the pure species' viscosity μ^{α} is different from the viscosity $\mu^{\alpha}_{\text{mix}}$ entering the partial stress. While the former is connected with the total stress response of a pure gas with the only constituent α present, the latter is oppositely connected with the partial stress response of the species α in a general mixture of gases. Thus μ^{α} is independent of composition by definition, while $\mu^{\alpha}_{\text{mix}}$ will depend on composition in general. From kinetic theory the pure species' viscosity is given by

$$\mu^{\alpha} = \frac{5 k_{\text{B}}}{16\sqrt{\pi}} \; \frac{m^{\alpha} T}{\Omega^{(2,2)}_{\alpha\alpha}(T)} \quad , \tag{2.42}$$

with a so-called collision integral $\Omega^{(2,2)}_{\alpha\alpha}(T)$, which depends solely on temperature. The interaction between gas phase molecules enters only here. The bulk viscosity ν is commonly set to zero, which is exact in the case of mono-atomic gases, but only approximate in the case of polyatomic molecules [23]. Although the bulk viscosity is often even higher than the shear viscosity, this approximation can mostly be applied without introducing a intolerable error. The bulk viscosity only contributes to the isotropic part of the stress (those terms which are proportional to the unit tensor), this part is dominated by the total pressure which is much larger than the term involving the bulk viscosity as long the velocity gradient is not extremely large.

For the thermal conductivity κ we employ a law similar to Wilke's law [9]

$$\kappa = \sum_{\alpha} \frac{X^{\alpha} \kappa^{\alpha}}{\sum\limits_{\beta} X^{\beta} \Phi^{\alpha\beta}} \tag{2.43}$$

where $\Phi^{\alpha\beta}$ is the same as in Wilke's law. The pure species conductivities κ^{α} ($\neq \kappa^{\alpha}_{\text{mix}}$ similar to the case of the viscosities) are obtained from the viscosities and heat capacities via the Eucken correction[34, 9]

$$\kappa^{\alpha} = (c^{\alpha}_{p} + \frac{5}{4} \frac{k_{\text{B}}}{m^{\alpha}}) \mu^{\alpha}. \tag{2.44}$$

The other coefficients in the equation for the intrinsic heat flux will be set to zero. Dufour effect and pressure conduction are commonly regarded to have a negligible influence in reactive flow calculations and therefore $\kappa_p = 0$ and $\kappa_Y^\alpha = 0$ is widely employed[23, 9].

We eliminate the diffusive mass fluxes with the help of the Stefan-Maxwell equations

$$\sum_\beta \frac{RT}{D_{\text{bin}}^{\alpha\beta}} \left[\frac{X^\alpha}{M^\beta} \underline{j}^\beta - \frac{X^\beta}{M^\alpha} \underline{j}^\alpha \right] = p \nabla X^\alpha + (X^\alpha - Y^\alpha) \nabla p + \frac{\chi^\alpha}{T} \nabla T, \tag{2.45}$$

where R is the ideal gas constant, the $D_{\text{bin}}^{\alpha\beta}$ are the binary diffusion coefficients and χ^α the coefficient of thermal diffusion.

$$D_{\text{bin}}^{\alpha\beta} = \frac{3}{16} \left(\frac{2k_{\text{B}}^3}{\pi} \right)^{1/2} \frac{\left[T^3 \left(\frac{m^\alpha + m^\beta}{m^\alpha m^\beta} \right) \right]^{1/2}}{p \Omega_{\alpha\beta}^{(1,1)}(T)} \quad , \tag{2.46}$$

The Stefan-Maxwell equations are used to determine the diffusion, the pressure diffusion and the Soret coefficients. Thermal diffusion is usually so small that it needs only to be considered for very light species like hydrogen. Additionally there exists no established formula for it, so that the full linear implicit problem arising from the Chapman-Enskog theory needs to be solved. In the present context we will neglect this effect and set $\chi^\alpha = 0$[9], which leads to $D_T^\alpha = 0$.

For the pure species viscosities μ^α and binary diffusion coefficients $D_{\text{bin}}^{\alpha\beta}$ we employ the common semi-empirical approach[57] based on Lennard-Jones (LJ) type interactions

$$V^{\alpha\beta}(r) = 4\epsilon^{\alpha\beta} \left[\left(\frac{\sigma^{\alpha\beta}}{r} \right)^{12} - \left(\frac{\sigma^{\alpha\beta}}{r} \right)^{6} \right], \tag{2.47}$$

with the potential $V^{\alpha\beta}(r)$ for the interaction of two molecules of type α and β, respectively. Here r is the intermolecular distance, and $\epsilon^{\alpha\beta}$ and $\sigma^{\alpha\beta}$ are the LJ parameters. The real interaction potential will be different, especially since the investigated molecules are not spherical and have internal degrees of freedom. Choosing a LJ model must therefore be seen as a convenient way of representing the temperature dependence of the transport coefficients. For a LJ gas the collision integrals reduce to

$$\begin{aligned} \frac{\Omega_{\alpha\beta}^{(1,1)}(T)}{(\sigma^{\alpha\beta})^2} &= \Omega^{(1,1)*}(T^{\alpha\beta}) \approx 0.0548 (T^{\alpha\beta})^{-0.15504} + (T^{\alpha\beta} + 0.55909)^{-2.1705}, \\ \frac{\Omega_{\alpha\alpha}^{(2,2)}(T)}{(\sigma^{\alpha\alpha})^2} &= \Omega^{(1,1)*}(T^{\alpha\alpha}) \approx 1.147 (T^{\alpha\alpha})^{-0.145} + (T^{\alpha\alpha} + 0.5)^2, \\ &\text{with: } T^{\alpha\beta} = \frac{k_{\text{B}} T}{\epsilon^{\alpha\beta}}. \end{aligned} \tag{2.48}$$

The LJ-parameters for pure substances are tabulated[18, 59, 25]. The lacking interaction parameters for unlike molecules are approximated with the common semi-empirical combination rules[57]

$$\sigma_{\alpha\beta} = (\sigma_\alpha + \sigma_\beta)/2, \quad \epsilon^{\alpha\beta} = \sqrt{\epsilon_\alpha \epsilon_\beta} \tag{2.49}$$

for non-polar molecules.

2.1.3 Low-Mach-Number Approximation

In practice it is often useful to work in the so-called Low-Mach-Number approximation (LMA)[72, 2]. It is a good working assumption, when the flow velocity is small. In the case of a zero velocity in the whole domain the total pressure will be constant in space. Therefore in the case of small velocities the spatial variations of the total pressure $\tilde{p}$ - called dynamic pressure - will be much smaller than its absolute value. We set

$$p(\underline{x}, t) = p_{\mathrm{ref}}(t) + \tilde{p}(\underline{x}, t) \tag{2.50}$$

where $p_{\mathrm{ref}}(t)$ is a reference pressure measured somewhere in the reaction chamber, e.g. at the inlet. All spatial variations of the total pressure need to be accounted for by the dynamic pressure. The order of magnitude of the dynamic pressure can estimated using Bernoulli's law. It turns out that for the pressure and the velocity range considered in this study the dynamic pressure is orders of magnitude smaller that the reference pressure. Thus we can determine the density from the applied total pressure $p_{\mathrm{ref}}(t)$. Since the density is not determined by the continuity equation anymore the small dynamic pressure must be introduced as a dynamic variable, i.e. it is not determined by the constitutive relation eq. 2.32, but needs to be adapted so that mass and momentum balances are fulfilled. The formal expansion in powers of the Mach-Number - the fraction of the maximal flow velocity and the speed of sound - shows that the gradient of the dynamic pressure can be neglected in all equations except the momentum balance.

The advantage of the LMA is that acoustic, high frequency and small length scale pressure modes are filtered out while still treating those aspects accurately which are important for the time and length scales of flow and transport. This eases the numerical simulation substantially, because the intrinsic stiffness of the fully compressible formulation stemming from the different time and length scales for acoustic waves and flow, respectively, has been removed.

Within the LMA the equations describing transient flow and transport in the gas phase read

Mass

$$\frac{\partial}{\partial t}\rho + \nabla \cdot \rho \underline{v} = 0 \tag{2.51}$$

Partial mass

$$\rho\frac{\partial}{\partial t}Y^\alpha + \rho\underline{v}\cdot\nabla Y^\alpha - \sum_\beta \nabla\cdot D^{\alpha\beta}\nabla Y^\beta = 0, \tag{2.52}$$

Momentum

$$\rho\frac{\partial}{\partial t}\underline{v} + \rho\underline{v}\nabla\cdot\underline{v} + \nabla\tilde{p} - \nabla\cdot\mu(\nabla\underline{v} + (\nabla\underline{v})^T) - \nabla\frac{2}{3}\mu\nabla\cdot\underline{v} = \rho\underline{g}, \tag{2.53}$$

Enthalpy

$$\rho\frac{\partial}{\partial t}h + \rho\underline{v}\cdot\nabla h - \nabla\cdot\kappa\nabla T - \nabla\cdot\sum_{\beta\alpha} h^\alpha D^{\alpha\beta}\nabla Y^\beta] = \frac{\partial}{\partial t}p_{\text{ref}}, \tag{2.54}$$

LMA

$$\nabla p_{\text{ref}} = \nabla\sum_\alpha \frac{Y^\alpha}{m^\alpha}\rho k_{\text{B}}T = 0 \tag{2.55}$$

where the dissipation function $\Phi = (\underline{\underline{T}} + p_{\text{ref}})\cdot\cdot\nabla\underline{v}$ has been set to zero on the right hand side of the enthalpy equation. This term represents the viscous dissipation of kinetic energy into thermal energy. In a flow with moderate streaming velocities we expect only a negligible heat up due to viscous forces and neglecting this term is reasonable in this regime[57].

2.2 Heat Transport in the Solid

The continuum mechanical model for the solid parts of the reaction chamber will in principle be posed in a similar way as for the gas phase. However here this procedure is much simplified as we want to assume that the solid parts of the reactor remain undeformed and in the same phase, so that only heat conduction has to be modeled. With the help of Fourier's law for the heat flux $\underline{q}_{\text{solid}} = -\kappa_{\text{solid}}\nabla T_{\text{solid}}$ the balance of energy then reads

$$\rho c_{p,\text{solid}}\partial_t T_{\text{solid}} - \nabla\cdot\kappa_{\text{solid}}\nabla T_{\text{solid}} = 0, \tag{2.56}$$

where T_{solid} is the temperature in the solid and $c_{p,\text{solid}}$ and κ_{solid} are the corresponding heat capacity and thermal conductivity, resp.. For the studied cases we can safely assume a constant value for the heat conductivity. While sample holder and reactor wall are probably polycrystalline and therefore isotropic, the sample is a single crystal, which is anisotropic. For such a material the heat conductivity is in general a tensor, not scalar as in 2.56 [69]. We will nevertheless stick to the isotropic model for simplicity, in particular as the details of the model for the heat transport in the solid part do not affect the here considered cases (as discussed in more detail in section 5.3.3).

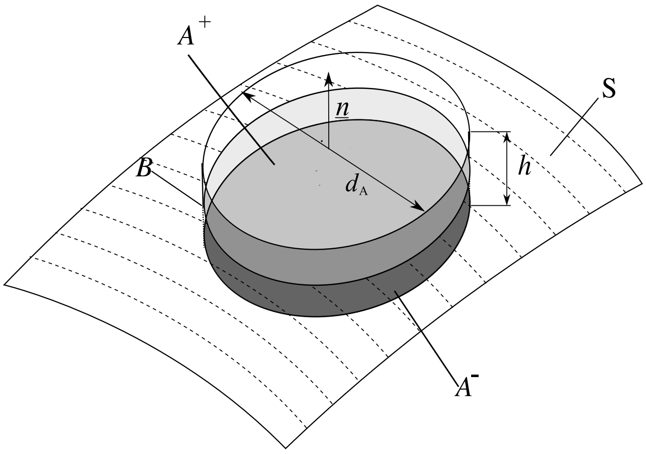

Figure 2.2: Macroscopically the catalytic surface can be considered as a two dimensional manifold having zero volumetric extension. An infinitesimal surface element can microscopically be represented by a small pill box. The height h is much smaller that the diameter d_A of the two parallel faces A^+ (transparent circle) and A^- (dark gray), facing gas and solid phase, resp.. Thus the area of the wall B is negligible compared to that of A^+ and A^-. The normal vector $\underline{n}$ perpendicular to A^+ and A^- is pointing into the gas phase. It is oriented in such a way that the phase boundary S (hatched area), the actual catalytic surface, is never cutting the A^+ and A^-.

2.3 The Catalyst's Surface

At the interface between the gas and the catalyst, the fields can a priori not be considered continuous and differentiable. As example might serve the density of gaseous species which is finite in the gas phase regime and zero in the solid. In order to describe the change between the different regimes the interface region between catalyst and gas phase needs to be considered as a two dimensional manifold although it has a microscopically three dimensional character. In figure 2.2 a schematic view on the surface is shown. An infinitesimal surface element is a small pillbox with the top A^+ facing the gas phase and the bottom A^- in contact with the solid phase. Both are parallel to the actual phase boundary S. The unit normal vector $\underline{n}$ is defined to point into the gas phase. The area of the cylinder wall B is supposed to be much smaller than the area of A^+ and A^-. In other words the height h of the cylinder is supposed to be much smaller than the diameter d_A of $A^{+/-}$. Since $A^{+/-}$ are already infinitesimal small in the continuum sense, the volume of such a pillbox effectively tends to zero on the scale where the continuum models for the gas and the solid phase are applicable. Nevertheless the continuum models for the gas and the solid need to be valid approximations at A^+ and A^- where the interface region faces these two phases and h must stay finite on a microscopic (or better mesoscopic) scale. When for instance a gaseous molecule approaches the surface the interaction with this will dominate those interactions with other molecules. The continuum model for the gas phase, solely based on intermolecular interactions, is therefore not a sufficient description. The two dimensional treatment of the interface region has the consequence that the balance equations formulated for such a singular surface have the form of jump conditions for the fluxes, such as heat flux or stress in the gas and the catalyst.

2.3.1 Balance equations

The general continuum mechanical theory of surfaces is extensively explained in refs. [82, 126, 39]. Due to the finite extension h of the interface region we must assume that both gaseous species and catalyst material are present there. Additionally there will be species which exist only on the surface of the catalyst. These are the adsorbed gas phase species, where we have the freedom of choice to define a surface species appropriately for modeling purposes. So we can for instance attribute all adsorbed CO molecules to one single surface species or split this group so that not only the molecule but also the adsorption site it sticks to defines a surface species. We want to assume that the macroscopic motion of such adsorbed species can be neglected due to their binding to the surface. We denote their number with M_{spec}, so that we have $N_{\text{spec}} + M_{\text{spec}} + 1$ different species in the interface. We denote the partial mass density per surface area by $\hat{\rho}^\alpha$ for all three kinds of species. We use the convention

- catalyst: $\alpha = 0$
- gaseous species : $\alpha \in [1, N_{\text{spec}}]$
- surface species: $\alpha \in [N_{\text{spec}} + 1, N_{\text{spec}} + M_{\text{spec}}]$
- total: $\hat{\rho} = \sum_{\alpha=0}^{N_{\text{spec}}+M_{\text{spec}}} \hat{\rho}^\alpha$

All fields defined in the interface will carry a hat. Due to its small perpendicular extension h tangential transport in the surface (through the wall B) is usually negligible compared to what enters and leaves the surface region through its two normal faces A^+ and A^-. That is we do not need to introduce surface diffusive fluxes, surface heat fluxes etc.. When the surface is at rest the (partial) mass balances at a point $\underline{x}_s$ of the surface reduce to

$$\frac{\partial}{\partial t}\hat{\rho}^\alpha = 0, \;\; \alpha = 0 \tag{2.57}$$

$$\frac{\partial}{\partial t}\hat{\rho}^\alpha - \hat{r}^\alpha = -(\rho Y^\alpha \underline{v} + \underline{j}^\alpha) \cdot \underline{n}, \;\; \alpha \in [1, N_{\text{spec}}] \tag{2.58}$$

$$\frac{\partial}{\partial t}\hat{\rho}^\alpha - \hat{r}^\alpha = 0, \;\; \alpha \in [N_{\text{spec}} + 1, N_{\text{spec}} + M_{\text{spec}} + 1] \tag{2.59}$$

$$\frac{\partial}{\partial t}\hat{\rho} = -\rho \underline{v} \cdot \underline{n} \tag{2.60}$$

with the chemical source terms $\hat{r}^\alpha$ of the constituent α. The right hand side of eqn. 2.57-2.60 represents the flux of the balanced matter (partial or total) through the face A^+. The requirement of mass conservation in every single reaction leads to[114, 82]

$$\hat{r}^\alpha = \sum_{K}^{N_{\mathrm{reac}}} m^\alpha \nu_K^\alpha s_K \tag{2.61}$$

where ν_K^α are the stoichiometric coefficients in the Kth reaction and s_K is the corresponding reaction rate given in number of reaction events per time and surface area. Note that we define stoichiometric coefficients by writing the reaction equation for the Kth reaction in the form

$$(-\nu_K^{\mathrm{A}})\mathrm{A} + (-\nu_K^{\mathrm{B}})\mathrm{B} \ldots \rightarrow \nu_K^{\mathrm{C}}\mathrm{C} + \nu_K^{\mathrm{D}}\mathrm{D} \ldots \tag{2.62}$$

so that stoichiometric coefficients for reactants are negative and positive for products. With the mixture velocity $\underline{\hat{v}}$ in the interface the balance of total momentum reads

$$\frac{\partial}{\partial t}\hat{\rho}\underline{\hat{v}} - \hat{\rho}\underline{g} = (-\rho\underline{v}\,\underline{v} + \underline{\underline{T}}) \cdot \underline{n} - \underline{\underline{T}}_{\mathrm{solid}} \cdot \underline{n}. \tag{2.63}$$

The right hand side represents the flux of momentum through the faces A^+ and A^-. Note that the interface momentum balance depends on the stress in the catalyst at the interface $\underline{\underline{T}}_{\mathrm{solid}}$. Since we do not treat the deformation of the catalyst we do not model momentum transport in the solid and thus we have no means to determine the solid stress. We introduce it because it will be used later for the manipulation of the energy balance in order to reduce its complexity. Neglecting tangential transport the balance of total energy reads

$$\frac{\partial}{\partial t}\hat{\rho}(\hat{e} + \frac{1}{2}\hat{v}^2) - \hat{r} - \hat{\rho}\underline{g} \cdot \underline{\hat{v}} = -[\rho(e + \frac{1}{2}v^2)\underline{v} - \underline{\underline{T}} \cdot \underline{v} + \underline{q}] \cdot \underline{n} + \underline{q}_{\mathrm{solid}} \cdot \underline{n} \tag{2.64}$$

with the mixtures' internal energy $\hat{e}$. Similar as for mass and momentum balances the right hand side represents the flux of energy through the top and the bottom face of the considered infinitesimal pillbox. Then the energy balance can be converted into a balance for the enthalpy by formally introducing surface pressures

$$\begin{aligned} \frac{\partial}{\partial t}\hat{\rho}\hat{h} - \frac{\partial}{\partial t}\hat{p} - \hat{r} &= \\ -[\rho e\underline{v} - \underline{\underline{T}} \cdot \underline{v} + \underline{q}] \cdot \underline{n} + \underline{q}_{\mathrm{solid}} \cdot \underline{n} & \\ -[\frac{1}{2}\rho v^2\underline{v} + \frac{1}{2}\rho\hat{v}^2\underline{v} - \rho\underline{v}\,\underline{v} \cdot \underline{\hat{v}}] \cdot \underline{n} + \underline{\hat{v}} \cdot [\underline{\underline{T}} - \underline{\underline{T}}_{\mathrm{solid}}] \cdot \underline{n} & \end{aligned} \tag{2.65}$$

Again we can assume that the quadratic term in the diffusion velocities for the internal energy is negligible. The partial and total enthalpy for the surface can then conveniently be defined

$$\hat{\rho}^\alpha \hat{h}^\alpha = \hat{\rho}^\alpha \hat{e}^\alpha + \hat{p}^\alpha \tag{2.66}$$

$$\hat{\rho}\hat{h} = \sum_\alpha \hat{\rho}^\alpha \hat{h}^\alpha \tag{2.67}$$

$$\hat{p} = \sum_\alpha \hat{p}^\alpha \tag{2.68}$$

where $\hat{e}^\alpha$ is the partial specific internal energy for a surface and $\hat{p}^\alpha$ is a surface partial pressure[3] We have assumed that the total energy can be decomposed into single component contributions, as we did for the gas phase. For the gaseous surface species this can be justified, since the interaction energy with the other constituents - also in the surface area - is small. For the surface species this can be done in a straightforward way if lateral interactions are negligible. If lateral interaction are present such a decomposition might still be possible but the partial internal energies will then also depend on the (microscopic) distribution of the adsorbates and will thereby not be independent of composition. We want to define the catalyst's partial internal energy to be independent of the adsorbed species. Thus all the interaction energy between adsorbed species and the catalyst is assigned to the surfaces species' energies. With these considerations we can write the balance of enthalpy

$$\begin{aligned}
&\sum_{\alpha=0}^{N_{\text{spec}}+M_{\text{spec}}} \left[\hat{\rho}^\alpha \frac{\partial}{\partial t}\hat{h}^\alpha + \hat{h}^\alpha \hat{\tau}^\alpha\right] - \frac{d}{dt}\hat{p} - \hat{r} = \\
&\sum_{\alpha=1}^{N_{\text{spec}}} \hat{h}^\alpha (\rho Y^\alpha \underline{v} + \underline{j}^\alpha) \cdot \underline{n} \\
&- [\rho e \underline{v} - \underline{\underline{T}} \cdot \underline{v} + \underline{q}] \cdot \underline{n} + \underline{q}_{\text{solid}} \cdot \underline{n} \\
&- [\frac{1}{2}\rho v^2 \underline{v} + \frac{1}{2}\rho \hat{v}^2 \underline{v} - \rho \underline{v}\underline{v} \cdot \underline{\hat{v}}] \cdot \underline{n} \\
&+ \underline{\hat{v}} \cdot [\underline{\underline{T}} - \underline{\underline{T}}_{\text{solid}}] \cdot \underline{n}
\end{aligned} \tag{2.69}$$

where we have made use of the partial mass balances. As already mentioned the interface region is a thin shell with vanishing thickness and hardly any material is in the surface. Thus all terms proportional to the partial mass densities tend to zero. The time derivative for the gaseous species in the corresponding mass balance 2.58 can also be dropped, it will be vanishing compared to the chemical source term and the flux of species through the boundary A^+. The mass balance for the surface species can not be further simplified, since the time derivative needs to balance the chemical source terms. Next we want to connect the fields only defined on the surface like $\underline{\hat{v}}$ or $\hat{h}^\alpha$ with those in the two bulk phases. Microscopically we have some freedom to define the thickness of the interface

---

[3] We have termed $\hat{p}^\alpha$ a pressure because of the analogy with the bulk gas phase, but $\hat{p}^\alpha$ has not the physical dimension of a pressure. It should no be mixed up with p_{s}^α, which is the gas phase pressure at the surface used later in this study

region and we can not really distinguish whether a gaseous particle must be assigned to the surface or to the gas phase. We must assume that the statistical properties of gaseous species are continuous when a gaseous particle enters the interface region. Given a point $\underline{x}_s$ on the singular surface used for modeling the interface region we have that partial (specific) internal energy and species velocity in the interface and in the gas phase at $\underline{x}_s$ are identical. If we define the surface pressures for gaseous species according to

$$\frac{\hat{p}^\alpha}{\hat{\rho}^\alpha}(\underline{x}_s) = \frac{p^\alpha}{\rho^\alpha}(\underline{x}_s),\ \alpha \in [1, N_{\text{spec}}] \tag{2.70}$$

this holds also for the enthalpies. From this definition we can see that the surface pressure $\hat{p}^\alpha$ carries a factor $\hat{\rho}^\alpha$ similar as p^α carries a factor ρ^α. If we define the surface pressures of the other components of the surface to be zero we can neglect the time derivative of the total pressure in the surface enthalpy balance. For the same reasons we could neglect the time derivative in the mass balances of gaseous species. The surface species can be regarded to have a vanishing velocity, which is a rather good approximation due to the binding between surface species and catalyst. Since the gas phase species have a zero surface mass density compared to the catalyst and the surface species, the mixture velocity of the surface is approximately zero and we can write down for the point $\underline{x}_s$

$$\hat{\underline{v}}(\underline{x}_s) = 0 \tag{2.71}$$

$$\hat{h}^\alpha(\underline{x}_s) = h^\alpha(\underline{x}_s),\ \alpha \in [1, N_{\text{spec}}] \tag{2.72}$$

and the balance equations reduce to

$$\hat{\tau}^\alpha = (\rho Y^\alpha \underline{v} + \underline{j}^\alpha) \cdot \underline{n},\ \alpha \in [1, N_{\text{spec}}] \tag{2.73}$$

$$\frac{\partial}{\partial t}\hat{\rho}^\alpha - \hat{\tau}^\alpha = 0,\ \alpha \in [N_{\text{spec}} + 1, N_{\text{spec}} + M_{\text{spec}} + 1] \tag{2.74}$$

$$\sum_{\alpha=1}^{N_{\text{spec}}} \hat{\tau}^\alpha = \rho \underline{v} \cdot \underline{n} \tag{2.75}$$

$$0 = (\underline{\underline{T}} - \underline{\underline{T}}_{\text{solid}} \cdot)\underline{n} \tag{2.76}$$

$$\sum_{\alpha=1}^{N_{\text{spec}}} h^\alpha \hat{\tau}^\alpha + \sum_{\alpha=N_{\text{spec}}+1}^{N_{\text{spec}}+M_{\text{spec}}} \hat{h}^\alpha \hat{\tau}^\alpha - \hat{r} = \sum_{\alpha=1}^{N_{\text{spec}}} h^\alpha \underline{j}^\alpha \cdot \underline{n} - [\underline{q} - \underline{q}_{\text{solid}}] \cdot \underline{n}, \tag{2.77}$$

where we have made use of the constitutive relation for the stress 2.25 and neglected the terms $\underline{n} \cdot (\underline{\underline{T}} + p\underline{\underline{1}}) \cdot \underline{v}$ and $\frac{1}{2}\rho v^2 \underline{v} \cdot \underline{n}$. These terms represent the transport of energy into the interface by mechanical work due to viscous stress and the flow of kinetic energy, resp.. Both are usually negligible compared to the heat flux. Equations 2.73 to 2.77 are popular jump (boundary) conditions employed in practical flow modeling[7, 20]. Note that the only surface fields we are left to determine are the reaction rates s_K, $\hat{h}^\alpha$ for the surface species and the the radiative heat source $\hat{r}$.

A very important special case is a stationary interface, for which all time derivatives in 2.73 to 2.74 vanish. As a consequence we do not need to consider the enthalpies of the surface species, but only those of gas phase species.

$$\hat{r}^{\alpha} = -\underline{j}^{\alpha} \cdot \underline{n},\ \ \alpha \in [1, N_{\mathrm{spec}}] \tag{2.78}$$

$$\hat{r}^{\alpha} = 0,\ \ \alpha \in [N_{\mathrm{spec}} + 1, N_{\mathrm{spec}} + M_{\mathrm{spec}} + 1] \tag{2.79}$$

$$0 = \underline{v} \cdot \underline{n} \tag{2.80}$$

$$0 = (\underline{\underline{T}} - \underline{\underline{T}}_{\mathrm{solid}} \cdot)\underline{n} \tag{2.81}$$

$$\hat{r} = [\underline{q} - \underline{q}_{\mathrm{solid}}] \cdot \underline{n}, \tag{2.82}$$

Under stationary operating conditions the normal component of the velocity is zero at the surface, else mass would accumulate in the interface. Having no convective transport at the interface the only way of energy exchange between gas phase and interface can only be due to heat conduction and diffusion and the heat flux from the catalyst and the heat flux from the gas phase must balance with the heat loss or gain due to radiation. There is no explicit term accounting for the heat of reaction, since this is the balance of total energy and includes of course the formation energy of the constituents. Total energy is conserved and the effect of reaction heat is included in the diffusion dependence of the gaseous heat flux. The jump conditions 2.78-2.82 can often also be applied to transient problems, which is the so-called quasi (or pseudo)-stationary approximation[23]. This can be done when the time scales on which the bulk phases (gas and catalyst) evolve are much longer than the time scale on which the surface relaxes to a steady state. This approximation can be motivated with the small normal spatial extension of the interface. The interface can be regarded as microscopic (mesoscopic) and we can hope that the afore mentioned separation of time scales prevails.

2.3.2 Closure

The balances provide jump conditions for the diffusive mass fluxes, the normal component of the velocity and for the heat fluxes in the solid and the gas phase. Since we model the heat conduction also in the catalyst, we need a second jump condition, so that we have one jump condition for each phase. The common assumption is that the temperature is continuous at the interface and we will also employ this in the following

$$T(\underline{x}_s) = T_{\mathrm{solid}}(\underline{x}_{\mathrm{s}}) \tag{2.83}$$

This continuous temperature condition (CTC) should be rather well ensured due to the frequent gas-surface collisions, which should lead to a rapid equilibration of the two different temperatures of both phases. What remains is a boundary condition (BC) for the tangential components of the gas phase mixture velocity. The momentum balance can not serve for this purpose, since we do not consider the momentum transport in the catalyst and we lack the solid stress. Even if we would, we gain nothing, since then two jump conditions are needed similar to the case of heat conduction. The required extra condition is the so-called non-slip boundary condition (NSBC) which assumes that the tangential velocities of the two phase match at the interface

$$(\underline{v}_{\mathrm{solid}} - \underline{v}) \cdot (\underline{\underline{1}} - \underline{nn}) = 0 \tag{2.84}$$

where $\underline{v}_{\mathrm{solid}}$ is the velocity of the catalyst. Since the catalyst is at rest and does not deform its velocity is zero. Thus we have a zero tangential velocity of the gas phase at the interface. The normal component is only zero in the stationary case and in the quasi-stationary approximation. Else it can be determined by equation 2.75.

The CTC and NSBC are more or less ad hoc assumptions having a by far weaker physical basis than the jump conditions based on balance equations. When one of these conditions is violated it needs to be replaced by appropriate partial balance equations. It is useful to consider solely the gaseous species in the surface area and write down the balances for 'gaseous' momentum and 'gaseous' energy (enthalpy)

$$\frac{\partial}{\partial t}\hat{\rho}_{\mathrm{g}}\hat{\underline{v}}_{\mathrm{g}} - \hat{\rho}_{\mathrm{g}}\underline{g} - \hat{\underline{S}}_{\mathrm{g}} = (-\rho\underline{vv} + \underline{\underline{T}}) \cdot \underline{n} \tag{2.85}$$

$$\sum_{\alpha=1}^{N_{\mathrm{spec}}} h^{\alpha}\hat{r}^{\alpha} - \hat{r}_{\mathrm{g}} - \hat{W}_{\mathrm{g}} = \left(\sum_{\alpha=1}^{N_{\mathrm{spec}}} h^{\alpha}\underline{j}^{\alpha} - \underline{q}\right) \cdot \underline{n}, \tag{2.86}$$

where both equations are obtained by summing over the partial balances of the gaseous species in the surface. Since more than only gaseous species are present in the surface the source terms associated with momentum and energy transfer between the different constituents do not sum up to zero. The resulting $\hat{\underline{S}}_{\mathrm{g}}$ and $\hat{W}_{\mathrm{g}}$ are the rates for momentum and energy transfer from the solid and surface to the gaseous species, respectively. Having a clear physical meaning that arises directly from the underlying balance equation, these two quantities have the drawback, that they are hardly accessible on microscopic scale and the phenomenological approach can not reduce their complex dependence enough so that these complex functions can be determined with a limited number of measurements. Due to these limitation we will remain within the CTC and NSBC in the rest of the manuscript.

What remains are the reaction rates and the radiation source. The former will be considered in detail in the following chapters. The radiation source is commonly modeled by a Stefan-Boltzmann type law [7]

$$\hat{r} = \varepsilon\sigma_{\mathrm{Stefan}}(T_{\mathrm{surf}}^4 - T_{\mathrm{ref}}^4). \tag{2.87}$$

σ_{Stefan} is the Stefan-Boltzmann constant and $0 < \varepsilon < 1$ is the emissivity. We will set the radiative source term to zero, since it is simply negligible compared to the heat fluxes at the temperatures we are interested in. Assuming the surface to be a black body ($\varepsilon = 1$) and setting $T_{\mathrm{ref}} = 0$ and $T_{\mathrm{surf}} = 600K$ we find that $\hat{r} \approx 6000\ \mathrm{Js^{-1}m^{-2}}$, which is definitely an upper limit for the radiation

Table 2.1: Material parameters for the gas-phase species: Characteristic diameter σ and energy ϵ, as well as vibrational frequencies ω and zero Kelvin component of the specific internal energy E_0^α (which includes the zero-point energy contribution). The latter is referenced as usual with respect to the standard state of the atomic species, i.e. gas-phase oxygen and solid graphite for O and C, respectively.

		O_2	CO	CO_2	
σ	(Å)	3.458	3.652	3.769	[18]
ϵ/k_B	(K)	107.4	98.1	245.3	[18]
$\hbar\omega$	(meV)	196	269	291, 167, 83 (2x)	[68]
E_0^α	(eV)	0	-1.179	-4.074	[110]

source at this surface temperature. We compare this value with the heat flux in Ruthenium when we have a temperature gradient of 1 K/mm. For such a gradient one can usually skip the energy balance and set the surface temperature to the value of the backside of the sample, which is usually not more than a millimeter thick. Thus this choice for the temperature gradient means that we have chosen a relatively small heat flux, leading to no severe temperature difference between the two faces of the catalyst. Already with this choice we find that $\underline{q}_{\text{solid}} \cdot \underline{n} \approx 10^5$ $\text{Js}^{-1}\text{m}^{-2}$. Thus we expect, that the much smaller radiation source will have no significant effect. But different from the heat flux, which in principle can become arbitrarily large, the radiative source always stays bounded. For the cases where the energy balance matters, i.e. large heat fluxes, the radiation source is in relation even smaller. With the emissivity being in the range of a few per cent for polished materials and single crystal facets being the optimum of polishing, the radiative source becomes a further order of magnitude smaller and the neglect of radiative emission becomes even better founded.

2.4 Stationary CO oxidation at $RuO_2(110)$

For the application to the CO oxidation we want to model a gas mixture consisting purely of O_2, CO and CO_2 in steady-state. For these three species we need the effective LJ parameters $\sigma^{\alpha\alpha}$ and $\epsilon^{\alpha\alpha}$ which can be found in data bases for reactive flow simulations[18, 25, 59]. In addition we need their vibrational frequencies and the zero Kelvin value for their partial internal energies, which can be easily obtained from thermochemical and spectroscopic tables[110, 68]. The parameters employed in this thesis are compiled in table 2.1.

Note that the parameters for the internal energies can also easily be obtained from first principles. Especially for the considered small molecules high level quantum chemical methods can be applied and these deliver the required parameters with a high accuracy[84]. Nevertheless for O_2, CO, and CO_2 zero Kelvin energies and vibrational frequencies have been determined experimentally before and resorting to ab initio calculations is not necessary. This might be different if highly reactive gas phase species exist and the experimental determination is laborious or even impossible. Then first principles calculations might offer a way to determine the lacking information.

In the case of stationary CO oxidation there is no net flux into or out of the surface caused by pure ad/desorption processes. Therefore

$$\mathrm{CO} + \frac{1}{2}\mathrm{O_2} \rightleftharpoons \mathrm{CO_2} \tag{2.88}$$

is the only overall reaction which leads to a net consumption of gas phase CO and O_2. We will call the reaction rate for this reaction the turnover frequency (TOF) in the following. The above reaction scheme implies the stoichiometric coefficients are

$$\nu^{\mathrm{CO}} = -1,\ \nu^{\mathrm{O_2}} = -\frac{1}{2},\ \nu^{\mathrm{CO_2}} = 1 \tag{2.89}$$

For the stationary case we also need the heat conductivity of the sample. An experimental value for bulk RuO_2 is $\kappa_{\mathrm{solid(RuO_2)}}$= 0.50 W cm^{-1} K^{-1}[33]. However, almost all *in situ* work on RuO_2(110) has in fact been performed on ultra-thin films grown on Ru crystals, which would suggest that the value $\kappa_{\mathrm{solid(Ru)}}$= 1.17 W cm^{-1} K^{-1}[67] is more appropriate. Fortunately, for the results reported below it makes no difference which value for this quantity is used.

Chapter 3

Mesoscopic Surface Model

In this chapter the first principles statistical mechanics approach for the modeling of the surface reactions is introduced. We start in section 3.1 with the probabilistic lattice model of a stable single crystal surface. How to relate this model to the underlying microscopic dynamics and the determination of the necessary kinetic parameters from first principles is explained in section 3.2. The employed microkinetic model[1] for CO oxidation at $RuO_2(110)$ by Reuter and Scheffler[97] is specified in section 3.2. We proceed with the two extremes for the solution of the mesoscopic model, the approximate phenomenological kinetics (PK) and the in principle exact kinetic Monte Carlo (kMC) method in section 3.4. The findings of both methods are compared with respect to their predictions for the steady-state total rate of CO conversion, i.e. the turnover frequency (TOF), for the same microkinetic model. The success and failure of the approximate PK is analyzed in terms of rate-determining steps. The influence of the rate-determining steps is thereby determined by calculating the Degree of Rate Control. On the basis of our findings we modify the PK model in order to incorporate the local arrangement of the adsorbates, and arrive at a quantitative description for the regime of high oxygen coverage, where the classical kinetics failed.

3.1 Probabilistic description of surface kinetics

For modeling the chemical kinetics the continuous molecular motion has to be coarse-grained, i.e. we introduce discrete, rare chemical reactions that bring the system from one metastable state to the other. In this mesoscopic description the state - called meso-state in the following - of the modeled system is given by the currently occupied local minimum of the potential energy surface (PES). The object of modeling is thus to predict the evolution of meso-states visited by

---

[1] Here a microkinetic model means a reaction mechanism and the necessary kinetic parameters. The commonly employed rate equations are not included in a microkinetic model, different from the common phrasing in chemical engineering.

the system, i.e. a sequence of chemical reactions. Having this sequence we can calculate the macroscopic reaction rates needed for the continuum mechanical model. Within the basin around every minimum the (vibrational) motion is only treated in a thermally averaged way. Every trajectory, which is assigned to a certain meso-state at time t, will leave the assigned area of the phase space at a different time and maybe to a different meso-state. Since this detailed information is not available in the coarse-grained description we can not know for sure which meso-state follows on the actual one and at which time the transition takes place. The equation representing the meso-scale must therefore account for stochastic dynamics. Generally any kind of coarse-graining leads to a non-deterministic time-evolution due to the restriction to a reduced amount of information[43, 127], regardless if the underlying level can be described deterministic or not. A central point of coarse-graining is therefore to choose the modeled amount of information, such that the mesoscopic stochastic dynamics can be described by equations accessible to simulation and the needed input can be obtained by a limited number of simulations on the microscopic scale. Thus the desired information (in our case the reaction rates in eq. 2.61) sometimes needs to be extended to extra observables (which local minima are visited). The coarse graining to the local minima of the PES has the advantage that the transitions from one meso-state to another, i.e. chemical reaction steps, are rare events. For a rare event the time, in which the it takes place, is much shorter than the time for which the meso-state stays unchanged. That is the average thermal energy per degree of freedom must be low compared to the energy needed to leave the currently occupied basin. Vibrational motion within one local minimum takes place on a faster time scale as a chemical reaction or rare event. Thus there are many oscillations before the next rare event. These vibrations before the next reaction cause the system to forget its former meso-states and the transition to a new meso-state depends only on the currently occupied minimum. As a consequence the changing between the meso-states can be regarded as Markov process[38].

In case of the strong chemisorption of relevance for CO oxidation adsorbates will not be in a random position but will only stick to certain adsorption sites[116]. It is then more or less natural to define a meso-state by the adsorbate occupation of each site on the surface, i.e. which kind of surface species is currently occupying a certain site. Hence the meso-state of the surface in this model can be mapped on the vector

$$\mathbf{x} = (x_1, x_2, \ldots) \tag{3.1}$$

where each component is assigned to one single site and the value of this component denotes the adsorbate state of this site. Thus the the entry x_i labels if the site i is empty or which surface species is adsorbed. Also more complex scenarios are possible, e.g. a molecule could possibly bind with its different terminations to an adsorption site. A mesoscopic model could account for that by introducing one or more adsorbate states for the same molecule, each assigned to a different binding situation. The probability of finding the system in the meso-state $\mathbf{x}$ at the time t will be denoted with

$$P(\mathbf{x}, t). \tag{3.2}$$

Since we deal with Markov processes the probability $P(\mathbf{x}, t)$ obeys the Master equation (ME) [38, 115]

$$\frac{\partial}{\partial t} P(\mathbf{x}, t) = \sum_{\mathbf{y}} W(\mathbf{x}|\mathbf{y}, t) P(\mathbf{y}, t) - \sum_{\mathbf{y}} W(\mathbf{y}|\mathbf{x}, t) P(\mathbf{x}, t), \tag{3.3}$$

where $W(\mathbf{x}|\mathbf{y}, t)$ is the rate constant (RC) for the transition from $\mathbf{y}$ to $\mathbf{x}$. The RC $W(\mathbf{x}|\mathbf{y}, t)$ is also often termed transition probability [38] or rate [97], which is easily mixed up with the macroscopic rate s_K (see equation 2.61), which is the number of chemical reactions actually taking place per unit time and surface area. The latter quantity is an expectation value and depends therefore on $P(\mathbf{x})$, in contrast to a rate constant. Formally the rate constants are defined by [38, 115]

$$W(\mathbf{x}|\mathbf{y}, t) = \lim_{\Delta t \to 0} \frac{p(\mathbf{x}, t + \Delta t|\mathbf{y}, t)}{\Delta t}. \tag{3.4}$$

The conditional probability $p(\mathbf{x}, t'|\mathbf{y}, t)$ describes how likely it is to find the surface in state $\mathbf{x}$ at a time t', when it was in the state $\mathbf{y}$ at a former time t.

3.1.1 Single and Two Site Reactions

On a surface a chemical reaction will only change the adsorbate state of a very few sites. A process which changes the adsorbate state of N sites will be called a N site process or a N site reaction. In this study we will restrict to single and two site reactions. This reduces the number of nonzero RCs tremendously. There are no two reactions taking place at the same time and eq. 3.4 therefore gives $W(\mathbf{x}|\mathbf{y}, t) = 0$, when $\mathbf{x}$ and $\mathbf{y}$ differ in more than two entries. Furthermore, in this work we will not consider lateral interactions. Since all energetics must enter the ME by the RCs, this can only mean that the RC for a given process is independent of those adsorbate states, which do not change during the reaction. With these premises the RCs will have the structure

$$\begin{aligned} W(\mathbf{x}|\mathbf{y}, t) = & \sum_i W_i(x_i|y_i, t) \prod_{l \neq i} \delta_{x_l y_l} \\ & + \frac{1}{2} \sum_{i \neq j} W_{ij}(x_i, x_j|y_i, y_j, t) \prod_{l \neq i,j} \delta_{x_l y_l}, \end{aligned} \tag{3.5}$$

where the first term represents single site events and the second two site events. If lateral interaction would come into play, $W_i(x_i|y_i, t)$ and $W_{ij}(x_i, x_j|y_i, y_j, t)$ would also depend on $y_l,\ l \neq i, j$. We define the reduced probabilities

$$\Pi_i(x_i, t) = \sum_{\{x_l | l \neq i\}} P(\mathbf{x}, t), \tag{3.6}$$

$$\Pi_{ij}(x_i, x_j, t) = \sum_{\{x_l | l \neq i,j\}} P(\mathbf{x}, t), \tag{3.7}$$

where the first is the probability of finding site i in the adsorbate state x_i. In a more chemical language this is the coverage of site i with the 'species' x_i. In equation 3.7 $\Pi_{ij}(x_i, x_j, t)$ is the joint probability of finding x_i at site i and x_j at site j. We will call this two site or pair probability in the following.

From the master equation 3.3 and the structure of the RCs in eq. 3.5 we find for the coverages

$$\begin{aligned}
&\frac{\partial}{\partial t}\Pi_k(x_k,t) = \\
&\quad \sum_{y_k} W_k(x_k|y_k,t)\Pi_k(y_k,t) - \sum_{y_k} W_k(y_k|x_k,t)\Pi_k(x_k,t) \\
&\sum_j \sum_{x_j y_j y_k} W_{kj}(x_k,x_j|y_k,y_j,t)\Pi_{kj}(y_k,y_j,t) \\
&\quad -\sum_j \sum_{x_j z_j z_k} W_{kj}(z_k,z_j|x_k,x_j,t)\Pi_{kj}(x_k,x_j,t).
\end{aligned} \tag{3.8}$$

which easily obtained by summing over all x_i except for x_k. Leaving out a further x_l in the summation we arrive at an equation for the two site probabilities.

In the following we will consider only nearest neighbor reactions and presume that all sites can be grouped by their type of site a. Further we restrict to homogeneous problems, i.e. the system is translationally invariant. That is the coverages $\Pi_k(x_k, t)$ depend only on the type a of the site k not on its actual position. Therefore all coverages for different sites are identical as long the sites are of the same type. Correspondingly the RCs $W_{kj}(x_k, x_j|y_k, y_j, t)$ will also depend only on the relative position of sites i and j and on its arguments of course. With a and b denoting the type of site for i resp. j we can set $W_{kj}(x_k, x_j|y_k, y_j, t) = w_{ab}(C, D|A, B, t)$, when i and j are nearest neighbors and $x_k = C$, $x_j = D$, $y_k = A$, and $y_j = B$. All other $W_{kj}(x_k, x_j|y_k, y_j, t)$ will be zero due to the restriction to nearest neighbor processes. Since the number of different types of sites should be small, independently of the total number of sites, the number of independent RCs $w_{ab}(C, D|A, B, t)$ is small and does not depend on the system size. In the coverage $P_a(A, t)$ the index a will denote the type of site and A the adsorbate state.

$$P_a(A,t) = \Pi_k(x_k,t) \tag{3.9}$$

when the site k has the type a and we can assign x_k to A. Similarly to the coverages for the pair probabilities the absolute position of the two involved sites is not important anymore, only their relative position and their types. Since we restrict to nearest neighbor reactions only nearest neighbor pair probabilities will occur in the equation for the coverages. We denote the probability of finding species A at site of type a and species B at a neighboring site of type b with $P_{ab}(A, B, t)$. Similarly to the coverages

$$P_{ab}(A,B,t) = \Pi_{kj}(x_k,x_j,t) \tag{3.10}$$

when the sites i and k are nearest neighbors and we can assign x_k to A and x_j to B. Equation 3.8 can then be reduced to

$$\begin{aligned} &\frac{\partial}{\partial t} P_a(A,t) = \\ &\quad \sum_B w_a(A|B,t)P_a(B,t) - \sum_B w_a(B|A,t)P_a(A,t) \\ &\quad + \sum_{bBCD} N_b^a w_{ab}(A,B|D,C,t)P_{ab}(D,C,t) \\ &\quad - \sum_{bBCD} N_b^a w_{ab}(D,C|A,B,t)P_{ab}(A,B,t), \end{aligned} \tag{3.11}$$

where N_b^a is the number of nearest neighbor sites of type b around an a-site. Note if we define b not by the type of site, but by its relative position to the site a, next nearest neighbor reactions and a directional dependence of the RCs are easily included.

3.1.2 Reaction Rates

Up to now we have introduced coverages, pair probabilities and rate constants. We did not show how these are related to the macroscopic reaction rates. For that we consider the mass balance for surface species eq. 2.59 with the requirement of mass conservation in every reaction eq. 2.61

$$\frac{\partial}{\partial t}\hat{\rho}^{\alpha} = \sum_{K}^{N_{\mathrm{reac}}} m_{\mathrm{s}}^{\alpha} \nu_K^{\alpha} s_K \tag{3.12}$$

If we define a surface species by the adsorbate type A and the site type a it sticks to and if we denote this species with $\mathrm{A_a}$, the relation

$$\hat{\rho}_{\mathrm{s}}^{A_a} = m_{\mathrm{s}}^{\mathrm{A}} N_{\mathrm{a,surf}} P_a(A,t) \tag{3.13}$$

can easily be established, where $N_{\mathrm{a,surf}}$ is the number of a-sites per surface area. Now consider the reaction rate s_K with the reaction

$$\mathrm{A_a} + \mathrm{B_b} \ldots \rightarrow \mathrm{D_a} + \mathrm{C_b} \ldots \tag{3.14}$$

where the dots imply that some gas phase species can also be involved in the reaction. Rewriting the left hand side of eq. 3.12 in terms of the corresponding coverage and comparing with eq. 3.11 we find

$$s_K = -\frac{N_{\mathrm{a,surf}} N_b^a}{\nu_{\mathrm{s},K}^{\mathrm{A_a}}} w_{ab}(D,C|A,B)P_{ab}(A,B,t). \tag{3.15}$$

Note, that we have used the mass balance of a reactant for finding the expression for the reaction rate, therefore the minus sign in the beginning. Since reactants have negative stoichiometric coefficients the reaction rates will always be positive.

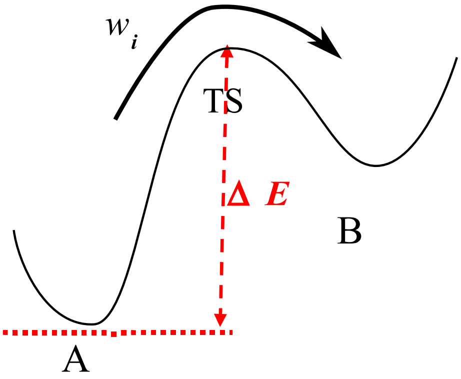

Figure 3.1: The potential energy surface is coarse-grained to its local minima. In harmonic Transition State Theory the transition from a basin A to another basin B is characterized by the transition state TS separating both minima. The corresponding RC is calculated from the potential energy difference ΔE of A and TS and their vibrational properties.

3.1.3 Sensitivity Analysis and Degree of Rate Control

A prevalent concept in chemical kinetics is the existence of rate determining steps[116, 77]. That is which elementary steps need to be more likely for the reaction to take place with a high rate and which elementary steps lower significantly this rate, when we make them more likely (e.g. by modifying the catalysts or reaction conditions). Knowing the rate-determining steps often allows to significantly simplify a given complex mechanism. Another crucial point is that we usually have an error in the rate constant. If this RC does belong to a step which is not rate determining, we expect not much impact of this error and we can hope to obtain the correct results when all other RCs are correct. Thus knowing the rate-determining steps allows to restrict our attention to these steps and to try to reduce only the error of the rate-determining steps. Campbell introduced a measure for the rate-determining steps, the so-called Degree of Rate Control (DRC)[14]. In the meanwhile the DRC has become a widely employed tool for the analysis of complex reaction networks[71]. We employ a slightly modified definition for the DRC[26, 79] for the sensitivity of the Kth stationary reaction rate on the ith independent RC w_i

$$X^i_{\mathrm{rc},K} = \frac{w_i}{s_K} \left(\frac{\partial s_K}{\partial w_i} \right)_{w_{j \neq i}} \tag{3.16}$$

where $w_i = w_{ab}(D, C|A, B)$ if the ith reaction is given by eq. 3.15. We want to call a reaction with a positive DRC rate-limiting, since increasing the number of these reactions would increase the targeted reaction rate. This reaction is in some sense a bottle-neck and limits therefore the reaction rate. We will correspondingly call a reaction with negative DRC rate-enhancing, although this wording is not intuitive.

3.2 First-Principles Rate Constants

Several different theories exist, that allow for the calculation of the RCs from the underlying microscopic dynamics[44]. Because of the high temperatures a classical description of the microscopic scale is often sufficient. It is assumed that the atoms obey Hamilton mechanics and their influence on each other is given by the PES. The most employed and practical method for coarse graining from microscopic to the mesoscopic scale is Transition State Theory in its harmonic approximation (hTST)[77]. In hTST the reaction path connecting an initial configuration A and a final configuration B is characterized by a transition state (TS) (see figure 3.1). The TS is usually a saddle point separating the two minima A and B. The modes perpendicular to the reaction path are assumed to be harmonic and hTST reduces the necessary information of the PES to the energy difference of A and TS and the vibrational modes at the TS and the initial state A. Therefore only a few evaluations of the PES are needed and a detailed simulation of the microscopic motion, e.g. molecular dynamics [37], is not necessary. This makes the problem feasible to first principles methods where a single evaluation of the potential energy E might last hours or longer on modern parallel computers[97]. In hTST the rate constants have the general form

$$w_i = \frac{k_\mathrm{B} T_\mathrm{s}}{h} \frac{Z_\mathrm{TS}}{Z_\mathrm{A}} \exp\left(-\frac{\Delta E_i}{k_\mathrm{B} T_\mathrm{s}}\right) \tag{3.17}$$

where ΔE_i is the activation barrier, the potential energy difference between initial state A and the transition state TS. T_s is the temperature at the surface. The (classical) harmonic vibrational partition function in the initial state Z_A is calculated with all modes, while only those modes perpendicular to the reaction path contribute to the partition function Z_TS in the transition state.

The surface area occupied by one unit cell will be denoted with A_unit. In each unit cell there might be different adsorption sites, each defining one site type. We want to consider adsorption, desorption and diffusion of adsorbed species. Reactions like the formation of CO_2 from adsorbed oxygen and CO will be modeled as associative desorption reactions. The RCs for the adsorption of species α can expressed by the partial pressure p_s^α and the temperature at the surface.

$$w_\mathrm{ad}^\alpha(p^\alpha) = f_\mathrm{ad}^\alpha(T_\mathrm{s}) \exp\left(-\frac{\Delta E_\mathrm{ad}^\alpha}{k_B T_\mathrm{s}}\right) \frac{p_\mathrm{s}^\alpha A_\mathrm{ad}^\alpha}{2\pi m^\alpha} \tag{3.18}$$

The local sticking coefficient $f_\mathrm{ad}^\alpha(T_\mathrm{s}) \exp\left(-\frac{\Delta E_\mathrm{ad}^\alpha}{k_B T_\mathrm{s}}\right)$ was multiplied with the impingement rate $\frac{p_\mathrm{s}^\alpha A_\mathrm{ad}^\alpha}{2\pi m^\alpha}$ from kinetic gas theory, i.e. number of gas phase molecules impinging through the active area A_ad^α. The active area A_ad^α is characteristic for the involved sites. Only gas molecules with an initial position in the active area contribute to the adsorption rate. The desorption RCs are conveniently obtained by detailed balance

$$w_\mathrm{des}^\alpha = \exp\left(-\frac{\Delta G_\mathrm{ad}^\alpha}{k_B T_\mathrm{s}}\right) w_\mathrm{ad}^\alpha \tag{3.19}$$

$$= \frac{A_\mathrm{ad}^\alpha}{A_\mathrm{unit}} f_\mathrm{des}^\alpha \frac{k_B T_\mathrm{s}}{h} \exp\left(-\frac{\Delta E_\mathrm{des}^\alpha}{k_B T_\mathrm{s}}\right) \tag{3.20}$$

The free reaction enthalpy $\Delta G^{\alpha}_{\mathrm{ad}}$ is approximated with

$$\Delta G^{\alpha}_{\mathrm{ad}} = \delta\mu^{\alpha}_{\mathrm{Ch}}(p^{\alpha}_{\mathrm{s}}, T_{\mathrm{s}}) - E^{\alpha}_{\mathrm{ad}} - k_B T_{\mathrm{s}} \ln z_{,\mathrm{ad,vib}} \tag{3.21}$$

where $\delta\mu^{\alpha}_{\mathrm{Ch}}$ is the gas phase chemical potential minus its zero Kelvin component, which can be obtained on the same basis as the specific internal energy, eq. 2.34. E^{α}_{ad} is the binding energy on the surface (site specific) and $z_{,\mathrm{ad,vib}}$ is the vibrational partition function of the adsorbed species (only those which were involved in the reaction). For diffusion events hTST gives

$$w_{\mathrm{diff}} = f_{\mathrm{diff}}(T_{\mathrm{s}}) \frac{k_B T_{\mathrm{s}}}{h} \exp\left(-\frac{\Delta E_{\mathrm{diff}}}{k_B T_{\mathrm{s}}}\right). \tag{3.22}$$

The formulas for the RCs for the mesoscopic scale contain parameters which are connected with the shape of the microscopic PES. The classical top-down approach is to fit these parameters to experimental data. Since often many different mechanism can fit a given data set equally well[70], one arrives at an effective microkinetic model, which needs not to have any microscopic meaning. Moreover, even for one and the same mechanism different parameter sets might reproduce the experimental findings with the same accuracy. An example is the here investigated CO oxidation at RuO_2 which is invariant under an exchange of site types. Exchanging in table 3.1 to 3.3 “br” against “cus” and vice versa we arrive at a microkinetic model which gives the same overall reaction rates as before.

Because of this invariance with respect to different mechanisms and parameter sets a different approach has been developed, which uses parameters obtained from the underlying electronic structure, i.e. a bottom-up approach[97]. This allows to determine the mechanism and the kinetic parameters without fitting to experimental data. The need of quantum mechanics[80, 36] is the price for this very small scale we start with. The most known and applied approach to quantum mechanics is via the Schrödinger equation (SE). Knowing the involved nuclei and the number of electrons the SE for this problem can be written down without a single parameter, that needs to be determined experimentally. As long as we do not deal with nuclear reactions or relativistic effects this SE describes all natural phenomena and experimental findings can be predicted from its solution, the wave function. Due to this universality the SE is regarded as a first principle, i.e. a natural law free of adjustable parameters. Methods which use the SE for electrons and nuclei as a basis are therefore called first principles or ab-initio methods. The problem is that we can not solve this equation except for the very simplest systems, even not numerically, since it is a partial differential equation on a $3(N_{\mathrm{elec}} + N_{\mathrm{nucl}})$-dimensional space, where N_{nucl} and N_{elec} is the number of nuclei and electrons in the system, respectively. We therefore need to introduce some approximations. The first is to separate the motion of nuclei and electrons, the Born-Oppenheimer approximation[10, 111]. The time scale of the nuclear motion is orders of magnitude larger than that for the motion of the electrons due to the much smaller mass of the latter. The nuclei are then regarded as immobile on the timescale of electronic motion and the electrons move in an external Coulomb field determined by the positions and charges of the nuclei. Doing so leads to the electronic SE, which now depends only parametrically on the nuclei. On the larger time scale of nuclear motion the electrons relax quasi instantaneously to their ground state. Assuming a quasi infinite time scale separation the potential energy for the nuclei in space is given by the electronic ground state energy plus the Coulomb interaction between the nuclei.

Even though we have now introduced a rule for obtaining the PES this rule is still not practical, since the electronic Schrödinger equation is still a very high-dimensional partial differential equation. So further approximations are needed. The quantum chemical (or wave function) methods provide a whole hierarchy of approximations, among the most popular are the very approximate Hartree-Fock, the more accurate Møller-Plesset perturbation theory, and the very accurate coupled cluster approach (for an introduction to wave function methods see e.g. [111, 65]). Unfortunately the computational complexity increases rapidly with increasing accuracy. Due to their high computational costs Coupled Cluster approaches are not feasible for surfaces and other periodic systems at all. Hartree-Fock and second order Møller-Plesset can be applied to surfaces, where the latter is a formidable task [52, 75]. Unfortunately both methods do not allow for an accurate description of metal oxide surfaces.

A different branch of electronic structure methods is Density Functional Theory (DFT). It is based on the Hohenberg-Kohn theorem [50], which state that the electronic energy E_{elec} of a system can be represented by

$$E_{\text{elec}} = \int dV n(\underline{r}) V(\underline{r}) + F_{\text{HK}}[n(\underline{r})], \tag{3.23}$$

where $V(r)$ is the external potential, i.e. the Coulomb potential of the nuclei, and $n(\underline{r})$ is the electron density. The Hohenberg-Kohn functional $F_{\text{HK}}[n(\underline{r})]$ depends solely on the electron density and not on the involved nuclei. It is therefore universally applicable to any system to which the electronic SE can be applied. The electronic ground state energy is found by minimizing E_{elec} with respect to to $n(\underline{r})$. The problem is thus reduced from 3N_{elec} to three dimensions. However, there exists no explicit formula for the Hohenberg-Kohn functional only a proof of its existence. Therefore an impressive number of approximate functionals exits, unfortunately without a hierarchy in accuracy. Almost all today employed density functional calculations make use of the Kohn-Sham equations [63], which work with single particle wave functions instead of the electron density. Thereby the number of unknown 3-dimensional fields multiplies by a factor of at least N_{elec}, but this approach allows to formulate more reliable kinetic energy functionals than on basis of the electron density alone. In [97] the functional developed by Perdew, Burke and Ernzernhof (PBE) for exchange and correlation was employed.

Due to the approximate character of the HK functionals one has to live with a certain systematic error. Usually DFT performs reasonably well for determining local minima and transition state geometries and vibrational frequencies but not so good for the energies. This error is often stated as $\sim 0.1 - 0.2$ eV, leading to an inaccuracy of a few orders of magnitude in the rate constants. We can thus a priori not expect quantitative agreement with experimental data. Therefore the empirical top-down approach is still in favor when quantitative data is required, as it is the case in engineering applications, where a quantitatively correct representation of the macroscopic response in the boundary condition eq. 2.73 is more important than microscopic understanding.

Being the most accurate of the feasible methods for obtaining the barriers DFT is still computationally very demanding, so that its application to complex reaction mechanism becomes soon intractable. The high computational complexity forces us to make a selection of those rate constants, which should be treated by DFT and which can be treated with less accurate but therefore very efficient methods. Starting with a set of approximate RCs and employing the DRC we can identify those RCs, where changes matter most for the reaction rates and which we need to refined. The remaining inaccuracy of DFT for the rate constants also makes it interesting to apply more accurate methods. For metallic surfaces like the here investigated $RuO_2(110)$, there are not very many methods, that improve accuracy over standard DFT. One such method is the Random-Phase Approximation, which has recently attracted some interest and which was able to resolve some drawbacks of of the known DFT functionals[46, 91]. The selection which numbers to improve on can be based on the DRC criterion again. Making use of the DFT geometries for minima and transitions state the number of energy evaluations with more accurate higher order methods can be further decreased and an application of those methods to the here described problems seems to be feasible in the nearer future.

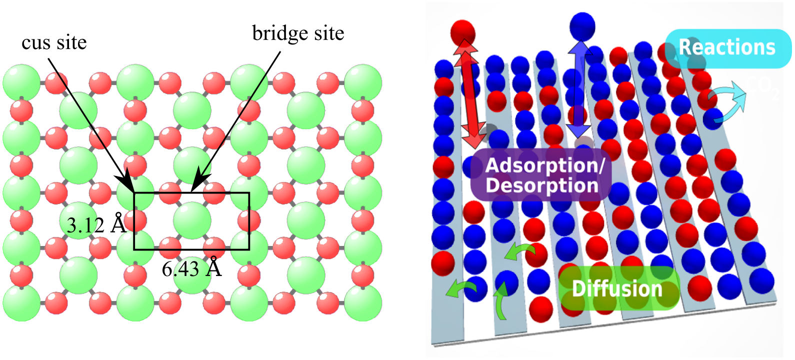

Figure 3.2: Left: Top view of of the RuO$_2$ surface (red: oxygen, green: ruthenium). The surface exhibits two dominant adsorption sites where CO and O can bind: bridge between two ruthenium atoms and cus on top of a ruthenium atom. The surface unit cell is (3.12 Å x 6.43 Å) $\approxeq$ 20 Å^2. Right: The employed lattice model with the br and cus sites aligned in rows. Each site can have three adsorbate states: CO covered (blue ball), oxygen covered (red), and empty (no ball). The possible processes are adsorption and desorption of CO and oxygen, surface diffusion and the formation of CO$_2$ from adsorbed CO and oxygen.

Table 3.1: Parameters for the RCs for CO and O$_2$ ad/desorption (from [97]).

	$\Delta E^\alpha_{\mathrm{ad}}$	$\Delta E^\alpha_{\mathrm{des}}$	$A^\alpha_{\mathrm{ad}}/A_{\mathrm{unit}}$	f^α_{ad}
$\mathrm{CO} \leftrightarrow \mathrm{CO_{cus}}$	0	1.60	0.5	1.0
$\mathrm{CO} \leftrightarrow \mathrm{CO_{br}}$	0	1.30	0.5	1.0
$\mathrm{O_2} \leftrightarrow \mathrm{O_{cus}} + \mathrm{O_{cus}}$	0	2.00	0.5	1.0
$\mathrm{O_2} \leftrightarrow \mathrm{O_{br}} + \mathrm{O_{br}}$	0	4.60	0.5	1.0
$\mathrm{O_2} \leftrightarrow \mathrm{O_{br}} + \mathrm{O_{cus}}$	0	3.30	0.5	1.0

3.3 CO Oxidation at RuO$_2$(110)

The CO oxidation at RuO$_2$(110) has been studied extensively over the last years, both experimentally and theoretically. The accepted picture is that the chemical kinetics predominantly takes place at two different types of adsorption sites, the so-called bridge (br) and coordinatively unsaturated (cus) sites, resp.[85, 97].

We use the DFT based microkinetic model developed by Reuter[97], which has shown to be in good agreement with UHV experiments[95, 99]. The smallest surface unit cell has a size of $A_{\mathrm{unit}} \approxeq 20$Å^2. The clean surface, i.e. without adsorbates in shown in the left panel of figure 3.2. Oxygen is depicted as red spheres, and ruthenium as green spheres. The surface structure implies to use a lattice model, where br and cus sites are aligned in alternating rows (see right panel in figure 3.2). In an atmosphere composed only of CO, O$_2$, and CO$_2$ the only two surface species are atomic oxygen (red balls) and carbon monoxide

Table 3.2: Parameters for the RCs for the diffusion of CO and O (from [97]).

	ΔE_{forw}	ΔE_{back}	f^{α}_{diff}
$CO_{\text{cus}} \leftrightarrow CO_{\text{cus}}$	1.70	1.70	1.0
$CO_{\text{br}} \leftrightarrow CO_{\text{br}}$	0.60	0.60	1.0
$CO_{\text{cus}} \leftrightarrow CO_{\text{br}}$	1.30	1.60	1.0
$O_{\text{cus}} \leftrightarrow O_{\text{cus}}$	1.60	1.60	1.0
$O_{\text{br}} \leftrightarrow O_{\text{br}}$	0.70	0.70	1.0
$O_{\text{cus}} \leftrightarrow O_{\text{br}}$	1.00	2.30	1.0

Table 3.3: Parameters for the RCs for formation of CO_2 from adsorbed CO and O_2 (from [97]).

	ΔE_{CO_2}	$A^{\alpha}_{CO_2}/A_{\text{unit}}$	f^{α}_{ad}
$CO_{\text{cus}} + O_{\text{cus}} \leftrightarrow CO_2$	0.9	0.5	0.5
$CO_{\text{br}} + O_{\text{br}} \leftrightarrow CO_2$	1.5	0.5	0.5
$CO_{\text{cus}} + O_{\text{br}} \leftrightarrow CO_2$	1.20	0.5	0.5
$O_{\text{cus}} + CO_{\text{br}} \leftrightarrow CO_2$	0.80	0.5	0.5

(blue balls), which both occupy only one site each. CO_2 does not bind to the surface and leaves it as soon as it is formed. The elementary processes included in the kinetic model are adsorption and desorption of reactants (CO and O_2), where oxygen adsorbs dissociatively and CO molecularly, diffusion of adsorbed species to a neighboring vacant site, and formation of CO_2 from adsorbed oxygen and CO, referred to as reaction steps in the following. These are in total 26 different elementary steps. The model includes no lateral interactions, which is reflected by all ΔE being independent of the arrangement of the adsorbates on the surface. The adsorption and desorption of CO and O_2 is modeled with the equations 3.18 and 3.19. The temperature dependent part of the chemical potential $\Delta\mu^{\alpha}_{\text{Ch}}$ is taken from thermochemical tables [110], all other necessary parameters can be found in table 3.1. Diffusion is modeled according to equation 3.22, the possible diffusion processes and the necessary parameters are given in table 3.2. The reaction events are modeled according to equation 3.20. The necessary kinetic parameters are shown in table 3.3. The re-adsorption of CO_2 is very unlikely due to sizable barriers for these processes. These can be easily calculated from the adsorption energetics of the reactants, the gas phase zero Kelvin energy of CO_2 in table 2.1 and the barrier for CO_2 formation. Regardless of the partial pressure of CO_2 the adsorption of this species is so unlikely, that these processes have no impact on the reactivity at all.

We will concentrate on steady-state operation, so the TOF is the only relevant macroscopic reaction rate for the determination of the jump conditions for the diffusive mass fluxes, eq. 2.78. The TOF is the sum of the reaction rates of the four different possible CO_2 reaction steps. Writing it in terms of probabilities eq. 3.15 we find

$$
\begin{aligned}
TOF/N_{\text{site}} = {} & w_{\text{br,br}}(*,*|\text{O,CO})P_{\text{br,br}}(\text{O,CO}) \\
& + w_{\text{cus,cus}}(*,*|\text{O,CO})P_{\text{cus,cus}}(\text{CO,O}) \\
& + w_{\text{br,cus}}(*,*|\text{O,CO})P_{\text{br,cus}}(\text{O,CO}) \\
& + w_{\text{br,cus}}(*,*|\text{CO,O})P_{\text{br,cus}}(\text{CO,O})),
\end{aligned}
\tag{3.24}
$$

where N_{site} is the number of sites (br and cus) per unit area and the asterisk stands for a vacant site.

3.4 Solving the Master Equation

The ME can hardly be solved explicitly because of the exploding number N_{state} of possible states $\mathbf{x}$ with increasing number of sites N_{sites}. As an example we consider a (10x10) lattice where each site can have two different adsorbate states, so that $N_{\text{state}} = 2^{N_{\text{sites}}} = 2^{100} \approx 10^{30}$. The coupled differential equation system eq. 3.3 for the N_{state} unknown probabilities becomes numerically unsolvable simply by its size - even for this moderately sized problem. Yet, even if we could solve the ME for what do we need all this information for? In the macroscopic catalysis context we are only interested in reaction rates. Microscopically coverages, two or three site probabilities are interesting quantities, or if islands form and which shape they have. So we need much less information than what is contained in $P(\mathbf{x}, t)$. Methods are therefore welcome, which only deliver a reduced amount of information, but therefore are computationally less demanding (i.e. feasible). We present two methods, which are both used in catalysis research and represent the two extreme ends of solution techniques. The first - kinetic Monte Carlo (kMC) - is a numerically exact method to obtain expectation values like reaction rates. That is the error is controllable and can in principle be reduced to zero, if enough computing resources are provided. The second is the so called phenomenological kinetics (PK). It only considers the coverages and uses eq. 3.11 to derive rate equations. It is conceptually and computationally much less demanding than kMC, which makes it the method of choice in most of all kinetic studies in present day practical research[17]. This advantage comes for the cost that a more or less physical assumption has to be made in order to express the pair probabilities in terms of the coverages. A systematic error is introduced, which can not be reduced regardless of the resources invested.

3.4.1 Kinetic Monte Carlo Simulation

As already mentioned kMC is a numerical method to obtain expectation value, which differ only by a controllable numerical error from those obtained by a direct solution of the ME[11, 40, 55, 120]. The idea behind kMC is based on the fact that the ME describes the dynamics of jump processes. The desired expectation values are obtained by generating a series of trajectories of such jump processes, the statistics of which formally obey the ME, and finally by performing statistical averaging over these trajectories to obtain expectation values. With an increasing number of trajectories the approximated statistical average will tend to the probabilistic average obtained from the solution of the ME for $P(\mathbf{x}, t)$.

Due to the stochastic nature of the process there exist an uncountable number of possible trajectories starting from the same initial configuration $\mathbf{x}$. Accordingly many different rules for generating a trajectory exist and a number of different kMC algorithms have been developed over the years. There are two families of kMC algorithms, namely rejection-free and null event algorithms. Generally a kMC algorithm consists of a sequentially generated number of time steps, at which the lattice configuration $\mathbf{x}$ is updated. Null event algorithms allow for time steps at which no event is executed. That is why they are often considered to be not so efficient, and also the connection of a time step to real time is not trivial. Rejection-free algorithms on the other hand adjust the time step so that one event is executed per time step and they allow for a proper connection to real time. A good review on different flavors of null-event and rejection-free kMC algorithms is given by Chatterjee and Vlachos[16]. Here we will employ a rejection-free kMC algorithm, the so-called direct kMC. The idea is first to determine the (random) waiting time for which a given state $\mathbf{x}$ stays unchanged. Then a process is selected with a probability on the basis of its RC and the state is updated according to the selected process. It can be shown that the waiting time obeys an exponential distribution[35, 51]. Thus the waiting time can be obtained by

$$t_{\text{wait}} = -\frac{1}{W} \ln(\xi_1), \tag{3.25}$$

with uniformly distributed random numbers ξ_1 in $[0, 1]$. The total rate W is given by sum over all rate constants of possible processes. The probability of a certain process i to appear is w_i/W, where w_i is the RC of that process. Having N_p processes a certain process can be selected by dividing $[0, 1]$ into N_p intervals, each assigned to a process i and with the width w_i/W. Then a second uniformly distributed random number $\xi_2 \in [0, 1]$ is drawn. The process is executed in which interval ξ_2 lies.

Thus we can write the kMC algorithm as

1. initialize lattice $\mathbf{x}$, process list $\{w_i\}$ and time $t = 0$
2. select two random numbers ξ_1, ξ_2
3. calculate total rate $W = \sum_i^{N_p} w_i$
4. select process l by
$$\sum_{i=1}^{l-1} w_i \leq \xi_1 W < \sum_{i=l+1}^{N_p} w_i \tag{3.26}$$
5. execute process, update $\mathbf{x}$ and $\{w_i\}$
6. update time $t \rightarrow t - ln(\xi_2)/W$
7. $t < t_{\text{end}}$ go to 2
8. end

Homogeneous systems are mimicked by employing periodic boundary condition, i.e. lattice sites located at opposite boundaries of the lattice are treated as neighbors. The size of the replicated periodic images is constrained by the requirement, that a site should not 'feel' its periodic image. In other words the two sites i and j would be uncorrelated, i.e. $\Pi_{ij}(x_i, x_j) = \Pi_i(x_i)\Pi_j(x_j)$, if they were more than the lattice size away from each other. In the direct method the process list is updated by going through the whole lattice and counting all possible processes in each step. More elaborate update algorithms exist achieving a better scaling with the number of sites[16], but for our case we can stick to simple updating, since we only need to consider a moderate number of sites. We employ a 20x20 lattice, which is sufficient for this system [112], exhibiting no far range correlation. Stationary data is obtained by time averaging, running the simulations until the steady-state is reached. In practice we run the simulation for at least 10^8 steps starting with the final lattice from a previous simulation with similar reaction conditions. Accurate steady-state data is obtained by averaging over the last 3×10^7 steps, which ensures that the numerical error is negligible for a non-vanishing TOF. The TOF is obtained by counting the number of reaction events, not by equation 3.24.

3.4.2 Classical Phenomenological Kinetics

Phenomenological kinetics (PK) is the most widely employed tool to study chemical kinetics in catalysis[27, 17]. To arrive at the PK description equation 3.11 needs to be closed, i.e. we need to express the pair probabilities in terms of the coverages. We will term a theory relating the pair probabilities and the coverages a correlation model. Nearly exclusively all work has been performed employing a mean-field approximation (MFA)[23, 17]. We assume that the adsorbed species are equally distributed on the surface. In this situation species A on a site a will always be observed with the same probability independently of what is adsorbed at a neighboring site b. Therefore the conditional probability $P_{ab}(A|B,t) = P_{ab}(A,B,t)/P_b(B,t)$ does not depend on B and we find

$$P_{ab}(A,B,t) = P_a(A,t)P_b(B,t). \tag{3.27}$$

We insert this expression into equation 3.11 and compare this to the standard formulation of PK

$$\frac{dP_a(A,t)}{dt} = \ldots \sum_{\alpha}^{N_{\mathrm{reac}}} \nu_\alpha^{A_a} k_\alpha^{PK} (P_b(B,t)P_c(C,t))_\alpha \tag{3.28}$$

for the generic reactions $B_b(\alpha) + C_c(\alpha) \to D_b(\alpha) + E_c(\alpha)$, where N_{reac} is the number of different reactions and $\nu_\alpha^{A_a}$ is the stoichiometric coefficient of A_a in reaction α. The dots imply that we have left out the single site processes, since they have already the desired form. The index at the brackets imply that b, B, c, and C depend on the reaction α. We find that the RC k_α^{PK} for the reaction $A_a + B_b \to C_a + D_b$ used in the standard formulation of PK is usually by a factor N_b^a larger than the RC in the ME. The only exception is when site b has the same adsorbate state as site a before and after the reaction and both are of the same type. For these cases the PK RC is only $N_b^a/2$ larger.

Notwithstanding its importance a derivation of the rate equation of PK from the more accurate stochastic model eq. 3.3 lacks in almost all textbooks on surface kinetics and catalysis[2]. This becomes even more astonishingly considering that all textbooks treat the theory of RCs on a quite detailed level. Nota bene for a set of parameters which will be fitted to experimental data in almost all cases. In the meanwhile this common neglect of the statistical basis of PK has led to some strange developments. For instance it is common to incorporate lateral interactions into classical PK by coverage dependent reaction barriers. This would lead to a coverage dependence of the rate constants [23]. However, this is unphysical since a barrier is a microscopic quantity while coverages can be regarded as macroscopic statistical averages. No microscopic quantity can depend on the latter. Also from the structure of the general master equation 3.3 it is clear that the right hand site of the rate equations can only depend polynomially on the coverages, actually with a low order of the polynomial since lateral interactions are in general short ranged. Coverage dependent barriers would contrariwise lead to an exponential dependence.

In this work simulation results for the phenomenological theories has been obtained by numerical integration of the occurring differential equations with the LSODE solver[48]. The employed discretization scheme is the stiff backward differentiation formula method and the tolerance is 10^{-12} for the relative and absolute error of all six coverages.

---

[2] Actually we found none, where such a derivation was performed. Therefore the detailed introduction into the stochastic description of surface reactions.

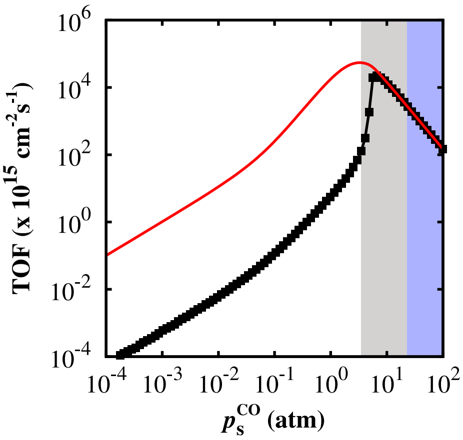

Figure 3.3: Turnover frequency (TOF) for T_s=600K, $p_s^{O_2}$ =1atm, and varying p_s^{CO} obtained with different methods: kMC (black squares), MFA (red line). Depending on p^{CO} the surface is in different coverage states: fully oxygen covered at low p_s^{CO} (white background), fully CO covered at high p_s^{CO} (blue background), and an intermediate regime with both species on the surface in appreciable amounts (gray background). The MFA gives good agreement for high CO coverage, but deviates strongly for high oxygen coverage.

3.5 Accurate and inefficient vs. efficient and inaccurate

For the steady-state CO oxidation at RuO_2(110) we want to compare the results obtained by kMC, very accurate but also very expensive, with the findings of the PK, very efficient but also equipped with a crude approximation. Employing the same microkinetic model any deviation of the PK results from those obtained with kMC must solely originate from the MFA. Such a comparison for the CO oxidation at RuO_2(110) had just been performed by Temel and co-workers[112], when the present PhD thesis was started. They used the traditional textbook approach starting from the rate equations 3.28 and identifying the PK-RC with the 1p-RC. Further diffusion was not considered, as it is common in classical PK. For the bridge to bridge or cus to cus diffusion this does not matter since the reaction rates cancel out already in equation 3.11 before any approximation, but the diffusion between different site types is not zero a priori. Here we keep it and also use the proper prefactors.

The steady-state turnover frequency (TOF) obtained with different methods is shown in fig 3.3. The operating conditions are 1 atm oxygen partial pressure $p_s^{O_2}$, a temperature T_s of 600K and varying CO partial pressure p_s^{CO}. This kind of 'experiment' was conducted in the studies of the employed 1p-microkinetic model[97, 79, 112] and we stay with it, so that we can make use of the findings stated there. The range of CO partial pressures $p_s^{CO} \in [10^{-4}, 10^{2}]$ and the oxygen partial pressures were chosen so, that the surface undergoes all relevant surface states at ambient pressures from fully oxygen covered at lowest p_s^{CO} to fully CO covered at the highest p_s^{CO}.

We first discuss the kMC results which are the black squares in fig 3.3. At very low p_s^{CO} the surface is fully oxygen covered and the reactivity is very low (white background). Increasing p_s^{CO} the TOF increases and the surface becomes populated by both, CO and oxygen (gray background). We will call this range

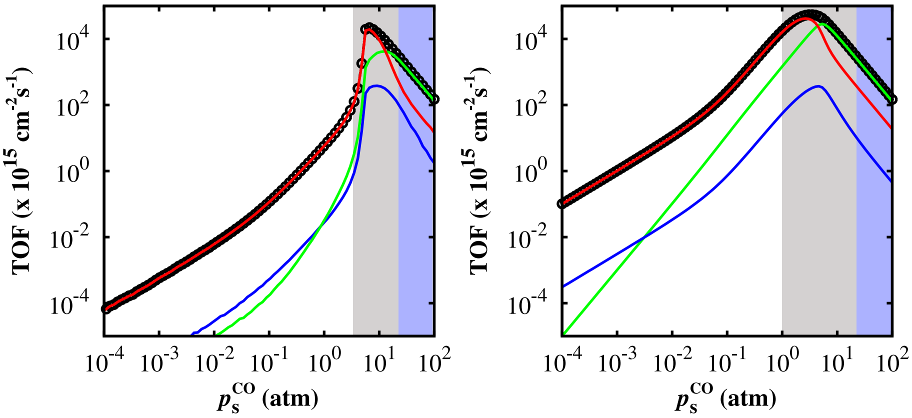

Figure 3.4: The different contributions to the total TOF for T_s=600K, $p_\mathrm{s}^{O_2}$ =1atm, and varying $p_\mathrm{s}^{\mathrm{CO}}$ obtained with kMC (left panel) and MFA (right). Shown are the reactions $\mathrm{CO_{cus}} + \mathrm{O_{cus}}$ (red), $\mathrm{CO_{cus}} + \mathrm{O_{br}}$ (blue) and $\mathrm{O_{cus}} + \mathrm{CO_{br}}$ (green). At very high and very low CO partial pressures MFA and kMC predict the same dominant reaction mechanism, albeit MFA overestimates the TOF for the former regime by 3 orders of magnitude. In the intermediate regime MFA fails to give the correct answer to this question. Anyhow the MFA still agrees quantitatively with kMC for $p_\mathrm{s}^{\mathrm{CO}}$= 10 atm.

of gas phase condition the intermediate regime. After the reactivity reaches a maximum at about $p_\mathrm{s}^{\mathrm{CO}}$= 7 atm the surface gets more and more CO poisoned, leading to a completely CO covered surface for high p^{CO} (blue background). Under all reaction conditions the surface is fully covered with adsorbates and the concentration of vacancies is low. If we now have a look at the MFA data (red line) we see that we have a nearly perfect agreement for the last regime. Yet, the more oxygen is on the surface the more the MFA deviates from the reference kMC simulations, even showing high activity where the kMC determines the catalyst to be nearly inactive. For the lowest pressures of CO the mismatch is three orders of magnitude. The differences for the coverages are mainly a less rapid change with partial pressure and therefore a wider transition regime.

Despite this tremendous quantitative difference most qualitative features of the correct kMC results also appear in the MFA curve. This is a reaction order (see appendix B) of one for the lowest CO partial pressures followed by an increase of the reaction order at $10^{-2} < p_\mathrm{s}^{\mathrm{CO}} < 10^{-1}$. The maximum reactivity is reached for $p_\mathrm{s}^{\mathrm{CO}} \approx$ 3atm. For higher CO partial pressures the reaction order is minus two. Different from experiment we can resolve the TOF data in more detail and compare the contributions to the total TOF from the different reaction channels (see figure 3.4). Both theories give the same dominant reaction paths for very high and very low $p_\mathrm{s}^{\mathrm{CO}}$. At low $p_\mathrm{s}^{\mathrm{CO}}$ the dominant path is the $\mathrm{CO_{cus}} + \mathrm{O_{cus}}$ reaction (red line), at high $p_\mathrm{s}^{\mathrm{CO}}$ it is the $\mathrm{CO_{br}} + \mathrm{O_{cus}}$ reaction (green line). Also the relative contribution to the total TOF of the second

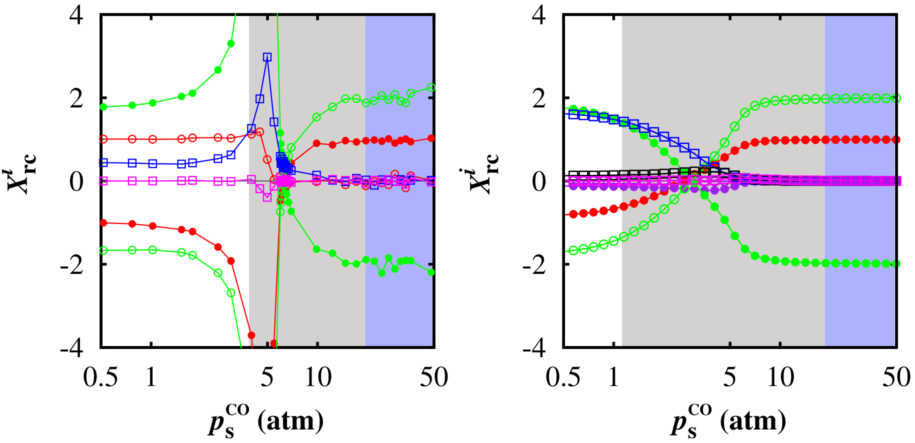

Figure 3.5: DRC for T_s=600K, $p_s^{O_2}$ =1atm, and varying p_s^{CO} obtained with kMC (left panel) and MFA (right). The TOF is only sensitive to the adsorption and desorption of CO on cus sites (green filled and empty circles, resp.), the adsorption and desorption of oxygen on cus sites (red filled and empty circles, resp.), and the $CO_{cus} + O_{cus}$ reaction (blue squares). For high p_s^{CO} MFA reproduces the kMC sensitivity nearly perfectly. This agreement extends to lower p_s^{CO} until the kMC TOF changes its slope.

largest reaction rate is well described by the MFA for very low and very high CO partial pressures. In the intermediate range the differences between both approaches are more prominent. At the partial pressures where each theory has its maximum we find that this highest reactivity is differently composed: the MFA predicts same contributions to the TOF by the $CO_{cus} + O_{cus}$ and $CO_{br} + O_{cus}$ reactions, while with kMC the whole reactivity is due to the former reaction channel. At a slightly higher p_s^{CO} = 10atm both approaches give the same total TOF value. But kMC still predicts the $CO_{cus} + O_{cus}$ reaction to be dominant, which is only of minor importance in the MFA. So the MFA can not be valid anymore, although it agrees quantitatively with the exact kMC results.

To shine further light into into the reasons behind these discrepancies we investigate the DRC obtained with kMC[79] (see left panel in figure 3.5). In the whole range of studied gas phase conditions there are only a few elementary steps, which are rate determining. These are the adsorption and desorption of oxygen and CO on cus sites and the reaction involving only cus sites. At the highest p_s^{CO} the adsorption of O_2 is found to be rate limiting as well as the desorption of CO. Increasing the CO adsorption decreases the TOF (which we call a rate enhancing step, see section 3.1.3). In the other limit of low p_s^{CO} we find that now the adsorption of CO and the desorption of oxygen are rate limiting and the corresponding backward reactions are rate enhancing. Further the dominant reaction (the $CO_{cus} + O_{cus}$ reaction) is rate limiting. Both findings can be explained in a unified manner. In both limits we have a majority species (MaS), which covers uniformly the whole surface. In order to enable the reactions we have to bring the minority species (MiS) onto the surface. For that we need vacant sites produced by the desorption of the MaS and therefore this process is rate limiting. Since the vacant sites need to be filled with an MiS the corresponding adsorption is also rate limiting. This adsorption of a MiS of course only occurs, when the vacant site is not filled again by an adsorption of the MaS. Thus the MaS adsorption is rate enhancing. The adsorbed MiS can now desorb again or react. If the occurring reaction is very fast, i.e. it has a low barrier, and the desorption of the MiS is slow (compared to the reaction) the reaction will take place as soon as a MiS is adsorbed. In this case the MiS desorption is not rate determining, since only a very few of the adsorbed MiS desorb and doubling this number will lead only to a minor decrease of those MiS, which leave the surface by reaction. This is the case for the highest $p_{\mathrm{s}}^{\mathrm{CO}}$, where the dominant $\mathrm{CO}_{\mathrm{br}} + \mathrm{O}_{\mathrm{cus}}$ reaction has a barrier of 0.8 eV which is much smaller than the barrier for oxygen desorption (lowest: 2.0 eV). For the other extreme $p_{\mathrm{s}}^{\mathrm{CO}} = 0.5$ atm the br sites are blocked by oxygen due to the high barriers for oxygen desorption involving a br site. Thus the $\mathrm{CO}_{\mathrm{cus}} + \mathrm{O}_{\mathrm{cus}}$ reaction is the dominant reaction channel. The barrier of this process (0.9 eV) is higher than for the $\mathrm{CO}_{\mathrm{br}} + \mathrm{O}_{\mathrm{cus}}$ reaction and the reaction steps is rate limiting. Further the barrier for CO desorption from a cus site is now in a comparable size (1.3 eV). The DRC shows this elementary step to be rate enhancing: blocking this step will increase the TOF.

Comparing the MFA data (right graph in fig. 3.5) with the kMC results we have a quantitative agreement for high CO partial pressures. Similar to kMC all none zero DRCs change their sign when crossing the intermediate region. But differently the MFA DRCs show no peak structure in the intermediate regime. At the lowest $p_{\mathrm{s}}^{\mathrm{CO}} = 0.5$ atm the MFA agrees quite well with the reference kMC results with one exception: the TOF is completely insensitive to the oxygen desorption. This is in contradiction to the before considered properties of a surface fully covered with one species. On such a surface the desorption of the MaS must be rate determining. With the larger extent to lower $p_{\mathrm{s}}^{\mathrm{CO}}$ of the intermediate regime for MFA we expect the limit of a oxygen covered surface to be shifted to comparatively lower $p_{\mathrm{s}}^{\mathrm{CO}}$. So we have to consider even lower CO partial pressures to reach this regime. Now we observe similar results as with kMC for $p_{\mathrm{s}}^{\mathrm{CO}} = 0.5$ atm especially the oxygen desorption is rate enhancing (not displayed).

The question arises what is the origin of the good agreement between MFA and kMC for the total TOF at $p_{\mathrm{s}}^{\mathrm{CO}} = 10$ atm, although both give different values for the partial TOFs. At the highest $p_{\mathrm{s}}^{\mathrm{CO}}$ the MFA is valid and both agree quantitatively for the total TOF as well as for the different contributions. Also the DRCs obtained with MFA and kMC, resp., agree quantitatively at these pressures. At the lower $p_{\mathrm{s}}^{\mathrm{CO}} = 10$ atm both kMC and MFA still show the same DRC, which explains the good agreement. Since we can always write the pressure dependence of the TOF as

$$TOF(p_{\mathrm{s}}^{\mathrm{CO}}=10) = TOF(p_{\mathrm{s}}^{\mathrm{CO}}=100) + \int\limits_{p_{\mathrm{s}}^{\mathrm{CO}}=100}^{p_{\mathrm{s}}^{\mathrm{CO}}=10} \left(\frac{\partial TOF}{\partial p_{\mathrm{s}}^{\mathrm{CO}}}\right)_{\partial p_{\mathrm{s}}^{\mathrm{CO}}=p^*} dp^* \quad (3.29)$$

both MFA and kMC agree if they provide the same derivative with respect to $p_{\mathrm{s}}^{\mathrm{CO}}$ for $p_{\mathrm{s}}^{\mathrm{CO}} \in [10, 100]$atm. In other words they agree because they show the same sensitivity for the CO adsorption, since the TOF depends only on the partial pressures by the corresponding adsorption rate constants. This finding can be brought into a stronger statement: Suppose the correlation model (e.g. the MFA) of a phenomenological theory is fulfilled at certain reactions conditions and it is violated in a neighborhood of these reaction conditions. This model still gives the correct answer in the whole neighborhood as long the rate determining steps and their importance (aka DRC) are reproduced correctly. The requirement of reproducing the rate determining steps is much weaker than the requirement of a proper correlation model. This might serve as an explanation why phenomenological models work so well although the assumptions they are based on are not appropriate. This insensitivity of the macroscopic reaction rates also shows that findings from phenomenological models should not be over-interpreted: Suppose we have a correlation model which reproduces the reaction rate quantitatively for a range of reaction conditions. Further we validate this model by experiments, which allow for a direct microscopic access. Now usually this detailed microscopic data is much more difficult to obtain than macroscopic reaction rates and we therefore restrict to one set of reaction conditions. Of course one would like to use the model now to gain insight on the microscopic behavior at different reaction conditions. But by doing so we overstress the correlation between microscopic and macroscopic behavior; just because the model represents the microscopic behavior at some certain reaction conditions and reproduces the macroscopic rates also at different conditions, it is not said that it also represents the microscopic behavior at these different conditions!

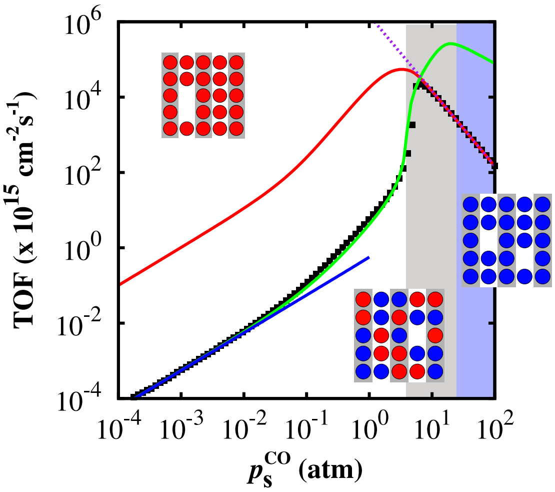

Figure 3.6: Turnover frequency (TOF) for T_s=600K, $p_\mathrm{s}^{\mathrm{O}_2}$ =1atm, and varying $p_\mathrm{s}^{\mathrm{CO}}$ obtained with different methods: kMC (black squares), MFA (red line), MPK (green line), and analytical results for the limits (purple: based on MFA; blue: based on MPK). The insets show typical surface states, where oxygen is displayed red, CO blue. The rows of bridge sites are marked gray and cus rows white. The modified PK behaves opposite to the MFA. It agrees well for high oxygen coverage, but for high CO coverage its assumptions are not valid anymore and it fails.

3.5.1 Modified Phenomenological Kinetics

Why does the MFA work well in the CO covered regime and fails so tremendously for the oxygen covered surface? In both cases we have no lateral interactions and the surface is uniformly covered with one single species. In order to arrive at a better description of the oxygen covered regime we have to identify those terms in equation 3.11 which are not well approximated by a MFA and have an impact on the simulation results. Since each term in 3.11 can be associated to a certain reaction, it seems reasonable to start with the rate-determining steps. This does not mean that other terms are well described, but an error in these will have less impact on the overall reactivity. From the previous comparison we know that in the considered regime only five reactions are rate-determining. These are the adsorption and desorption of CO on cus sites, adsorption and desorption of oxygen on two cus sites and the reaction to CO_2 where both reactants are adsorbed on cus sites. Since ad/desorption of CO is a single site process the terms associated with these reactions are exactly described because no MFA is necessary (see eqn. 3.11). For the desorption of oxygen we need $P_{\mathrm{cus,cus}}(\mathrm{O,O})$. Since the surface is fully oxygen covered $P_{\mathrm{cus,cus}}(\mathrm{O,O}) \approxeq 1$ which also holds for the coverages and therefore for their product. Hence the MFA for this term can not be responsible for the large deviation. Thus the major source of error must lie in the MFA for $P_{\text{cus,cus}}(*, *)$ (oxygen adsorption into vacancies) and $P_{\text{cus,cus}}(\text{CO,O})$ (formation of CO_2). At an oxygen covered surface vacancies are mostly created by the desorption of oxygen. For $RuO_2(110)$ we have three different types of oxygen desorption and the desorption from two cus sites occurs most often in the kMC, since it has the lowest barrier. The desorption is associative and empty cus sites are formed in pairs. Under the investigated conditions the RCs for diffusion of oxygen are much lower than the adsorption RC for oxygen. As a consequence the formed vacancies can be regarded as immobile and the vacancy pair is stable until the an oxygen molecule is adsorbed again. This is confirmed by kMC simulations, where we only observed vacancies occurring in pairs (as displayed by the inset for the oxygen covered regime). This concerted appearance of vacancies next to each other is definitely not well described by a MFA. If we find a vacancy on a cus site one of the neighboring cus sites will also be empty in almost all cases, not with a probability proportional to the coverage of vacancies as the MFA implies. Now also a CO molecule can adsorb on one of the vacancies. Since oxygen needs two adjacent sites for the adsorption the other site will stay empty or adsorb a further CO molecule. Thus when one finds a CO adsorbed on a cus site only one of the neighboring cus sites will carry an oxygen. The other cus site will be empty or covered with CO. The above considerations imply for the pair probabilities

$$\begin{aligned} P_{\text{cus,cus}}(*, *, t) &= \frac{P_{\text{cus}}(*, t)}{2}, \\ P_{\text{cus,cus}}(\text{CO,O}, t) &= \frac{P_{\text{cus}}(\text{CO}, t)}{2}. \end{aligned} \tag{3.30}$$

Replacing the corresponding MFA expressions by the above we arrive at the green line in figure 3.6. We see that the modified phenomenological kinetic (MPK) model matches the true solution for high oxygen coverage and deviates from it for higher CO pressures. The above analysis now also allows an explanation why the MFA overestimates the TOF in this regime. The limiting factor for the formation of CO_2 at a high oxygen coverage is to get CO on the surface. If we place vacancies randomly on the surface, it is rather unlikely that an oxygen molecule finds a pair of neighboring vacancies. Thus much more vacancies are available for CO adsorption and the TOF will be higher.

For the CO covered regime we can now also explain why the MFA works so well there. In this regime there are only three rate determining steps. These are the ad/desorption of CO on cus sites and the adsorption of oxygen on cus sites. This means that occurrence of vacancy pairs is the important point in the phenomenological modeling similar as before. However, now the situation is different: on a fully CO covered surface the main process of vacancy creation is the CO desorption. Since this frees always only a single site, vacancies will be formed at a random position and the MFA is a valid assumption.

The results obtained by the MPK agree too well with the kMC data. Not for very low CO partial pressures. Here we have a fully oxygen covered surface and we expect the MPK to work well, since it was derived especially for this

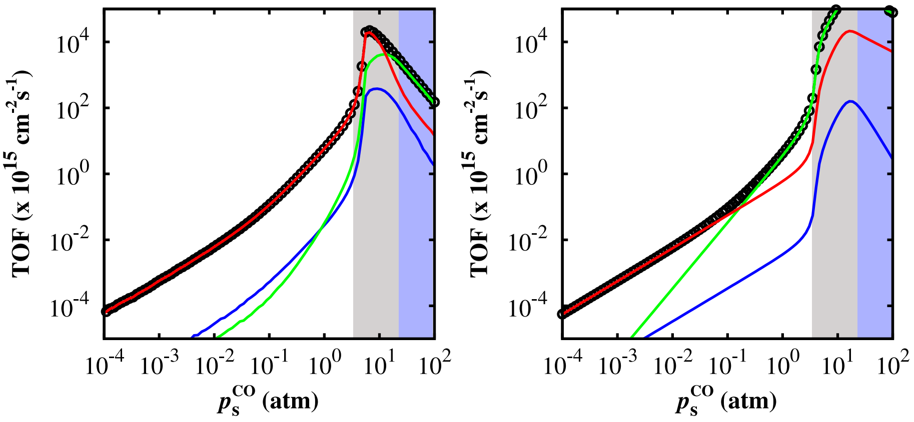

Figure 3.7: Same as 3.4 but MPK results are displayed in the right panel instead of MFA. For the extreme conditions it was derived MPK predicts correctly the dominant reaction mechanism. But already at 0.1 atm it favors the $CO_{br} + O_{cus}$ reaction, while the $CO_{cus} + O_{cus}$ is still by far the most occurring reaction at these conditions.

regime. However, near the maximum the assumptions, which led to eq. 3.30, are not fulfilled and the MPK still matches the kMC results. This agreement is not because the MPK correlation model correctly reflects the microscopy for the intermediate reaction conditions. In some sense this is not so surprising, the correlation model is constructed so that it agrees with the MFA for $P_{cus}(O) = 0.5$. With MPK having a much lower activity than MFA for high oxygen coverage a more or less steep increase was expected since both must match at some point. Looking at the contributions from different reaction channels we observe that both kMC and MPK give very different answers to this problem, see fig. 3.7. At very low pressures MPK identifies the $CO_{cus} + O_{cus}$ reaction to contribute the far most in agreement with kMC. Also the importance of the other reaction channels is reproduced more or less correctly. Increasing the CO partial pressure to $p_s^{CO} > 10^{-1}$atm we still have a quantitative agreement, but while kMC still assigns nearly all reactivity to the $CO_{cus} + O_{cus}$ reaction, MPK yields the $CO_{br} + O_{cus}$ reaction as dominant. Similar as for the MFA at $p_s^{CO} = 10$atm we have the situation that the total TOF is reproduced correctly although the different reaction channels are not properly described.

The reasons for the good agreement can be clarified by considering the DRC again. In the left panel of figure 3.8 the DRCs for oxygen ad- and desorption are shown. For ad/desorption on two adjacent cus sites we find a nearly quantitative agreement between kMC (dark green) and MPK (red). The adsorption of oxygen on a bridge and an adjacent cus site occurs only in the MPK, but also only near the point of highest activity of the kMC data where we have a transition from the regime where MPK works well to the regime where the MFA works well. So we can say that the MPK reproduces the sensitivity for oxygen adsorption

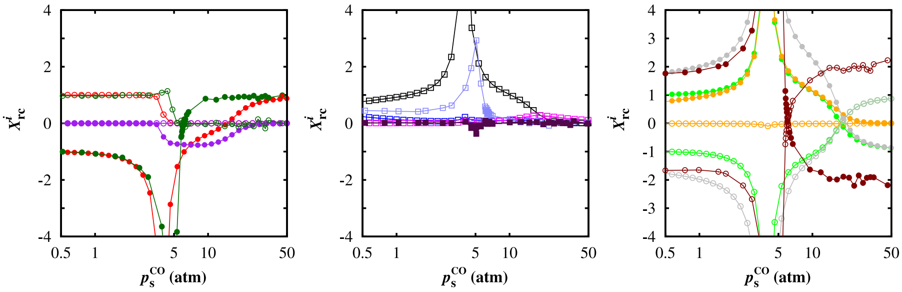

Figure 3.8: DRC obtained by kMC and MPK. Left: DRC for the oxygen adsorption (filled) and desorption (empty) on cus sites (red: MPK, green: kMC). MPK reproduces the sensitivity up to the point of highest activity. Middle (reactions): In MPK only the $\mathrm{CO_{cus}} + \mathrm{O_{br}}$ reaction (black squares) has a non-zero DRC, in contrast to the kMC where the $\mathrm{CO_{cus}} + \mathrm{O_{cus}}$ reaction is rate determining. Right (CO adsorption (filled) and desorption (empty)): MPK reproduces the kMC peaks (brown) for CO ad/desorption on cus sites (green), but not quantitatively. The lower sensitivity compared to kMC is compensated by a sensitivity on the CO ad/desorption on br sites (orange). Adding both adsorption DRCs to the total sensitivity on CO adsorption, we arrive at the same results both in kMC (brown filled) and MPK (gray filled). In kMC this is identical with the DRC for the cus adsorption. The gray empty circles represent CO cus desorption + Oxygen diffusion from cus to bridge site obtained with MPK which reproduces the kMC sensitivity for the CO cus desorption (brown).

and desorption in the considered regime. Especially the divergence of the DRC for adsorption on two cus sites is present and the DRC for the corresponding desorption stays constant for low p_s^{CO} and drops to zero near the transition. This picture changes when considering the reaction events (middle panel in 3.8). kMC shows a peak structure for the $\mathrm{CO_{cus}} + \mathrm{O_{cus}}$ reaction (light blue) and no sensitivity to all other reactions. The MPK on the other hand shows no sensitivity to this reaction (dark blue), but instead for the $\mathrm{CO_{br}} + \mathrm{O_{cus}}$ reaction (black). The DRCs for the CO ad- and desorption are shown in the right panel of fig. 3.8. MPK reproduces the peak structure for the cus ad/desorption (kMC: brown, MPK: green) but a quantitative agreement can not be established. Comparing to the MFA at $p_s^{\mathrm{CO}} = 10$atm we also have a quantitative agreement for the total TOF, but in contrast the DRCs are not reproduced. The origin for the reproduced total TOF can be found, when looking at the DRC for the CO adsorption on br sites. In MPK this step is rate determining (orange), while kMC predicts no sensitivity at all. The same holds for the corresponding desorption. If we now add the DRCs for both adsorption processes, we find this sum to agree in both approaches. For MPK this is the gray line with the filled dots in the right panel of fig. 3.8. In kMC this equals the DRC for CO cus adsorption, since the other is not rate determining. Since both adsorption RCs depend in the same way on p_s^{CO}, the derivative with respect to p_s^{CO} of the total

TOF agrees for both methods kMC and MPK, respectively. For completeness we want to mention that the kMC DRC for the CO desorption can be reproduced when adding the MPK DRCs for oxygen diffusion from a cus to a br site to the DRC for CO desorption on a cus site.

3.5.2 Analytical Results

Both MFA and MPK allow for an analytical expansion in the two limits of small and high CO coverage. Again we make use of the information provided by the DRC. In the low CO pressure regime nearly all CO_2 is formed by the O_{cus}/CO_{cus} reaction. Therefore $\mathrm{TOF} = N_{\mathrm{site}} k^r P_{\mathrm{cus}}(\mathrm{CO})/2$ is a good approximation, where k^r is the rate constant for the O_{cus}/CO_{cus} reaction. We keep only those reactions with a high DRC. That is we need only to consider ad/desorption and reaction on cus sites. The MPK rate equations for the coverages of CO_{cus} and O_{cus} reduce to

$$\begin{aligned} 0 &= k^a_{\mathrm{CO}} P_{\mathrm{cus}}(*) - k^d_{\mathrm{CO}} P_{\mathrm{cus}}(\mathrm{CO}) - k^r P_{\mathrm{cus}}(\mathrm{CO}) \\ 0 &= k^a_{\mathrm{O}} P_{\mathrm{cus}}(*) - 2k^d_{\mathrm{O}} - k^r P_{\mathrm{cus}}(\mathrm{CO}), \end{aligned} \tag{3.31}$$

with the RC for ad/desorption $k^a_{\mathrm{CO}}/k^d_{\mathrm{CO}}$ for CO and $k^a_{\mathrm{O}}/k^d_{\mathrm{O}}$ for O_2. In the above equation we have set the coverage of oxygen to one. Solving this linear system we find for the TOF

$$\mathrm{TOF} = \frac{N_{\mathrm{site}} k^r k^d_{\mathrm{O}}}{k^a_{\mathrm{O}}/k^a_{\mathrm{CO}}(k^r + k^d_{\mathrm{CO}}) - k^r} \approx \frac{N_{\mathrm{site}} k^r k^d_{\mathrm{O}} k^a_{\mathrm{CO}}}{k^a_{\mathrm{O}}(k^r + k^d_{\mathrm{CO}})} \tag{3.32}$$

where we have used that $p_{\mathrm{s}}^{\mathrm{O}_2} \gg p_{\mathrm{s}}^{\mathrm{CO}}$ and therefore $k^a_{\mathrm{O}} \gg k^a_{\mathrm{CO}}$. Since RCs for adsorption depend linearly on the partial pressures we have a reaction order of one with respect to the CO partial pressure and minus one with respect to the oxygen partial pressure. Equation 3.32 (the blue line in fig 3.3) agrees very well with the kMC result but deviates earlier than the full MPK.

In the limit of high $p_{\mathrm{s}}^{\mathrm{CO}}$ the dominant reaction is the O_{cus}/CO_{br} reaction and thus $\mathrm{TOF} = N_{\mathrm{site}} k^R P_{\mathrm{cus}}(O)$ with the rate constant for the O_{cus}/CO_{br} reaction k^R. As in the low $p_{\mathrm{s}}^{\mathrm{CO}}$ limit we can restrict to the cus sites, since only the ad/desorption on these sites are rate determining. The rate equations in the MFA read

$$\begin{aligned} 0 &= k^a_{\mathrm{CO}} P_{\mathrm{cus}}(*) - k^d_{\mathrm{CO}} - 2k^R P_{\mathrm{cus}}(\mathrm{O}) \\ 0 &= k^a_{\mathrm{O}} P_{\mathrm{cus}}(*)^2 - 2k^d_{\mathrm{O}} P_{\mathrm{cus}}(\mathrm{O})^2 - 2k^R P_{\mathrm{cus}}(\mathrm{O}), \end{aligned} \tag{3.33}$$

We subtract the second from the first equation and linearize with respect to $P_{\mathrm{cus}}(*)$ and $P_{\mathrm{cus}}(\mathrm{O})$, since both are very small and $p_{\mathrm{s}}^{\mathrm{CO}} \gg p_{\mathrm{s}}^{\mathrm{O}_2}$. We find that $P_{\mathrm{cus}}(*) = k^d_{\mathrm{CO}}/k^a_{\mathrm{CO}}$. Inserting into the second equation and linearization with respect to $P_{\mathrm{cus}}(\mathrm{O})$ gives

$$\mathrm{TOF} = 2N_{\mathrm{site}} k^a_{\mathrm{O}} \left(\frac{k^d_{\mathrm{CO}}}{k^a_{\mathrm{CO}}} \right)^2 . \tag{3.34}$$

Here we have a reaction order of one with respect to $p_{\mathrm{s}}^{\mathrm{O}_2}$ and the minus two with respect to $p_{\mathrm{s}}^{\mathrm{CO}}$. Equation 3.34 agrees very well with the reference kMC simulations in the CO covered regime (purple line in fig 3.6). Surprisingly it has the same range of applicability as the underlying MFA model, although some of its premises are violated in the intermediate regime.

The analytical solutions show that at least in the considered limits the dynamics on the cus sites is most important, while the br sites either do not contribute at all to the reactivity or simply serve as a bath of CO. In fact no reaction involving a br site is rate-limiting and the analytical solutions would be identical, if we would have replaced the $\mathrm{O}_{\mathrm{cus}}/\mathrm{CO}_{\mathrm{br}}$ by the $\mathrm{O}_{\mathrm{cus}}/\mathrm{CO}_{\mathrm{cus}}$ reaction in the derivation of eq. 3.34. Thus only looking at those conditions with constant reaction orders will not help to discriminate between the complex reaction mechanism used in this study and a simpler one with only one type of site.

3.6 Summary

We have introduced the first principles statistical mechanics approach for surface kinetics. Two different methods for obtaining approximate solutions to the ME are common among researchers, the very accurate kMC and the very approximate PK. Both methods have been compared with respect to their predictions concerning total reaction rates, contributions from different reaction channels and rate determining steps. The mean-field based PK shows good agreement with the kMC data for high CO coverages of the surface but deviates more from the correct behavior the more oxygen is present at the surface. Using the DRC to identify the most critical terms in the rate equations we have been able develop a modified PK, which is reliable for the mentioned oxygen covered surface. It was shown that the formation of stable vacancy pairs was wrongly described in the standard PK. Both phenomenological approaches showed the strange behavior of being quantitatively accurate, but failing qualitatively at the same time, i.e. reproducing the total TOF correctly but predicting the shares of the different reaction channels falsely for certain reaction conditions in the intermediate regime. For the MFA this could be explained by a similar sensitivity to certain reaction steps in MFA and kMC. For the MPK it originates in an effective sensitivity pattern leading to the same pressure dependence as the correct data. This findings emphasis the limited use of phenomenological models for the targeted understanding on an atomic scale. Notwithstanding the derived accurate analytical and DRC results for the two extremes clearly indicate that catalytic activity can be assigned mostly to the cus sites.

An integration of the two phenomenological theories is straightforward. The time discretization of the (partial) differential equations describing macroscopic transport can in principle also be applied to the ordinary differential equations arising from the phenomenological theories for surface reactions. However, due to the limited range of their applicability neither PK nor MPK can be used in fluid dynamical simulations, since it is not possible to say which regime of reaction condition will prevail at the surface beforehand (compare section 5.3).

Additionally PK and MPK are only valid under very restrictive conditions on the arrangement of adsorbates. Even for the investigated simple CO oxidation problem the latter could also only be developed because of a deep and very time consuming analysis of the kMC simulations. From a modeling point of view this is undesired, since it is not clear, how to develop a computationally cheaper phenomenological model, or even if such a model exists at all. Thus these approaches can not be generalized to other reactions, even not to other CO oxidation catalysts like palladium [100]. With the methodological focus of this thesis a general purpose, model independent approach for coupling fluid flow and kMC simulations will therefore be developed in the next chapter, which is valid for a large class surface reaction and which is as efficient as the classical, rate equation based surface flow coupling.

Chapter 4

Coupling of 1p-kMC with Continuum Level Simulations

In chapter 2 we have assembled the continuum mechanical basis for reactor modeling. This was not complete in the sense that there is no explicit or implicit expression for the functional dependence of the surface reaction rates on the basic fields like composition or temperature. In chapter 3 we have dealt with the chemical kinetics of surfaces. This allows to determine reaction rates, but needs the gas phase conditions, i.e. partial pressure and temperature, at the surface as input. Since these are usually only accessible at some distance from the surface, e.g. at the inlet, we are faced with a coupled problem which needs to be solved self-consistently: in order to calculate the reaction rates we need the gas-phase conditions at the surface and the reaction rates are needed to determine these gas-phase conditions. Subject of this chapter is to propose an effective coupling scheme between the computationally expensive 1p-kMC and an existing simulation environment solving the macroscopic transport equations, e.g. a Computational Fluid Dynamics (CFD) package. This allows for an integrated modeling of first principles detailed reaction chemistry and macroscopic transport both affecting each other. We start with some physical consideration in order to relate the non-local stochastic description to the local continuum mechanical model.

4.1 Physical Model

One of the key assumptions in chapter 3 was that we deal with homogeneous systems, i.e. the surface sees everywhere the same temperature and partial pressures. In general these will vary spatially at the surface at non-equilibrium and consequently all rate constants must be considered as different although they are assigned to the same type of process. For instance the rate constant for the CO adsorption on a cus site will be different depending where the site is on the surface, due to the different partial pressures and temperatures at these places. As a consequence the solution of the Master equation (ME) and therefore all reaction rates depend on the history of uncountably many different rate constants. For homogeneous systems the number of independent RCs reduce tremendously, leading to 26 RCs for the CO oxidation at $RuO_2(110)$. Making use of the relations for the RCs (section 3.2) the history of the partial pressures and the temperature at the surface determines the current meso-state of the systems completely. Yet, the general stochastic model is non-local, since the behavior of very distant sites is coupled by the ME 3.3. Therefore the reaction rates $s_K(\underline{x}_s)$ at a certain continuum point $\underline{x}_s$ may also depend on the history of the reaction conditions at a distant surface point $\underline{y}_s$. Now a point in continuum mechanics must still be considered as a macroscopic volume, which is only vanishingly small on the length scale of pressure, temperature etc. variations. Within such a “point” we can safely assume the macroscopic fields to be spatially constant. The size of such a point is determined by the mean free path of gas phase molecules, which is of the order of 0.1 μm for near ambient pressures[5], and the employed continuum model is only valid for variations on scales much larger than this. On the other hand the lattice spacings are in the nanometer scale ($\approx$ 3Å for $RuO_2(110)$), which is smaller than the mean free path of gas phase molecules. If the influence of the rate constants some hundred lattice spacings away is negligible for the site specific coverages Π_k and pair probabilities Π_{kj}, the spatially inhomogeneous pressure and temperature field can be regarded as homogeneous on the mesoscopic level. Thus only the history of the temperature and the partial pressures at the point $\underline{x}_s$ has an influence on the reaction rates at this point. We can therefore employ the methods described in chapter 3 to describe a surface point also for inhomogeneous gas phase conditions. The physical model consists of the equation for transport in the gas and the solid phase and the jump conditions at the interface. This continuum mechanical basis is complemented by one independent master equation for each point at the surface. Thus we have at the surface

Species balance:

$$\hat{r}^{\alpha}(\underline{x}_s) = (\rho(\underline{x}_s)Y^{\alpha}(\underline{x}_s)\underline{v}(\underline{x}_s) + \underline{j}^{\alpha}(\underline{x}_s)) \cdot \underline{n}(\underline{x}_s) \tag{4.1}$$

Mass conservation in a reaction

$$\hat{r}^{\alpha}(\underline{x}_s) = \sum_{K}^{N_{\text{reac}}} m^{\alpha}\nu_K^{\alpha} s_K(\underline{x}_s) \tag{4.2}$$

Reaction rates

$$s_K(\underline{x}_s) = -\frac{N_{\text{a,surf}}N_b^a}{\nu_{\text{s},K}^{\alpha}} w_{ab}(D, C|A, B, t, \underline{x}_s)P_{ab}(A, B, t, \underline{x}_s) \tag{4.3}$$

Master equation

$$\frac{\partial}{\partial t}P(\mathbf{x},t,\underline{x}_s) = \sum_{\mathbf{y}} W(\mathbf{x}|\mathbf{y},t,\underline{x}_s)P(\mathbf{y},t,\underline{x}_s) - \sum_{\mathbf{y}} W(\mathbf{y}|\mathbf{x},t,\underline{x}_s)P(\mathbf{x},t,\underline{x}_s) \tag{4.4}$$

where the extra argument $\underline{x}_s$ in the master equation, denotes that the rate constants are evaluated with the gas phase temperature and partial pressures at $\underline{x}_s$. This means that the surface chemistry is only coupled to the gas phase at the macroscopic surface point. Coupling with other surface points is only due to macroscopic transport in the gas or solid phase.

4.2 Coupling Idea

As already stated in the previous chapter the direct solution of the ME in terms of differential equation integration is essentially impossible. If it would be possible, no explicit method for coupling would be necessary since the time discretization for the gas and solid phase partial differential equations could also be applied to the master equation allowing for an integrated simulation on the same basis for both levels, mesoscopic and macroscopic. This kind of approach can be used when the MFA or other rate equation (RE) models work. For the problem at hand we have to stick to kMC to treat the surface kinetics. A straightforward idea is to divide the time into small intervals and to solve both problems independently within each time interval. After every time interval information between the two different solution procedures is interchanged. In the next time interval the kMC is solved with the temperature and partial pressures calculated in the previous time interval by the solver for the transport problem. Vice versa the flow problem is solved with those reaction rates obtained by kMC at the end of the last time interval. Such a direct integration of the stochastic kMC into a fluid simulation is possible[118, 62] but can experience severe problems. kMC allows already the simulation of much longer time intervals compared to microscopic level simulation techniques like molecular dynamics simulations, which integrate Newton's equations of motion. However, it is still computationally very expensive, much more than the solution of the rate equations, since it is a mesoscopic simulation method generating a series of elementary steps. For instance, the CPU time spent for simulating the steady state in chapter 3 was at least 4 orders of magnitude larger for kMC than for the numerical solution of the RE. With the transport problem describing the macroscopic time evolution the necessary time step for the discretization of the flow problem will be several orders of magnitude larger than the kMC step. Further the kMC is a stochastic method and all results will have a certain amount of fluctuations, while the macroscopic equations of motion describe the evolution of probabilistic averages. These show by definition no microscopic fluctuations. So the CPU time spent is not only determined by the real time, which shall be simulated, but can further increase because the statistical error of the kMC

averages needs to be reduced[88]. From a practical point of view this reduction becomes even more important, since derivatives of the jump (boundary) conditions are often required for the numerical integration of the transport problem. The error of numerical derivatives can easily explode, when the averages have a too large statistical error. In consequence this can lead to a non-convergence of the flow solver even though the problem would be numerically undemanding, if accurate derivatives would be available. This high complexity of the direct approach makes it necessary to restrict to one-dimensional problems or to parallelize the computer code, so that the ME for every grid point at the catalyst surface is solved independently by kMC on an own processor. There have been different attempts to increase the efficiency of the direct approaches, for instance by on the fly adaptive tabulation[117], and to overcome the numerical stability problems of the direct approaches [101].
We circumvent all the mentioned problems by employing a divide-and-conquer strategy. For stationary simulations and in the quasi-stationary approximation only steady-state reaction rates are needed. Eventually, the surface reaches a unique steady state for fixed reaction conditions at the surface regardless of its initial meso-state. In other words in a steady state the functional dependence on the history of partial pressures and temperature will reduce to the dependence on the current temperature and current partial pressures at the surface

$$s_K(\underline{x}_s) = s_K(p_{\mathrm{s}}^{\alpha}(\underline{x}_s), T_{\mathrm{s}}(\underline{x}_s)). \tag{4.5}$$

This finding thus dictates to run the kMC simulations and to obtain the reaction rate function $s_K(p_{\mathrm{s}}^{\alpha}, T_{\mathrm{s}})$ before the actual flow simulation. This function is then used for the jump conditions instead of the expensive kMC simulations. Generating this data before the actual flow simulation allows for a trivial parallel processing and to run the kMC simulation until the statistical error is negligible.

The only problem is how to convert a finite number of kMC results into a continuous representation for the s_K. Considering the kMC just as some kind of (computer) experiment one could fit a rate equation model to the kMC data. This approach allows to reduce the CPU time spent for the jump conditions to the value of the commonly employed rate equations. Nevertheless it also requires the solution of a nonlinear set of equations, at least. It is therefore still quite expensive and it will never reproduce the kMC data to its fully accuracy, i.e. there will always be an finite error produced by the RE model regardless how many kMC simulations one performs as input. Also such models can hardly be refined since improving the fit for a certain set of reaction conditions leads in general to a worse representation for other reaction conditions. Another drawback is that a RE model has to be proposed, which is capable to reproduce the effects of the stochastic model underlying the kMC data. Due to the high dimensionality of the latter model it is in general much more flexible than any low-dimensional RE model, that is a RE model might not be able to reproduce even just the phenomenology of the kMC data. We conclude, that this approach can be become very time-consuming. With these drawbacks in mind we decide to apply another approach, which is much less demanding in the sense that it requires much less human endeavor. We will simply use an interpolation technique instead. Doing so allows for a numerically exact representation of the reaction rates, i.e. it is possible to come arbitrarily close to the real reaction rate function, enough data points provided. Thus despite the made preconditions this is a model free approach, very different from the common RE based approach. Such an interpolation is usually fast to evaluate and can be easily coupled to any kind of flow solver. In the end the CPU time for calculating reaction rates in the flow simulation is of the order of the value for the RE based approach. Actually we expect an interpolation to be even faster for this purpose[121].

4.2.1 Interpolating 1p-kMC Data

Interpolation techniques can be divided into two groups: grid based and gridless methods. Grid based methods like Splines[22] can usually only be applied to problems with a very moderate number (≤ 4) of independent variables. For higher dimensions either the amount of necessary grids points explodes or the storage requirement for the data structure defining the grid becomes intractable. For the here treated CO oxidation with at maximum 4 independent arguments[1] using grid based methods is still feasible, but the problem becomes too high-dimensional as soon as other constituents are added to the gas phase, that can adsorb on the surface. Aiming rather on developing a coupling method applicable also to more general cases we will therefore employ a grid-less method, where the kMC data for the interpolation can be obtained at any reaction conditions, which are not necessary located on a grid. This makes the method applicable to higher dimensions than three, where grid based methods suffer from a bad scaling. An overview about such “Scattered Data Interpolation”[2] methods can be found in [1]. We will employ a local modified Shepard interpolation for its representation properties, i.e. the capacity to reproduce certain classes of functions exactly. Another advantage is its efficiency, scaling linearly with the number of interpolation points for the initial construction of the interpolation and constant for every subsequent evaluation of the interpolation[3].

Before the actual construction of the interpolant it is useful to transform the independent and dependent variables. The choice of a logarithmic scale for the reaction rates and the partial pressures and an inverse representation of the temperature combines many advantages. First a logarithmic scale flattens peaked structures of the reaction rate function making the interpolation easier. Remember that only the adsorption rate constants depend linear on the partial

---

[1] These are the the partial pressures of CO, O_2 and CO_2 and the temperature.

[2] Although there also exist grid based methods which can interpolate scattered data. Nevertheless these methods require a data structure defining the grid, which storage requirement explodes for higher dimensions

[3] For the here employed code this strictly holds only for equally distributed data

pressure, so that

$$\frac{\partial \ln s_K}{\partial \ln p_{\mathrm{s}}^{\alpha}} = \sum_{i}^{N_{\mathrm{ad.}}^{\alpha}} \frac{\partial \ln s_K}{\partial \ln w_i} \frac{\partial \ln w_i}{\partial \ln p_{\mathrm{s}}^{\alpha}} = \sum_{i}^{N_{\mathrm{ad.}}^{\alpha}} X_{\mathrm{rc},K}^{i} \tag{4.6}$$

where $N_{\mathrm{ad.}}^{\alpha}$ is the number of different adsorption reaction of the species α and $X_{\mathrm{rc},K}^{i}$ is the DRC of such an adsorption. The (negative) derivative of the reaction rate with respect to the inverse temperature (multiplied by the Boltzmann constant) is the apparent activation barrier E_{app}. It can be well approximated with[79]

$$E_{\mathrm{app}} = -\frac{\partial \ln s_K}{\partial 1/kT} \approxeq \sum_{i}^{N_{\mathrm{reac}}} X_{\mathrm{rc},K}^{i} \Delta E_i \tag{4.7}$$

From the above equations we immediately see that in this representation the reaction rates behave linear in regions with constant sensitivity. For the problem at hand we observe such a behavior in most of the considered reaction conditions (compare with chapter 3). With the typical large differences in the activation barriers for different processes we also expect this behavior to be rather generic for heterogeneous catalysis.

We specifically use the QSHEP3 code for the interpolation. It implements a modified quadratic Shepard interpolation developed by R. Renka[93, 92]. Suppose we have N_{data} function values f_j at the points $\mathbf{X}_j \in \mathbb{R}^D$ of a function $f(\mathbf{X})$, which is going to be interpolated. The basic idea of the modified Shepard interpolation[128] is to construct an approximate Taylor expansion $Q_i(\mathbf{X})$ at each interpolation point $\mathbf{X}_j$

$$Q_j(\mathbf{X}) = f_j + \sum_{a}^{D} \left(\frac{\partial f}{\partial X_a}\right)_{\mathbf{X}_j} (\Delta \mathbf{X}_j)_a + \sum_{ab}^{D} \left(\frac{\partial^2 f}{\partial X_a \partial X_b}\right)_{\mathbf{X}_j} (\Delta \mathbf{X}_j)_a (\Delta \mathbf{X}_j)_b. \tag{4.8}$$

with $\Delta \mathbf{X}_j = \mathbf{X} - \mathbf{X}_j$. The index $\mathbf{X}_j$ at the derivatives means that they are evaluated at at this value of the independent variable $\mathbf{X}$. These Taylor expansions are then superposed to the representation $S(\mathbf{X})$ of the original function $f(\mathbf{X})$

$$S(\mathbf{X}) = \sum_{i} Q_i(\mathbf{X}) W_i(\mathbf{X}), \tag{4.9}$$

where the weights $W_i(\mathbf{X})$ are a so-called Shepard partition of unity, i.e. $\sum_i W_i(\mathbf{X}) = 1$ and $W_i(\mathbf{X}_j) = \delta_{ij}$. This ensures the necessary interpolation property $S(\mathbf{X}_j) = f(\mathbf{X}_j)$. When the weighting function $W_i(\mathbf{X})$ is only nonzero within a small (hyper-)sphere with center $\mathbf{X}_i$ (a so called cloud), the method is local, i.e. given $\mathbf{X}$ only data points nearby will have an influence on the outcome of the interpolation. In the local formulations the weights have the form

$$W_i(\mathbf{X}) = \frac{\upsilon_i(\mathbf{X})}{\sum_j \upsilon_j(\mathbf{X})}, \text{ with } \upsilon_i(\mathbf{X}) = \frac{\varsigma_i(|\mathbf{X} - \mathbf{X}_i|)}{|\mathbf{X} - \mathbf{X}_i|^n}, \tag{4.10}$$

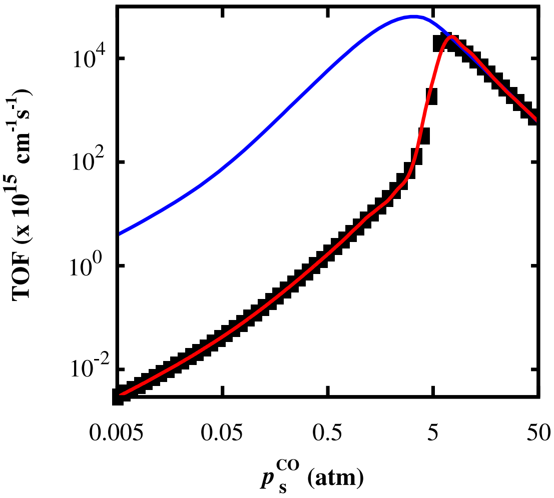

Figure 4.1: Comparison of MFA (blue line) and interpolation (red line) with raw kMC data (black squares). Shown is the TOF for varying p_s^CO and constant T_s=600 K and $p_\mathrm{s}^{O_2}$=1atm. The MFA deviates largely from the accurate kMC results. The employed interpolation shows a small deviation, where the TOF shows a rapid change, but else it agrees very well with the raw kMC data.

where $\varsigma_i(|\mathbf{X}-\mathbf{X}_i|)$ is finite and monotonically decreasing until it becomes zero for $|\mathbf{X}-\mathbf{X}_i| \geq R_i$, where R_i is the radius of the cloud around $\mathbf{X}_i$. Renka's method is obtained with $n = 2$ and $\varsigma_i(\mathbf{X}) = (R_i - |\mathbf{X}-\mathbf{X}_i|)_+^2$, where the + indicates that the content of the brackets is to be replaced by zero if negative. The radius R_i is determined such that N_q nearest neighbors are in the sphere. The approximate Taylor polynomial $Q_i(\mathbf{X})$ is determined by fitting the derivatives at $\mathbf{X}_i$ to the data of the N_f nearest neighbors of $\mathbf{X}_i$ in a weighted least squares sense[128]. From its construction this quadratic modified Shepard method interpolates second order polynomials exactly. Due to the local structure a (sub)domain Ω with such a polynomial dependence should also be exactly interpolated away from its boundaries. Only a boundary shell is affected by data points outside the domain, either by their clouds overlapping with Ω or because they are included in the fitting for points inside Ω. Together with the above discussed choice for the internal representation of the data this interpolation property implies that reactivity data can be represented with a minimum number of points. Especially for higher dimensions we expect this to be necessary. For the here discussed CO oxidation problem with suppressed CO_2 adsorption we can easily afford a dense enough grid.

4.3 Settings for the CO Oxidation at RuO_2

In practice we use a grid with 25 K spacings for the temperature range 400 K < T_s < 850 K and logarithmic spacing for the partial pressures with 30 spacing for 10^{-6} atm < $p_\mathrm{s}^{\mathrm{O}_2}$ < 10^2 atm and 42 spacings for 10^{-5} atm < p_s^CO < 10^2 atm. The actual interpolation is performed with the recommended default settings for the logarithm of the TOF as a function of the logarithm of the partial pressures and the inverse temperature. The independent variables $\{\log p_\mathrm{s}^\mathrm{CO}, \log p_\mathrm{s}^{\mathrm{O}_2}, 1/T_s\}$ are scaled such that the distance between neighboring points is in the size of one.

In figure 4.1 the interpolation is compared with raw kMC data not used for the interpolation for varying $p_{\mathrm{s}}^{\mathrm{CO}}$ and constant $T_s = 600\mathrm{K}$ and $p_s^{\mathrm{O}_2} = 1\mathrm{atm}$. The employed interpolation (red line) shows only small deviations in the pressure range where the TOF changes most rapidly. Note that this rapid change occurs in an interval of partial pressures, which is in the range of the employed grid spacing and we can not expect that this nonlinear behavior will be resolved with only a negligible error. At the expected error in the rate constants due to the first principles input this relatively small and localized mismatch is tolerable.

4.4 Strengths and Limitations

The presented very efficient approach is easy to implement and can in principle be applied to arbitrary reactor geometries. Very different from the direct approach it has no additional computational overhead for higher dimensions, i.e. the number of necessary 1p-kMC simulations is independent of the number of surface grid points in a simulation. For one-dimensional flow simulations as will be presented in chapter 5 the approach offers the possibility to search a wide parameter space of flow conditions. This efficiency comes of course not at no cost. A unique steady state must exist for all reaction conditions and if applied to transient problems the approach relies on the quasi-stationary approximation. For unique steady states the results differ from the most accurate direct method only by the numerical error in the interpolation, but models the same physics. Given the possibility to refine the interpolation with additional data this approach lies in between the direct and the rate equation approach. One might argue that for transient problems rate equations might serve better since they in principle also apply for this case. When the MFA is working one thus should switch to rate equations, of course. For the here presented reaction and many other this is not the case. We note however, that in practice RE models are often fitted to stationary data and we can not expect a proper time dependent behavior for an effective model obtained in this way. Even when fitting to time dependent data it is not ensured, that the RE model is able to reproduce a time series correctly, even if partial pressures and temperature have not left the range of reaction conditions, the RE model was fitted to. Thus RE models must in all cases be considered as the least accurate approach and should only be used, when either the MFA reflects the mesoscopic level properly - not just the macroscopic accessible reaction rates - or when there exists no appropriate mesoscopic model due to the high complexity of the catalyst, e.g. a complex industrial catalyst.

Chapter 5

A Simple Reactor Setup: Stagnation Flows

We will apply the methodology developed in the previous chapters to a simple reactor geometry suitable to discuss mass and heat transfer effects in *in situ* experiments. This very important class of reactor setups is the so-called stagnation flows. The flow geometry is depicted in figure 5.1. A gas mixture of CO, O_2, and CO_2 streams from a shower-head-like inlet towards the flat-faced model catalyst. The catalyst is a disk parallel to the inlet with a thickness d. We want to assume that at the bottom side of the catalyst either the temperature T_{cat} or the (normal) heat flux q_{cat} can be controlled. Composition, temperature, pressure and velocity are known at the inlet, which is at a distance L away from the catalyst's surface. The shower head-like inlet ensures that there velocity, partial pressures, and temperature do no vary perpendicular to the flow

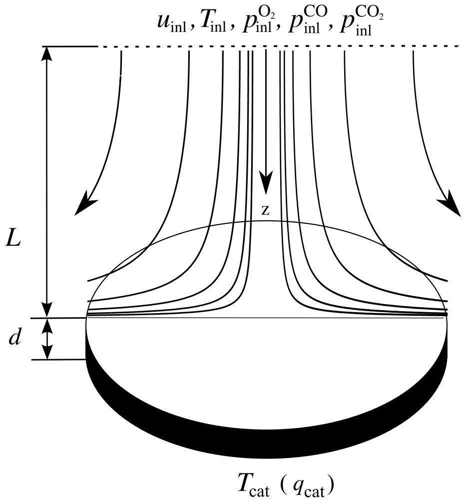

Figure 5.1: Schematic view of a stagnation point configuration: The gas streams from the inlet (dashed line) towards the flat-faced catalyst of thickness d. Inlet-surface distance is L. At the inlet partial pressure, temperature and velocity are controlled. At the backside of the catalyst temperature or heat flux are controlled.

direction. For simplicity we will restrict to stationary stagnation flows. The importance of stagnation reactors in heterogeneous catalysis originates not from the application in industrial reactors but from the simplicity of their analysis. Due to the flow geometry they enable highly homogeneous reaction conditions at the surface, which is absolutely necessary to gain insight into the targeted intrinsic reactivity in near-ambient environments, e.g as a function of partial pressures and temperature at the surface. If one considers e.g. a flow geometry where the stream of reactants would approach the surface from the side – thus in some sense an opposite scenario to the here discussed perpendicular stagnation flow – then this is clearly not the case. Due to the on-going conversion of reactants into products the gas-phase composition close to the surface would gradually change across the lateral extension of the single crystal. If there are non-negligible heat transfer limitations, this goes hand in hand with a non-uniform temperature profile parallel to the surface. Under such conditions, making a defined assignment of observed turnovers to specific pressures and temperatures becomes essentially intractable. In contrast, in the stagnation flow geometry at least the entire center part of the active surface sees the same gas phase, thereby facilitating the analysis. From a theoretical perspective the cylindrical symmetry problem reduces the computational complexity. And for flat-faced singly crystal surfaces it is indeed one of the few highly symmetric flow geometries. Other flow geometries showing high symmetry differ mostly in the shape of their inlet, e.g. the impinging jet geometry[60] has a point like inlet rather than a sieve. Neglecting edge effects, i.e. the finite lateral extension of the model catalyst, the stagnation flow profile can effectively be described by a one-dimensional boundary-value problem[32, 19, 58]. This eases the discussion of the influence of the reactor setup significantly and allows to extract the relevant physics without being riddled by algebra and numerics.

5.1 The Stationary Stagnation Flow Equations

In the following we use an axial coordinate system with z being the axial coordinate perpendicular to the catalyst's surface. The radial coordinate will be denoted with r. We put the origin at the inlet and the z-axis points towards the catalyst. We restrict to the flow situations with no circumferential motion. In the derivation the key assumption is that variations in radial direction of partial pressure, temperature and axial velocity are much smaller than in axial direction at least near the symmetry axis. Starting with the gas phase equations in the LMA eqs. 2.51 - 2.54 a lowest order expansion in the radial dependence of ρ, the axial velocity component u, Y^α and T leads to[57]

Mass

$$V = \frac{1}{2}\frac{1}{\rho}\frac{d}{dz}\rho u, \tag{5.1}$$

Axial momentum:

$$\rho u \frac{du}{dz} = -\frac{d\tilde{p}}{dz} + \frac{4}{3}\frac{d}{dz}\left[\mu\frac{du}{dz} - \mu V\right] + 2\mu\frac{dV}{dz} \tag{5.2}$$

Radial momentum:

$$\rho u \frac{dV}{dz} + \rho V^2 = -\Lambda_r + \frac{d}{dz}\mu\frac{dV}{dz} \tag{5.3}$$

Energy (gas phase):

$$\rho c_p u \frac{dT}{dz} = \frac{d}{dz}\kappa\frac{dT}{dz} - \sum_\alpha c_p^\alpha j_z^\alpha \frac{dT}{dz} \tag{5.4}$$

Species:

$$\rho u \frac{dY^\alpha}{dz} = -\frac{dj_z^\alpha}{dz}, \tag{5.5}$$

LMA:

$$\sum_\alpha \frac{\rho Y^\alpha}{M^\alpha} RT = p_{\text{ref}} = p_{\text{inl}} = \text{const.} \tag{5.6}$$

where j_z^α is the axial component of the mass flux. The radial velocity component v enters the equations only via the scaled velocity $V = v/r$, which depends only on the axial coordinate z as all other occurring fields in equations 5.1-5.6. Within the stagnation flow approximation the radial pressure curvature $\Lambda_r = \frac{1}{r}\partial_r \tilde{p}$ is constant but unknown. The above equations therefore represent an eigenvalue problem, which solution fulfills the three-dimensional gas phase equations in the LMA but in general not the BC at the reactor walls. It can therefore only be considered as a good approximation near the symmetry axis. Due to the LMA the axial momentum balance 5.2 is decoupled from the other equations. We can determine all fields without considering it except for the the dynamic pressure $\tilde{p}$. It can be obtained after calculating fields ρ, Y^α, T, u, and V. A more detailed discussion on stagnation flows can be found in the book of Kee, Coltrin and Glarborg [57].

The above set of differential equations needs to be closed by appropriate boundary conditions. We need two boundary conditions each for the second order differential equations, which are the radial momentum, the partial mass and the energy balances. Further we need one boundary condition each for the first order balance of total mass and an additional one in order to determine the unknown pressure curvature. Further the total pressure at the inlet must be determined. At the inlet we control composition, temperature and density as well as the inlet velocity and we have the boundary conditions

$$\rho(z=0) = \rho_{\text{inl}}, \tag{5.7}$$

$$u(z=0) = u_{\text{inl}}, \tag{5.8}$$

$$T(z=0) = T_{\text{inl}}, \tag{5.9}$$

$$Y^{\alpha}(z=0) = Y^{\alpha}_{\text{inl}}, \tag{5.10}$$

$$V(z=0) = 0 \tag{5.11}$$

where the last condition is implied by the sieve-like inlet, which does not allow for radial flow. The first condition serves for determining p_{inl}, the second as the boundary condition for the mass balance, while the other three provide the first of two boundary conditions for the radial momentum, the partial mass and the energy balances, respectively. For the other boundary conditions defined at the surface we employ the non-slip boundary condition and continuous temperature condition (see section 2.3.2) and the surface balances for partial and total mass and energy. Thus we have the additional boundary conditions for the gas phase equations

$$u(z=L) = 0, \tag{5.12}$$

$$V(z=L) = 0, \tag{5.13}$$

$$q_z(z=L) = q_{z,\text{solid}}(z=L) \tag{5.14}$$

$$j^{\alpha}_z(z=L) \;=\; -\hat{r}^{\alpha} \;=\; -m_{\alpha}\nu_{\alpha}\text{TOF}, \tag{5.15}$$

where $q_z(z=L)$ and $q_{z,\text{solid}}(z=L)$ are the axial components of the heat fluxes in the gas and the solid phase at the surface, respectively . The first boundary condition serves for the determination of the eigenvalue and the other as remaining boundary conditions for radial momentum, the partial mass and the energy balances, respectively. In order to determine the solid heat flux we need to solve the heat transport problem in the sample. Since in the stagnation flow setup the temperature is uniform at the catalyst's surface, we do not expect radial variation of the temperature within the catalyst. This leads to the one dimensional Laplace equation

$$\frac{d}{dz}\kappa_{\text{solid}}\frac{dT_{\text{solid}}}{dz} = 0 \tag{5.16}$$

which shows that in the sample the temperature varies linearly between surface $(z = L + d)$ and sample backside $(z = L)$.

In this study we consider two extreme conditions at the backside of the sample, the completely thermally isolated sample allowing no heat flux through the backside of the sample (adiabatic limit, $q_{\text{cat}} = 0$) and the thermally well connected sample ensuring the same temperature at the backside of the sample as at the inlet (isothermal limit, $T_{\text{cat}} = T_{\text{inl}}$). We have the two boundary conditions

Isolated sample

$$q_{z,\mathrm{solid}}(z) = 0, \tag{5.17}$$

Connected sample

$$q_{z,\mathrm{solid}}(z) = \frac{\kappa_{\mathrm{solid}}}{d}(T(z = L) - T_{\mathrm{cat}}), \tag{5.18}$$

where we have made use of the solid heat flux being constant in z for the considered one dimensional heat conduction. With experimental setups never being perfectly heat isolated or allowing for an ideal heat dissipation these two idealized boundary conditions form the two limits between which the real experiment will take place. We note that for the isolated sample there could be a small influence of the radiative heat loss, since we now suppress the heat conduction in the solid (see section 2.3.2). We nevertheless skip the corresponding terms, because we want to study the limiting case with as many dissipation channels turned off as possible.

5.2 Numerical Solution

The stagnation flow equations can be transformed into a semi-explicit system of differential-algebraic equations (DAE)

Gradients:

$$\frac{d}{dz}V = \frac{A}{\mu}, \tag{5.19}$$

$$\frac{d}{dz}\rho = C, \tag{5.20}$$

$$\frac{d}{dz}T = \frac{F}{\kappa}, \tag{5.21}$$

$$\frac{d}{dz}Y^{\alpha} = G^{\alpha}, \tag{5.22}$$

Continuity:

$$\frac{d}{dz}u = -2V - \frac{uC}{\rho}, \tag{5.23}$$

Eigenvalue:

$$\frac{d}{dz}\Lambda_r = 0, \tag{5.24}$$

Radial Momentum:

$$\frac{d}{dz}A = \rho u \frac{A}{\mu} + \rho V^2 + \Lambda_r, \tag{5.25}$$

Species:

$$\frac{d}{dz}j_z^\alpha = -\rho u G^\alpha, \tag{5.26}$$

Energy:

$$\frac{d}{dz}F = \rho u c_p \frac{F}{\kappa} + \sum_\alpha^N c_p^\alpha j_z^\alpha \frac{F}{\kappa}, \tag{5.27}$$

LMA ($\frac{dp_\mathrm{ref}}{dz} = 0$):

$$0 = \frac{\partial p}{\partial \rho} C + \frac{\partial p}{\partial T}\frac{F}{\kappa} + \sum_\alpha \frac{\partial p}{\partial Y^\alpha} G^\alpha, \tag{5.28}$$

where the concentration gradient G^α is determined from the mass fluxes using the Stefan-Maxwell equations 2.45. Making use of $\sum_\alpha Y^\alpha = 1$ these are $2N_\mathrm{spec}+5$ differential equations and one algebraic equation. ρ, V, u, T, Λ_r, A, F, Y^α and j_z^α are called the differential components and C the algebraic component. The DAE has the index one[4], since the algebraic constraint eq. 5.28 can be inverted with respect to the density gradient C. Although we can easily eliminate the algebraic constraint we stay with this formulation mainly for historic reasons. The $2N_\mathrm{spec} + 5$ needed boundary conditions are given by eqs. 5.7-5.15.

We numerically solve the DAE boundary value problem using the **COLDAE** package by U. Ascher and R. Spiteri [4]. It uses piecewise orthogonal collocation at Gaussian points and has an adaptive mesh strategy allowing for an error-controlled solution of the DAE. We have selected the default option controlling the number of intermediate points and an initial equidistant mesh with 10 spacings. In all simulations we have used a tolerance of 10^{-4} for each differential component. In order to improve the stability and have full error control, appropriate units for all variables, dependent or independent, are employed internally. The employed units are the inlet-surface distance L for length, and for the velocity, density, and mass fractions their values at the inlet. The employed temperature scale T_scale is Kelvins. We use the representation $(T - T_\mathrm{inl})$ for the temperature, so that this re-normalized temperature is always zero at the inlet. The mass fluxes, heat flux, and density gradient are expressed in multiples of $\frac{D^\alpha_\mathrm{eff,inl} Y^\alpha_\mathrm{inl}}{L}$, $\frac{\kappa_\mathrm{inl} T_\mathrm{scale}}{L}$, and $\frac{\rho_\mathrm{inl}}{L}$, respectively, where $D^\alpha_\mathrm{eff,inl}$ is the mixture averaged diffusion coefficient[57]. Finally, the radial pressure curvature Λ_r and $\mu\frac{dV}{dz}$ are scaled with $100\mu_\mathrm{inl}\frac{u_\mathrm{inl}}{L^3}$ and $\mu_\mathrm{inl}\frac{u_\mathrm{inl}}{L^2}$, respectively.

The software uses a (damped) Newton strategy to find a solution starting from an initial guess. The initial guess for first simulation was a third order

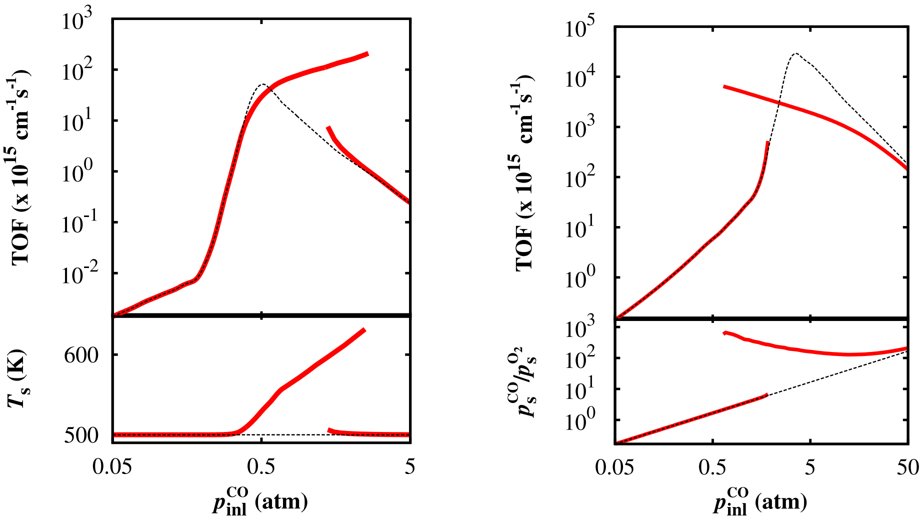

Figure 5.2: Comparison of intrinsic catalytic activity (TOF,black dashed line) with observable TOFs (red solid line) when accounting for macroscopic transport effects in the prescribed stagnation flow reactor for CO oxidation at RuO$_2$(110) with $L = 1$ cm, $p_{\text{inl}}^{\text{O}_2} = 0.3$ atm, $u_{\text{inl}} = 1$ cm/s and varying $p_{\text{inl}}^{\text{CO}}$ at the inlet. Left: $T_{\text{inl}} = 500$K, and suppressed heat flux at the backside of the $d = 1$mm thin single-crystal. This allows the system to sustain a high-activity branch for more CO-rich conditions than the nominal most active state. For this branch the surface temperature, T_{s} shown in the lower panel, is significantly increased. Right: Same as left, but for an ideal heat coupling at the backside of the crystal ($T_{\text{cat}} = T_{\text{inl}} = 600$K). Now the partial pressures change significantly between inlet and surface, while there is hardly any heat up of the surface. The lower panel shows the corresponding partial pressure ratio directly at the surface and illustrates that in the high-activity branch the surface effectively sees a more CO-rich gas phase compared to the nominal inlet composition.

polynomial for u, which fulfills the boundary conditions, and constant ρ, T and Y^α. The remaining unknowns are approximated according to these assumptions. For subsequent simulations we use the result of the previous simulation, when appropriate. In this case we make use of the adapted mesh from the previous simulation, which has been coarsened to contain only half as many grid points as initially.

5.3 Results

In order to assess the effect of the heat connection of the catalyst sample we consider the afore mentioned two reactor setups, the perfectly heat isolated sample allowing no heat flux at the backside of the sample and the perfectly heat connected sample, where it is ensured that the catalyst has always the same temperature at its backside as the inlet. These two setups form more or less the limiting cases for real experiments, where none of both cases are ever realized. There will always be some some heat flux through the backside and a heat up of the backside above the nominal inlet temperature can also hardly be suppressed. We will consider more or less the same type of computational experiments as in chapter 3, i.e. fixed temperature and oxygen partial pressure in conjunction with varying CO partial pressures. Differently we can now display all results depending on the applied reaction conditions at the inlet and need not to know the partial pressures and the temperature at the surface. Therefore our simulation results reflect rather what is measured in an experiment than the pure kMC simulations presented in chapter 3, which deliver only the intrinsic activity. In all our simulations we set $p_{\mathrm{inl}}^{\mathrm{CO}_2} = 10^{-5}$atm in order to mimic a highly pure mixture of CO and O_2 entering the reactor. As default setting we choose $L = 1$cm, $u_{\mathrm{inl}} = 1$cm/s and $d = 1$mm, which are representative for real reactors. Nevertheless we will later on vary these values in order to study their influence on the observed effects.

5.3.1 Limit 1: The Thermally Isolated Sample

First we consider a thermally well isolated sample allowing no heat flux at the its backside. The observed catalytic activity for $p_{\mathrm{inl}}^{\mathrm{O}_2} = 0.3$atm, $T_{\mathrm{inl}} = 500$K and varying $p_{\mathrm{inl}}^{\mathrm{CO}}$ is depicted in the upper left panel in figure 5.2 as solid red line. It coincides with the intrinsic catalytic activity (dashed black line) for low TOFs, but deviates more and more for higher TOFs. With a deviation of up to two orders of magnitude the observed TOF also shows a complex behavior with two stationary solutions. We have an active branch where the observed activity increases monotonically with $p_{\mathrm{inl}}^{\mathrm{CO}}$. At 1.5 atm a second, low active branch sets in following the intrinsic activity with decreasing TOF for increasing partial pressure. The two branches coexist until 2.5 atm are reached. For higher partial pressures the low active branch is the only stationary solution found. This bi-stability is completely absent in the intrinsic catalytic activity and is therefore a qualitatively new feature arising due to the coupling of macroscopic transport and surface chemistry. With the partial pressures staying unchanged between inlet and surface these effects are solely driven by an increase of the surface temperature T_{s} of up to 120 K above the nominal inlet temperature as shown in the lower left panel in figure 5.2. This temperature increase allows the coupled reactor-surface system to reach a higher reactivity than the intrinsic one.

5.3.2 Limit 2: The Thermally Well Connected Sample

Changing to the well heat connected sample with a thickness of 1mm and increasing the applied temperature to 600 K the observed catalytic activity is very different from the intrinsic as in the previous case, again showing bi-stability (see upper right panel in figure 5.2), in this case in a range from a nearly stoichiometric composition up to a CO partial pressure of 1.8 atm. The deviation

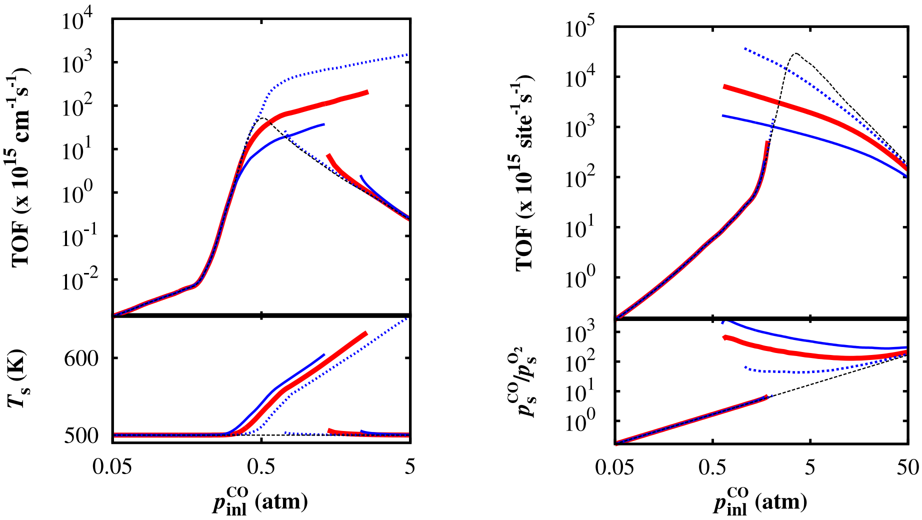

Figure 5.3: Same as fig. 5.2, but for different inlet-surface distance L. Shown are the results for $L = 1$ mm (dotted blue line), $L = 1$ cm (solid red line), and $L = 10$ cm (solid blue line). It shows that deviation from the ideal behavior sets in earlier for larger inlet-surface distance, both for the TOF and the surface temperature (isolated sample, left) or partial pressure ration (isothermal limit, right).

of the observed catalytic function from the intrinsic one is up to three orders of magnitude for the active branch. Now the highly active branch is stable for higher CO partial pressures and the TOF decreases for increasing $p_{\mathrm{inl}}^{\mathrm{CO}}$, i.e. the opposite behavior as for the thermally isolated sample. Analogously the low active branch is only stable for low pressures and the TOF increases with $p_{\mathrm{inl}}^{\mathrm{CO}}$. Also now the highest observed reactivity is lower than the intrinsic maximum. Different from the thermally isolated sample there is nearly no heat up of the surface in this case, although now orders of magnitude higher TOFs are reached. Here the observed effect is driven by mass transfer leading to very different partial pressures p_{s}^{α} at the surface from those applied. This can easily be seen from the ratio of CO and O_2 partial pressures displayed in the lower right panel in figure in 5.2. For the high activity branch this ratio deviates largely from ideal case (dashed black line), where the partial pressures do not change between inlet and surface. The gas phase at the surface is much more CO-rich than at the inlet. At such conditions the catalyst is generally more active than at the nominal inlet composition, where the catalyst is essentially dead.

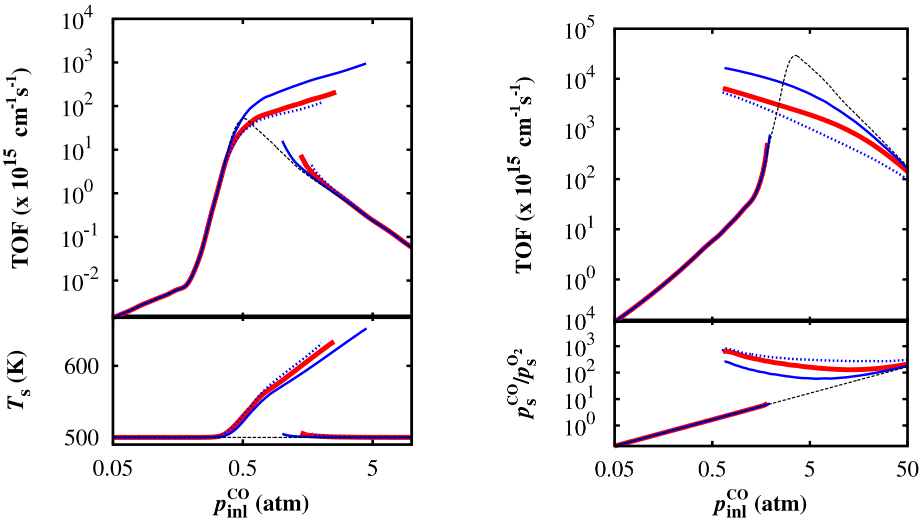

Figure 5.4: Same as fig. 5.2, but with different inlet velocities. Shown are the results for $u_{\mathrm{inl}} = 1$ mm/s (dotted blue line), $u_{\mathrm{inl}} = 1$ cm/s (solid red line), and $u_{\mathrm{inl}} = 10$ cm/s (solid blue line). A larger inlet velocity leads to later deviation from the ideal behavior.

5.3.3 Dependence on the Inlet Surface Distance and Inlet Velocity

Next we examine the effect of the inlet surface distance on the observed catalytic activity. We perform the same computer experiments as before but for different L. The results are displayed in figure 5.3, where the solid and the dashed blue lines correspond to $L = 1$cm and $L = 10$cm. The results change quantitatively, but the qualitative picture stays unchanged. In both cases a smaller L has generally a larger observed TOF as result, but also the deviation from the ideal behavior does not set in until higher TOFs. Correspondingly the surface temperature and the partial pressure ratio are closer to the ideal case for the same inlet partial pressure.

Changing the inlet velocity by an order of magnitude has also only a quantitative effect, as can be seen in figure 5.4. The solid and the dashed blue lines correspond to $u_{\mathrm{inl}} = 1$mm/s and $u_{\mathrm{inl}} = 10$cm/s, respectively. The dependence on the inlet velocity is very similar to that on the inlet surface distance only with opposite sign. A smaller u_{inl} leads to a stronger heat up of the surface and also the deviation of the partial pressure ratio from the ideal case is more pronounced.

Additionally to the dependence on L and u_{in} there is a dependence on the sample thickness d in the isothermal case. Changing d to 0.1mm and 1cm respectively, the temperature difference between inlet and surface changes proportionally. Still, in all cases it stays so small that the change of D has virtually

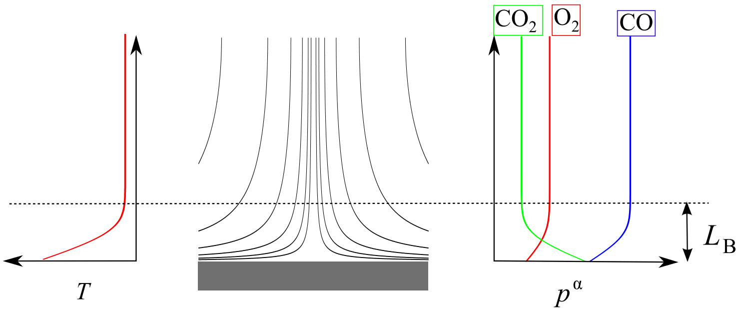

Figure 5.5: Illustration of the temperature and pressure variations. Diffusion and heat conduction take place only in a boundary layer above the surface. This boundary layer expands when the inlet velocity is decreased, filling the whole gap between inlet and surface for the limit $u_{\text{inl}} \to 0$. Opposite it shrinks when the inlet-surface distance L is decreased.

no effect on the observed catalytic activity.

5.4 Discussion

5.4.1 Formation of a Boundary Layer

In order to discuss the overall results presented in the previous section we need to have a closer look on what is going on in the reactor, i.e. how do the fields of partial pressure, temperature etc. behave between inlet and catalyst. In figure 5.5 prototypical variations of the partial pressures and temperature are shown. It is seen that heat conduction and diffusion only take place in a boundary layer (BL) of thickness L_{B} above the surface (below the dashed line). That is only within this region we find non-vanishing gradients of temperature and partial pressures. This is due to the convective nature of the transport; the gas streams towards the surface and the chemical reactions at the surface have no influence on the fields far away, since the heat and species move with flow which overcomes any non-convective transport. When the axial velocity approaches zero near the surface, diffusion and heat conduction set in, since they are now of similar size as the convective transport. With this knowledge the behavior for varying L and u_{inl} is easily explained. A higher inlet velocity compresses the boundary layer stronger thereby enabling higher gradients for the same difference between inlet and surface partial pressures and temperature, respectively. Since the TOF is proportional to these gradients at the surface, the deviation from the ideal behavior is smaller for higher velocities, i.e. we observe a smaller difference between inlet and surface partial pressures respectively temperature for the same value of the TOF. Similarly a smaller inlet surface distance leads to a smaller boundary layer and the analogous effect is observed. The bi-stability can be explained with the volcano shape of the TOF function. Because the TOF

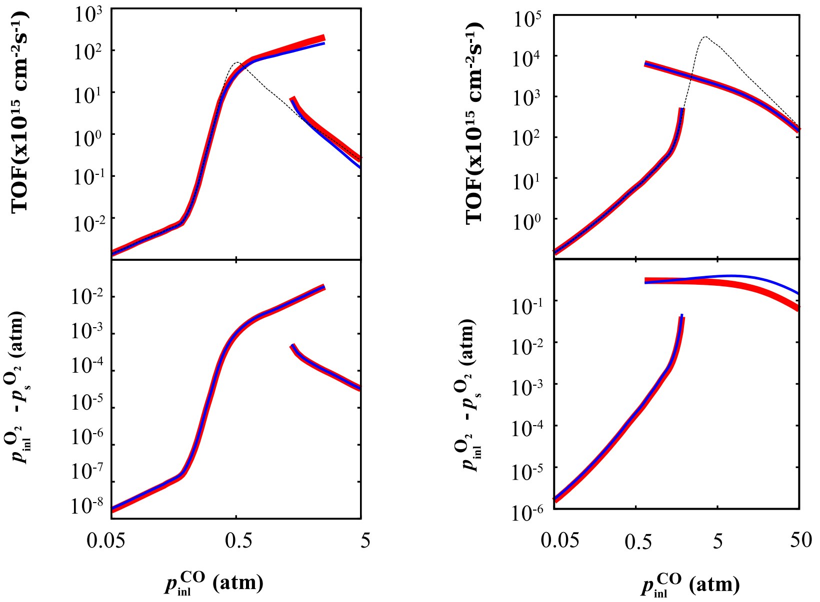

Figure 5.6: Comparison of the exact simulation results with the approximate theory for the estimated TOF and the drop of the O_2 partial pressure at the surface. Left: adiabatic case for $T_{\mathrm{inl}} = 500$K, $p_{\mathrm{inl}}^{\mathrm{O_2}} = 0.3$ atm, $u_{\mathrm{inl}} = 1$ cm/s and varying $p_{\mathrm{inl}}^{\mathrm{CO}}$ Right: Same as left, but the isothermal limit ($T_{\mathrm{inl}} = T_{\mathrm{cat}}$ =600K)

decays for higher partial pressures, we have a steady state solution with a small pressure drop, i.e. higher surface pressure, and smaller TOF, and a another one with a larger pressure drop and larger TOF. Similar arguments hold for the isolated case, when we have no pressure effects but only a temperature effect.

5.4.2 A Very Simple Model

The results in the previous sections show that it is not possible to give a value of the TOF below which mass and heat transfer effects are negligible. The problem depends too sensitively on the applied reaction and flow conditions, geometry and heat dissipation through the sample. Nevertheless an experimentalist wants to know, whether his results are masked by macroscopic transport effects or not. We therefore develop a simple approximate model, which allows to estimate the difference between applied reactions conditions at the inlet and the actual reactions conditions at the surface. Utilizing only easily accessible experimental data measured outside the reaction chamber the model leads to simple explicit formulas, which allow to estimate what is going on inside the reaction chamber. This ease of the analysis serves as another argument, why stagnation flow reactors are optimal for catalyst characterization.

We assume no diffusion and heat conduction outside the boundary layer[1], that is temperature and partial pressures do not vary between inlet and the onset of the boundary layer. Within the BL we want to assume that we have no convection, i.e. $u, V = 0$ and the heat and the diffusion fluxes are therefore constant within the BL. With equations 2.27, 2.28, 2.45 and the boundary conditions we find

$$-\kappa \frac{d}{dz} T - \sum_{\alpha} h^{\alpha} m^{\alpha} \nu^{\alpha} \mathrm{TOF} = q_{z,\mathrm{solid}} \tag{5.29}$$

$$\frac{d}{dz} p^{\alpha} = \mathrm{TOF} RT \sum_{\beta} (X^{\alpha}\nu^{\beta} - X^{\beta}\nu^{\alpha})/D^{\alpha\beta}_{\mathrm{bin}} = A^{\alpha} TOF \tag{5.30}$$

holds within the mentioned limitations for $L - L_{\mathrm{B}} < z < L$. We now want to additionally assume that κ, h^{α} and A^{α} are constant in space. With this we can write simple formulas for estimating the TOF and the importance of mass and heat transfer effects from the applied reaction conditions measured at the inlet and temperature and the heat flux at the backside of the sample. We require two boundary conditions at the backside of the sample, temperature and heat flux, different from the previous section where we needed only one. One of the boundary conditions obviously serves to replace the intrinsic TOF, which is not known in an experiment a priori. From these two boundary conditions at the backside we can determine the temperature T_{s} at the surface. The TOF can then be estimated with eq. 5.29 since with no convection and constant κ and h^{α} temperature will behave linear between the onset of the BL and the surface. The derivative in eq. 5.29 can then be replaced with the temperature difference between surface and inlet divided by the BL thickness. Under the made assumptions the partial pressures also have this linear behavior and the derivative in eq. 5.30 can eliminated in the same way as the temperature derivative. This leads to the equations

$$T_{\mathrm{s}} = \frac{d}{\kappa_{\mathrm{solid}}} q_{z,\mathrm{solid}} + T_{\mathrm{cat}} \tag{5.31}$$

$$TOF = -\frac{q_{z,\mathrm{solid}} + \kappa_{\mathrm{inl}}(T_{\mathrm{s}} - T_{\mathrm{inl}})/L_{\mathrm{B}}}{\sum_{\alpha} h^{\alpha}_{\mathrm{inl}} m^{\alpha} \nu^{\alpha}}, \tag{5.32}$$

$$p^{\alpha}_{\mathrm{inl}} - p^{\alpha}_{\mathrm{s}} = -L_{\mathrm{B}} A^{\alpha}_{\mathrm{inl}} TOF, \tag{5.33}$$

where the index $_{\mathrm{inl}}$ denotes that the indexed functions are evaluated with the inlet temperature, composition etc[2]. Note that for the first equation no approximations need to be made and the second becomes exact in the case of an isothermal flow. So it can be expected that for the well heat connected sample

---

[1] Actually this was our definition of a BL.

[2] Physically it makes more sense to evaluate the enthalpies with the surface temperature, since equation 5.29 is the balance of energy at the surface. Since the temperature dependent part is very small compared to the zero Kelvin component, this introduces only a small error, which only a negligible impact on the targeted rough estimates for the TOF

the TOF is reproduced accurately. What is left is the value for the boundary layer thickness L_{B}. Similarly to the other quantities on the right hand side we want to estimate it on the basis of measurements, which can be performed outside the reaction chamber. First we want to point out that we have pure convective transport outside the BL. No information can travel up stream by diffusion, heat conduction or viscous momentum transport. Consequently the information on the surface reactivity should only be present in the BL. Thus we can expect that the flow field outside the BL and therefore L_{B} is hardly effected by what is going on in the BL. We can hence estimate the value of L_{B} from non-reactive isothermal stagnation flows. This special case can be transformed so that the whole problem depends only on one single parameter, the Reynolds number $Re = \rho_{\mathrm{inl}} u_{\mathrm{inl}} L/\mu_{\mathrm{inl}}$ (see appendix C.1). This means that we can tabulate L_{B} as a function of Re. As mentioned the BL starts when the viscous momentum transport sets in. For non-viscous stagnation flows the scaled velocity V has a linear dependence on z[57]. Thus the deviation from the linear behavior is a good marker for the BL. In a viscous stagnation flow V is zero at the inlet and at the surface and has a maximum somewhere in between. From the previous considerations it is clear that this maximum must lie within the BL. We choose $L_{\mathrm{B}} = 2(L - z_{\mathrm{max}})$, where z_{max} is the position of the maximum of V. This ensures L_{B} approaching L for $u_{\mathrm{inl}} \to 0$, as we expect for a convection free transport problem, where the BL fills the full reactor. We have calculated L_{B} for different Reynolds numbers and found that

$$\begin{gathered}\log_{10}\frac{L_{\mathrm{B}}}{L} = -\mathrm{sig}(a_1(\log_{10}(Re) - a_2))(a_3 + a_4\log_{10}(Re)),\\ \text{with: } a_1 = 0.75,\ a_2 = 1.91,\ a_3 = 0.168,\ a_4 = 0.365,\end{gathered} \tag{5.34}$$

fits these data very well. Here $\mathrm{sig}(t) = (1 + \exp(-t))^{-1}$ is the sigmoid function, which tends to zero for $t \to -\infty$ and to one for the $t \to \infty$. Thus for large enough Reynolds numbers we have

$$\frac{L_{\mathrm{B}}}{L} = 10^{-a_3} Re^{-a_4} \tag{5.35}$$

We apply the developed method to the simulation results for the two limits of isothermal and adiabatic boundary conditions. The estimations for the TOF and the drop of the O_2 pressure are shown in figures 5.6. We find a surprisingly good agreement with the exact simulation, thereby supporting the assumptions made in the derivation of the approximate equations. The small deviations grow with increasing pressure. This can be rationalized by our choice of L_{B} being the best for low velocities and therefore low Reynolds numbers. Since the Reynolds number is proportional to the density, it increases with the total pressure and we are further away from the ideal case of no convection. The direction of the deviations is easily explained. Generally the linear approximation delivers a lower bound for the gradients at the surface, since the slope is zero at the onset of the BL and increases monotonically. To reach the same surface temperature or pressure the real gradient must therefore be larger than the linear estimate.

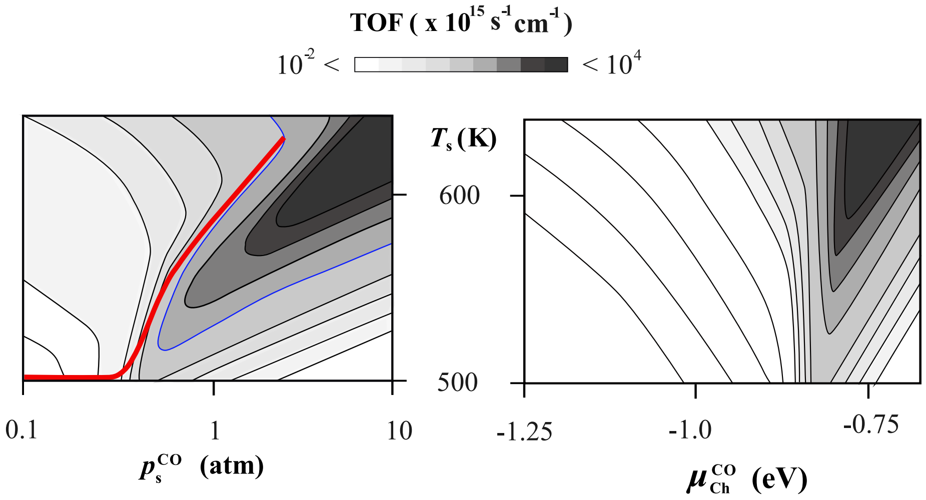

Figure 5.7: Left: intrinsic TOF (in gray scale) as a function of the surface temperature and the partial pressure of CO at the surface p_s^CO for $p_\mathrm{s}^{\mathrm{O}_2}$=0.3 atm. The red line is the high activity branch as in fig. 5.2. High steady-state activity can only be sustained until the TOF increases in all physically allowed directions. Proceeding after this point would lead to an infinite cycle of heat up and TOF increase. Right: intrinsic TOF as function of 1/T and CO chemical potential and fixed oxygen chemical potential ($\mu_\mathrm{Ch}^{\mathrm{O}_2} = \mu_\mathrm{Ch}^{\mathrm{O}_2}(p_\mathrm{s}^{\mathrm{O}_2} = 0.3\mathrm{atm}, T_\mathrm{s} = 550\mathrm{K})$). In this representation the TOF increases monotonically with the temperature and the rim of highest activity is nearly vertical.

Therefore the gas phase heat flux is underestimated in eq. 5.32 and thereby the TOF. For the same reasons the partial pressure difference is overestimated in eq. 5.33 if we know the exact TOF. This is the case for the isothermal limit, where we expect a good agreement for the TOF. Consequently the drop of the partial pressure is larger than assumed. For the limit of an isolated sample, an underestimation of the TOF is visible. This underestimation compensates with the overestimation of the partial pressure difference, so that this is accurately reproduced. Of course, this method can also be used directly with observed TOFs. Yet, these are measured at some outlet and therefore always contain edge effects. The heat flux can be measured in the middle of the backside of the sample thereby reducing the influence of the edge effects.

5.4.3 Breakdown of the Highly Active Branches

But why do the high activity branches suddenly break down? Different from the above discussion this can not be answered with one argument for both cases, the thermally well connected and the thermally isolated sample, respectively. For the isolated sample it is useful to inspect the surface temperature and the partial pressure of CO at the surface, as well as the corresponding TOF, as displayed in the left panel of figure 5.7. The axes are the CO partial pressure directly at the surface and the surface temperature. The TOF as a function of both is displayed as gray-scale contours. The oxygen partial pressure at the surface is 0.3 atm, because there is hardly any drop of partial pressures. In red we see the high activity branch. It ends at the point, when $\frac{\partial \mathrm{TOF}}{\partial T}$ changes its sign from negative to positive (which means that the blue isoline is parallel to the T_s-axis). If we increase the partial pressure of CO at the inlet, the pressure at the surface will also increase. Since the TOF increases with p_s^CO and the CO oxidation is exothermic, the surface temperature should also increase at the point of the breakdown. Nevertheless, opposite to the cases with lower surface pressures, i.e. left of the point of breakdown in the displayed figure, from this point on this increase leads to an even higher TOF and the temperature would need to increase even further, which again leads to a higher TOF and so on. As a consequence no highly active steady state can be established. The change of the slope at the point of break down can be attributed to the reaction mechanism requiring both adsorbates to be present at the surface for high activity. The most active state is therefore characterized by the coexistence of O and CO at the surface, which follows more a constant ratio of chemical potentials than the ratio of partial pressures. Thus the rim of highest activity is not a vertical line in the left panel of figure 5.7, but tilted towards higher CO pressures for higher temperatures. Plotting the TOF instead as a function CO chemical potential and temperatures the rim becomes almost vertical and the reactivity increases with temperature (right panel in fig 5.7). Also we observe that the rim broadens with temperature (entropic broadening). Translating back to partial pressures this broadening causes the observed change in the slope.

We analyze this break down in a more detailed way. Fixing the inlet boundary conditions as well as L and d the stagnation flow problem allows for a unique solution when the turnover frequency is explicitly given and not by the intrinsic catalytic function $\mathrm{TOF}_{\mathrm{intr.}}(p_\mathrm{s}^\beta, T_\mathrm{s})$. For the case at hand with varying CO partial pressure the values of all fields at the surface are functions of $p_{\mathrm{inl}}^{\mathrm{CO}}$ and the value of the TOF. We expect the temperature to monotonically increase with increasing TOF for fixed $p_{\mathrm{inl}}^{\mathrm{CO}}$ as consequence of the exothermic surface reactions. Thus there exists a one to one mapping between surface temperature and TOF, i.e. we can write

$$\mathrm{TOF} = \mathrm{TOF}_{\mathrm{Stag.}}(p_{\mathrm{inl}}^{\mathrm{CO}}, T_\mathrm{s}) \tag{5.36}$$

where the function $\mathrm{TOF}_{\mathrm{Stag.}}(p_{\mathrm{inl}}^{\mathrm{CO}}, T_\mathrm{s})$ is solely determined by the flow properties and independent of the employed catalyst. The surface temperature must be determined by the requirement that this reactor TOF must agree with the intrinsic TOF. We can write the stagnation flow problem for the TOF given by the intrinsic catalytic function

$$\begin{gathered}\mathrm{TOF}_{\mathrm{Stag.}}(p_{\mathrm{inl}}^{\mathrm{CO}}, T_\mathrm{s}) = \mathrm{TOF}_{\mathrm{intr.}}(p_\mathrm{s}^\beta(p_{\mathrm{inl}}^{\mathrm{CO}}, T_\mathrm{s}), T_\mathrm{s}) \\ \Downarrow \\ \mathrm{TOF}_{\mathrm{Stag.}}(p_{\mathrm{inl}}^{\mathrm{CO}}, T_\mathrm{s}) = \mathrm{TOF}_{\mathrm{intr.}}(p_{\mathrm{inl}}^{\mathrm{CO}}, T_\mathrm{s})\end{gathered} \tag{5.37}$$

where we have made use of $p_{\mathrm{s}}^{\beta} \approxeq p_{\mathrm{inl}}^{\beta}$ and therefore we do not need to consider oxygen partial pressure. Thus we have for varying surface temperature and CO inlet pressure

$$\frac{\partial \mathrm{TOF}_{\mathrm{Stag.}}}{\partial p_{\mathrm{inl}}^{\mathrm{CO}}} dp_{\mathrm{inl}}^{\mathrm{CO}} + \frac{\partial \mathrm{TOF}_{\mathrm{Stag.}}}{\partial T_{\mathrm{s}}} dT_{\mathrm{s}} = \frac{\partial \mathrm{TOF}_{\mathrm{intr.}}}{\partial p_{\mathrm{inl}}^{\mathrm{CO}}} dp_{\mathrm{inl}}^{\mathrm{CO}} + \frac{\partial \mathrm{TOF}_{\mathrm{intr.}}}{\partial T_{\mathrm{s}}} dT_{\mathrm{s}} \quad (5.38)$$

Now we follow the highly active branch in figure 5.7. Here $dp_{\mathrm{inl}}^{\mathrm{CO}} > 0$ holds. Recall that the intrinsic TOF must increase proceeding on this branch also after its break down. Due to exothermic reactions we have $dT_{\mathrm{s}} > 0$ and

$$\frac{\frac{\partial \mathrm{TOF}_{\mathrm{Stag.}}}{\partial p_{\mathrm{inl}}^{\mathrm{CO}}} - \frac{\partial \mathrm{TOF}_{\mathrm{intr.}}}{\partial p_{\mathrm{inl}}^{\mathrm{CO}}}}{\frac{\partial \mathrm{TOF}_{\mathrm{intr.}}}{\partial T_{\mathrm{s}}} - \frac{\partial \mathrm{TOF}_{\mathrm{Stag.}}}{\partial T_{\mathrm{s}}}} = \frac{dp_{\mathrm{inl}}^{\mathrm{CO}}}{dT_{\mathrm{s}}} > 0 \quad (5.39)$$

must hold for an active steady-state solution. For the active branch near the point of break down we have $\frac{\partial \mathrm{TOF}_{\mathrm{intr.}}}{\partial T_{\mathrm{s}}} < 0$ and so the denominator is negative since the reactor TOF increases with T_{s}. Since the whole left hand side must be positive the nominator must be negative too for a point on the active branch. Now we examine if the nominator changes sign when crossing the point of break-down. If this is not the case eqn. 5.39 gives constraints on the derivatives with respect to temperature of both reactor and intrinsic reactivity. The derivative of the reactor TOF function with respect to the partial pressure is positive (fixed T_{s}). This is because increasing the inlet pressure increases the density, which leads to a higher Reynolds number. For higher Reynolds numbers the boundary layer thickness decreases, enabling higher temperature gradients for the same temperature difference ($T_{\mathrm{s}} - T_{\mathrm{inl}}$), and therefore higher TOFs. Due to the nature of the problem we expect that the TOF increases more or less linearly with the inverse of the boundary layer thickness L_{B} (eqn. 5.32). This inverse has now a weaker than linear dependence on the Reynolds number and therefore on the density and total pressure (see eqn. 5.35).

$$L_{\mathrm{B}}^{-1} \propto Re^{a_4} \propto \rho_{\mathrm{inl}}^{a_4} \propto p_{\mathrm{inl}}^{a_4} \text{ with } a_4 = 0.365 \quad (5.40)$$

where we have neglected the (weak) dependence of the viscosity on composition for the first proportionality and assumed the same for total pressure. Since total pressure depends linear on the CO partial pressure we have a sub-linear behavior of the reactor TOF with respect to CO partial pressure. Thus, the derivative with respect to CO partial pressure of the reactor TOF decreases for higher $p_{\mathrm{inl}}^{\mathrm{CO}}$. $\frac{\partial \mathrm{TOF}_{\mathrm{Stag.}}}{\partial p_{\mathrm{inl}}^{\mathrm{CO}}}$ taken at a low CO partial pressures serves then as an upper bound for this derivative for higher partial pressures. The intrinsic TOF on the other hand increases faster than linear with respect to $p_{\mathrm{inl}}^{\mathrm{CO}}$ everywhere left of the rim. Since we have at some point on the active branch $\frac{\partial \mathrm{TOF}_{\mathrm{intr.}}}{\partial p_{\mathrm{inl}}^{\mathrm{CO}}} > \frac{\partial \mathrm{TOF}_{\mathrm{Stag.}}}{\partial p_{\mathrm{inl}}^{\mathrm{CO}}}$ it follows immediately from the afore detailed behavior that the nominator is not only negative on the active branch, but also everywhere left of the rim, especially when crossing the point of break down. Therefore we have a necessary condition

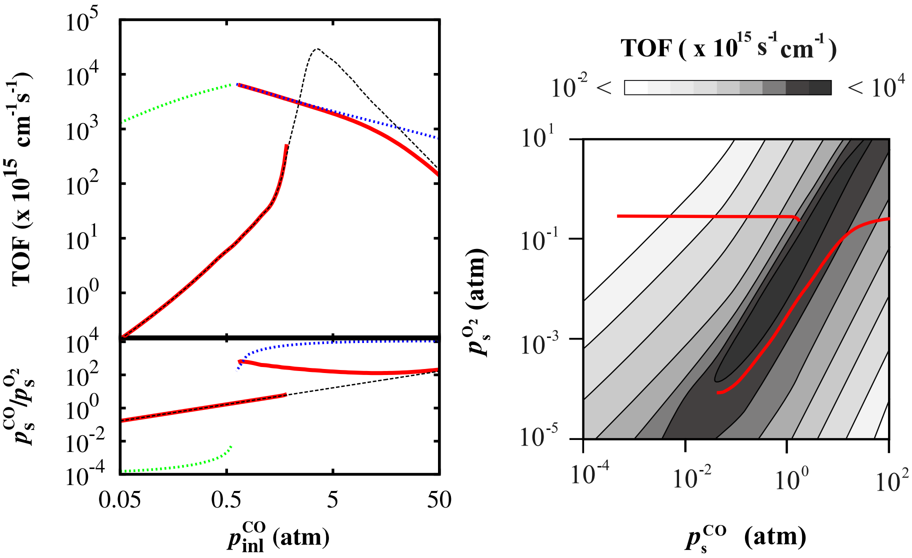

Figure 5.8: Left: Same as 5.2 right panel, now with mass transfer limits (dashed lines, green for CO transport limited and blue for O_2 transport limited). Right: TOF as function of p_s^{CO} and $p_s^{O_2}$. In red the surface partial pressures obtained in the isothermal case. The highly active branch is clearly O_2 transport limited (left). It sustains high catalytic activity to the point, where the transport of CO is the limiting factor. Proceeding on the highly active branch needs an inversion of the partial pressure ratio as can be seen in the lower panel in the left graph. However, for high O_2 and low CO partial pressures the catalyst is not active and the branch breaks down (right graph).

for a stationary solution

$$\frac{\partial \mathrm{TOF}_{\mathrm{intr.}}}{\partial T_{\mathrm{s}}} < \frac{\partial \mathrm{TOF}_{\mathrm{Stag.}}}{\partial T_{\mathrm{s}}}, \tag{5.41}$$

which is always fulfilled when the intrinsic TOF decreases with temperature. Thus the breakdown occurs not because $\frac{\partial \mathrm{TOF}_{\mathrm{intr.}}}{\partial T_{\mathrm{s}}}$ changes its sign, but rather when it becomes larger than the same derivative for the reactor TOF. This explains why we do not get a failing behavior on the active branch at lower $p_{\mathrm{inl}}^{\mathrm{CO}}$ although we have $\frac{\partial \mathrm{TOF}_{\mathrm{intr.}}}{\partial T_{\mathrm{s}}} > 0$. The corresponding derivative of the reactor TOF is there still larger.

For the isothermal case it is useful to consider mass transfer limitations, i.e. there exists an upper limit for the TOF, which is independent of the employed catalyst. This limit originates from the fact that no partial pressure can drop below zero at the surface. In practice it can be obtained by replacing the boundary conditions for the mass flux eq. 5.15 for one species by the requirement $p_{\mathrm{s}}^{\alpha} = 0$. The TOF needed for the remaining jump conditions is then obtained from the mass flux of species α at the surface. Successively performed for all species the maximum TOF is simply the lowest one of all found. The species for which $p_\mathrm{s}^\alpha = 0$ is reached first will be called minority species. The results together with the previous results for the well heat connected sample are shown in the left panel of figure 5.8. The green dotted line is the mass transfer limit, when the CO diffusion is the limiting factor. Correspondingly, the blue dotted line represents the mass transfer limit when the transport of O_2 is limiting. The highly active branch is clearly mass transfer limited. It breaks off at the transition between both regimes. This transition is at approximately stoichiometric ratio of the inlet partial pressures, due to the similar transport parameters and mass of both diatomic reactants, cf. Table 2.1. As long as the nominal inlet composition is different from stoichiometric feed, a corresponding roughly equal reduction of both reactant partial pressures close to the surface will then effectively change the $p_\mathrm{CO}^\mathrm{surf}/p_{\mathrm{O}_2}^\mathrm{surf}$ ratio. When now crossing the point with stoichiometric feed the ratio of partial pressures must invert as seen in the lower panel, where we have displayed the solution for the BC $Y^\alpha(z = L) = 10^{-4}$ of the minority species. In the right panel of figure 5.8 we display the intrinsic TOF as a function of surface partial pressures. The solutions for the surface partial pressures of the combined reaction–reactor system are displayed in red. On the active branch the surface partial pressures deviate more from their nominal inlet value the closer the inlet composition is to stoichiometric ratio. This goes hand in hand with the surface partial pressures being closer to the rim of highest activity. When the CO inlet pressure is further lowered so that there is an excess of oxygen at the inlet, a highly active solution would then require high oxygen partial pressures (compared to those of of CO). The surface partial pressures would need to cross the rim, but left from the rim the activity decreases fast and no highly active solution can be found.

5.4.4 Phenomenological Surface Modeling

In section 3.5 we have compared the findings of kMC and MFA based phenomenological kinetics. Although it fails by three orders of magnitude, especially in the oxygen covered regime, most of the qualitative features present in kMC are also present in the MFA modeling. One might thus argue that the conceptually simpler MFA modeling is sufficient for the use in flow modeling, since with the intrinsic error of the 1p-RCs in mind we can only draw qualitative conclusion also for 1p-kMC anyway. That this view does not work for the CO oxidation at RuO_2 can easily be seen in figure 5.9. The flow conditions and heat connectivity of the sample are the same as for the considered isothermal case 5.3.2 only the data points for the interpolation are exchanged from kMC based to MFA based (displayed red and blue in the left panel, respectively), all other setting are identical. At high CO partial pressures both theories give identical results. This is expected for these conditions. There we have a CO rich atmosphere at the surface, which therefore is fully CO covered, and the MFA should do a proper job. For lower CO partial pressures the MFA based modeling still agrees with the highly active branch, but it does not show the low active branch and completely misses the bi-stability. For even lower CO

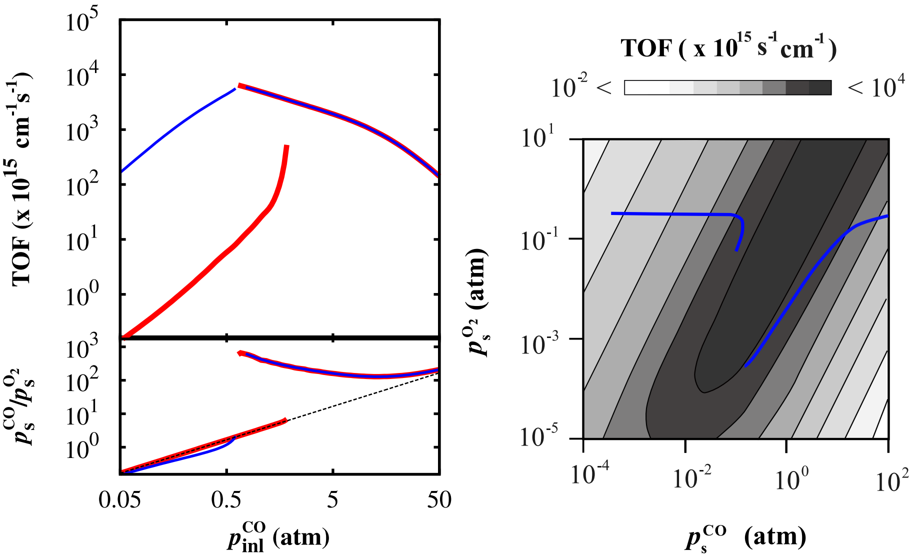

Figure 5.9: Left: PK vs. kMC based observed TOF and partial pressure ratio. PK reproduces the active branch, but not the bi-stability, and shows high activity for low $p_{\mathrm{inl}}^{\mathrm{CO}}$ different from kMC. Right: PK-TOF as function of surface partial pressures. The rim is broader than in kMC, therefore the low active branch is absent and replaced by a second highly active branch.

partial pressures, when the highly active branch in the kMC based modeling breaks down, the MFA based flow modeling continues with another highly active branch, which looks like the continuation of the high activity in the region where the oxygen transport was limiting. This continuation is spurious, as the ratio of partial pressures is discontinuous just like in kMC based modeling. Having a look at the surface partial pressure (right panel in figure 5.9) we have a very similar picture as for the kMC based case. The solution for the surface partial pressures is displayed in blue. Starting at high pressures both surface partial pressures drop below their inlet values, where the deviation increases as the CO partial pressure decreases. This behavior proceeds until the rim of highest activity is reached, and this branch stops here. This is the point where the flow regime must change from oxygen transport limited to CO transport limited. Differently, now the region of highest activity is more smeared, so that there is activity for a partial pressure ratio $p_{\mathrm{s}}^{\mathrm{CO}}/p_{\mathrm{s}}^{\mathrm{O}_2} > 2$. Although this branch - solely present in the MFA - reaches high activity, we see that it is not mass transfer limited, since the partial pressures at the surface are relatively fast approaching their nominal inlet values for decreasing $p_{\mathrm{inl}}^{\mathrm{CO}}$. On the other hand the smearing prevents now the formation of a low active branch, since it leads to a significant increase in reactivity already at low CO partial pressures, thereby transforming the low active branch in figure 5.8 into the new active branch. From the MFA data we would therefore conclude that it is worth to perform an experiment at the partial pressures of this branch: it is active but not mass transfer limited, so there is hope to extract information from such an experiment. On contrary, looking at the kMC data we would advice an experimentalist to perform the experiment at different conditions. The kMC based data namely show only two extremes: either the catalyst is inactive or we are faced with mass transfer limitations. Extracting information about the chemistry is very difficult in both cases. On the one hand low reaction rates are difficult to measure and will carry large uncertainties. When the reactivity is mass transfer limited at least one partial pressure at the surface is not accessible, because little changes in the TOF cause large relative changes for a partial pressure at the surface, which is already nearly zero.

In conclusion, using 1p-RCs in a phenomenological framework misses some qualitative important features and - even more severe - leads to opposite conclusions on how to proceed with experiments. If one wants to use 1p-RCs in conjunction with a MFA, the MFA needs to be tested to give a good **quantitative** agreement with kMC in order to avoid a **qualitative** failure at the reactor level.

5.5 Summary

The afore developed methodology for coupling first principles statistical mechanics to reactive flow simulations was applied to stationary stagnation flows as suitable, albeit idealized model in order to discuss qualitative features arising in *in situ* experiments with single crystals due to macroscopic heat and mass transfer. The observed activity in such reactors might deviate tremendously from the targeted intrinsic catalytic function. Not taking macroscopic transport phenomena into account, the catalyst and its surface chemistry might look more complex than it actually is. In the here discussed example the combined gas flow/surface chemistry system shows a bistable behavior, while for the intrinsic activity this effect is absent. The question arises whether the two branches are stable and what happens in real experiments when the combined flow–surface system needs to change from one branch to the other. Only corresponding time-resolved simulations can answer these questions and give access to the wealth of phenomena that are now only suggested by the observed bi-stability. Notably this is the possibility of oscillations between the two modes. In contrast to e.g. purely surface reaction–surface diffusion driven oscillations on single-crystals in UHV [53] the mechanistic details behind corresponding reactor–reaction oscillations in the ambient pressure regime are only poorly understood [107].

Our findings can be easily explained in terms of a boundary layer, where all non-convective transport takes place. Making use of the boundary layer concept we have developed a very approximate theory, which needs only the temperature and the heat flux at the backside of the sample as an input. This method agrees surprisingly well with the correct simulation results. The developed explicit simple formulas might serve for experimentalists as a measure for the order of magnitude of mass and heat transfer effects in their experiment.

The real thermal coupling of the sample is investigated at two extreme cases: a thermally isolated sample where all the reaction heat must be transported away by the gas phase, and a thermally well connected sample ensuring nearly isothermal operating conditions. In the former, adiabatic limit the deviation from the ideal behavior was driven by a significant surface heating. For the isothermal limit this was due to mass transfer effects, that led to the build-up of a significant concentration of products in the boundary layer above the active surface. With the single-crystals in real experimental setups being neither perfectly heat-coupled nor isolated, these two effects discussed here separately will obviously be intricately intermingled and need to be disentangled from the desired intrinsic activity by dedicated experiments. One of such setups are the here discussed stagnation flows. Due to their quasi one-dimensional nature, their analysis is extremely simple, even allowing for an inversion of experimental data to obtain the intrinsic catalytic function. Also because of the limitation of the employed 1p-kMC $RuO_2(110)$ model with respect to a reduction of the oxide catalyst we have refrained from comparing our simulations to already published experimental data. Nevertheless, we note that the gas-phase conditions and TOFs discussed here are of the order of magnitude presented in a manifold of *in situ* studies of CO oxidation at late transition metal catalysts. In this respect it is important to recognize that the CO oxidation reaction – that has been a fruit-fly reaction in UHV surface science due to its alleged "simplicity" and model character – requires particular attention. The high turnovers that can be reached precisely because of this "simplicity" make this reaction much more prone to transport effects than other more complex, selective ones.

Chapter 6

Conclusion

Future materials' design will eventually rely on a microscopic understanding on the molecular or even electronic level. An important field, where such understanding is commonly regarded as invaluable, is heterogeneous catalysis. In order to bridge the gap between this understanding of the elementary processes, e.g bond breaking and bond making, and the targeted macroscopic response of materials multi-scale methodologies need to be developed. Such an approach has been introduced in this work allowing for an integrated modeling from the smallest, i.e. electronic, to the largest, i.e. continuum, scales. Thereby it enables the simulation of a macroscopic chemical reactor on a first principles basis. Existing modeling approaches in contrast have either started on[118, 62] or left out[54] a level between these two extreme scales, thereby introducing a rather uncontrollable error. While we could build on the existing methodology of 1p statistical mechanics bridging between the electronic and mesoscopic level[94], the focus of this study was to make the last step, i.e. bridging between the mesoscopic and the continuum scale. The approach was applied to the CO oxidation at $RuO_2(110)$ as a representative example for currently investigated model catalysts.

After introducing the established continuum mechanical models for gas flow, heat transport in the solid and the interface of both phases the basis for a stochastic modeling of the surface kinetics was explained. Making use of the established first principles based micro-kinetic model for the afore mentioned reaction system[97] the performance of two extreme methods used for extracting information from the high-dimensional mesoscopic model was investigated. The approximate classical phenomenological kinetics was compared to the accurate but also computationally expensive kinetic Monte Carlo simulations. Large differences between both approaches were observed for the investigated microkinetic model[112] with deviations of orders of magnitude for the turnover frequency for a surface fully covered with oxygen. Oppositely for a CO covered surface the agreement for the TOF was almost exact. The success and failures of the classical approach were analyzed with the help of the Degree of Rate Control as a measure for rate-limiting steps. An improper account for the occurrence of vacancy pairs was identified as the reason for the mismatch at high oxygen partial pressures. The obtained insight was used to develop a modified version of the phenomenological kinetics able to describe the response of a oxygen covered surface. In the analysis of both models it turned out that such a model can give quantitative agreement for the macroscopic accessible reaction rates, although it might not reflect the real mesoscopic behavior, e.g. which reaction channels are dominant. Even more severe the model can be tested at some reaction conditions to reproduce the mesoscopic behavior, and while still agreeing with the accurate kMC results for the macroscopic reaction rates, it already misses the details of exactly that mesoscopic behavior at slightly different reaction conditions. Concluding it must be said that phenomenological models are a good tool for effectively representing macroscopic reactivity data, especially when they are fitted to the data they shall reproduce, but the information about the mesoscopic surface chemistry needs to be treated with some skepticism.

In order to maintain the accuracy of the 1p-kMC simulations an alternative efficient approach was therefore developed for coupling first principles based detailed reaction chemistry with continuum level simulations. The developed methodology based on an interpolation of the reactivity data allows for macroscopic heat and mass transport simulations with computational costs comparable to phenomenological models. In its construction the methodology can easily be applied with any kind of flow solver. For the considered CO oxidation example the interpolation could have been based on gridded data. Yet, interpolation on a grid becomes prohibitive for complex reaction mechanism with more than two gas phase species that can adsorb. The here employed modified Sheppard interpolation can instead deal with more or less arbitrarily distributed data thereby allowing to interpolate data in higher dimensions. Nevertheless there exist multiple ways of scattered data interpolation, e.g. the very popular radial basis function methods[105], and since every method has its strengths and weaknesses future work needs to investigate the performance of the different available methods. Regardless which methods turns out to be the best for a certain problem choosing the data points for a high-dimensional interpolation is a crucial point, especially when the generation of the necessary data is costly. Thus methods are needed capable to construct optimal point sets, so that the interpolation error is minimal for a fixed number of points. The problem of good quality data sets exists in many fields of physics and engineering e.g. for the representation of potential energy surfaces[6], and such a method would have a high impact not only in the here investigated field.

Even though developed to be used also for complex geometries, the approach was applied to the CO oxidation at $RuO_2(110)$ in a stationary stagnation flow reactor as suitable example to discuss transport effects in modern *in situ* experiments. The intrinsic catalytic function was found to be masked by macroscopic transport effects with the observed activity deviating by up to three orders of magnitude from the intrinsic one. The outcome of an experiment depends thus sensitively on the employed reactor geometry (mimicked in this study by varying the inlet-surface distance) and the applied throughput rate (i.e. the streaming velocity at the inlet). For the thin, well heat conducting single-crystal the degree of heat dissipation possible at the back of the sample (e.g. through radiative loss or contact to the sample holder) is a further crucial factor. Not aiming, nor being able to address specific experimental realizations this was considered through two opposite extremes: The isothermal limit mimicking a highly efficient heat coupling of the crystal to the system, and the adiabatic limit to represent a well insulated sample. In real experimental setups none of both cases will be achieved and the effects discussed here separately will probably occur at the same time. If such peculiarities are not appropriately accounted for, qualitatively wrong conclusions can be made, preventing a qualified discussion of the effect of the pressure gap. This becomes most perspicuous considering the partial pressure ranges where the coupled system of flow and surface shows bi-stability, while the surface chemistry alone does not show this effect. This bi-stability elucidates, why mass transfer effects need to be considered not only for theory/experiment comparisons but also in the comparison of different experiments even when drawing only qualitative conclusions. Here we can have a difference of up to three orders of magnitude between the possible outcomes for one and the same experimental setup. Thus one could conclude that the catalyst is very active as well as that the catalyst is hardly active, depending in which stationary solution the combined reactor surface system runs. When comparing experimental results from different reaction chambers this effect can be even enhanced, disqualifying any discussion even on the very qualitative level. Thus, eliminating mass and heat transfer effects from both experimental results and thereby arriving at the intrinsic catalytic function is a crucial task. Reaction chambers operating in the stagnation flow regime are especially suitable for this purpose, due to their quasi-one-dimensional nature. For the CO oxidation in these reactors the dependence on the applied inlet velocity and the size of the reaction chamber can conveniently be explained in terms of the formation of a boundary layer above the catalyst's surface. The origin of the deviation from the intrinsic behavior is different in both examined cases of heat coupling at the sample's backside. In the adiabatic limit it is a pure temperature effect, while in the isothermal limit this is solely driven by mass transfer effects. Consequently, the reasons for the breakdown of the highly active branches observed in both cases have a different origin. For the isolated sample this breakdown is related to a qualitative change in the intrinsic catalytic function. In the other case the breakdown can nearly exclusively be attributed to a property of the reaction chamber, since the mass transfer limit shown in fig. 5.8 is completely independent of the employed catalyst. In this study we have restricted our attention to stationary stagnation flows. However the observed bi-stability clearly suggests that transient behavior is important, and the system might oscillate between both stationary solutions, possible even in-homogeneously showing pattern formation at the surface in this case mediated by gas phase transport. Clearly next steps will be the investigation of the time dependent stagnation flow problem[7] and the extension to two and three dimensional problems by coupling the interpolation to existing CFD software, e.g. [12, 8]. Even without oscillating behavior and pattern formation such CFD simulations might be necessary for analyzing *in situ* experiments. Many experimental techniques like *in situ* Scanning Tunneling Microscopes[89] need to put a tip near to the surface, thereby making the depicted stagnation flow geometry impossible. In order to establish a relation between reactivity, reaction conditions and micro-structure, partial pressures and temperature near the tip are required and there is no way around a full CFD simulation.

Acknowledgements

This thesis would not be possible without the support of many different people. Starting in a more or less chronological order these are my parents, Elke and Sepp, my grandparents, Bruno and Ursula, my aunts, Christa and Bärbel, and my uncles, Helmut and Winfried. The time and efforts, they invested in me and my education, enabled me to study and to conduct the research for this thesis in the first place. I also want to thank my girlfriend Joanna for her patience with me, when I was having no time, and her support, when I was desperate. Up to now I have only mentioned those, who are not directly related to the Fritz Haber Institute. Of course I am also indebted to a lot the people working there. I therefore want to acknowledge

- My supervisor Prof. Karsten Reuter, for his trust in my skills, for keeping me on track, when I wanted too much in too short time, for being the boss and teacher, I needed.
- My former office mate Dr. Hakim Meskine, for fruitful discussions and collaboration, very much of chapter 3 is based upon our common endeavors.
- Prof. Matthias Scheffler and Prof. Horia Metiu (Santa Barbara), for fruitful discussions and collaboration.
- The non-scientific members of the theory department, for keeping the show running.
- My colleagues at the theory department at the FHI, for fruitful discussions and brightening up a hard working day.

Of course, scientists can not live from air and motivation. Therefore I want to acknowledge the Multiscale Modeling of Materials initiative of the Max Planck Society and the UniCat Cluster of Excellence by the German Research Council for funding.

Publications

The work presented in this thesis has been or will be published in the following articles

1. H. Meskine, S. Matera, M. Scheffler, K. Reuter, and H. Metiu, *Examination of the concept of degree of rate control by first-principles kinetic Monte Carlo simulations.* Surf. Sci. **603**, 1724-1730 (2009)
2. S. Matera and K. Reuter, *First-principles approach to heat and mass transfer effects in model catalyst studies.* Catal. Lett. **133**, 156-159 (2009).
3. S. Matera and K. Reuter, *Transport limitations and bistability for in situ CO oxidation at RuO2(110): First-principles based multiscale modeling.* Phys. Rev. B **82**, 085446 (2010)
4. S. Matera, H. Meskine, M. Scheffler, and K. Reuter *Adlayer inhomogeneity without lateral interactions: Rationalizing correlation effects in CO oxidation at RuO_2(110) with first-principles kinetic Monte Carlo* (in preparation)

Appendix A

Notation

In this appendix the notation, which is used in the text is going to be explained.

A.1 Scalars, Vectors, Tensors

In this section the notation of the mathematical objects used for the continuum mechanical modeling is explained. These are tensors of different order. An introduction to tensor calculus using a similar notation can be found in books by Lebedev and Cloud [64] and by Schade [106]. For Latin indices Einstein's sum convention is used (it is summed over twice appearing indices or superscripts). This use restricts to this appendix, in the text we will use exclusively to the symbolic representation. A tensor is marked with several underlines. If a tensor has the order m, it is m times underlined. Therefore a scalar (0. order tensor) has no underline, a vector (1. order tensor) has one underline and all other tensors have at least two underlines. Examples

$$\begin{aligned} &\text{a scalar: } s \\ &\text{a vector: } \underline{v} \\ &\text{a second order tensor: } \underline{\underline{T}} \end{aligned} \tag{A.1}$$

A dot '$\cdot$' denotes a scalar product. Two dots '$\cdot\cdot$' is the double scalar product (symmetric). No symbol between two tensors of different or same order denotes the dyadic (tensor) product. Examples ($\{\underline{e}_i\}$ is a Cartesian basis)

a scalar product between a vector $\underline{v}$ and a tensor $\underline{\underline{T}}$:

$$\underline{\underline{T}} \cdot \underline{v} = T^{ij}\underline{e}_i\underline{e}_j \cdot v^k\underline{e}_k = T^{ij}v^k\underline{e}_i(\underline{e}_j \cdot \underline{e}_k) = T^{ij}v^k\delta_{jk}\underline{e}_i = T^{ij}v^j\underline{e}_i. \tag{A.2}$$

a double scalar product between two tensors $\underline{\underline{T}}$ and $\underline{\underline{S}}$:

$$\underline{\underline{T}} \cdot\cdot \underline{\underline{S}} = T^{ij}\underline{e}_i\underline{e}_j \cdot\cdot S^{kl}\underline{e}_k\underline{e}_l = T^{ij}S^{kl}(\underline{e}_j \cdot \underline{e}_k)(\underline{e}_i \cdot \underline{e}_l) = T^{ij}S^{kl}\delta_{jk}\delta_{il} = T^{ij}S^{ji}. \tag{A.3}$$

a dyadic product between two vectors $\underline{v}$ and $\underline{w}$:

$$\underline{v}\underline{w} = v^i \underline{e}_i w^j \underline{e}_j = v^i w^j \underline{e}_i \underline{e}_j. \tag{A.4}$$

The second order unit tensor $\underline{\underline{1}}$ is defined by

$$\underline{\underline{1}} \cdot \underline{v} = \underline{v} \cdot \underline{\underline{1}} = \underline{v}, \quad \forall \underline{v}. \tag{A.5}$$

In the text the differential (nabla) operator $\nabla(\cdot)$ is often used. This can be used to define gradient and divergence. Definition ($\{\underline{e}_i\}$ is a Cartesian basis and q_i are the corresponding coordinates):

The Nabla operator:

$$\nabla(\cdot) = \underline{e}_i \frac{\partial}{\partial q_i}(\cdot) \tag{A.6}$$

Gradient of a vector field:

$$\nabla \underline{v} = \underline{e}_i \underline{e}_j \frac{\partial}{\partial q_i} v_j \tag{A.7}$$

Divergence of a tensor field:

$$\nabla \cdot \underline{\underline{T}} = \underline{e}_i \cdot \frac{\partial}{\partial q_i}(T_{jk} \underline{e}_j \underline{e}_k) = \underline{e}_k \frac{\partial}{\partial q_j} T_{jk} \tag{A.8}$$

A.2 Matrices

All matrices of arbitrary dimensions (this includes row- and line-matrices) are bold printed

$$\mathbf{M}. \tag{A.9}$$

The normal matrix multiplication has no operation symbol. Hence we have for $n \times m$ matrix $\mathbf{A}$ $m \times p$ matrix $\mathbf{B}$

$$\mathbf{AB} = \mathbf{C} \quad , \tag{A.10}$$

where $\mathbf{C}$ is a $n \times p$ matrix. An element of a matrix $\mathbf{C}$ with the column index i and the row index j is referenced by

$$C_{ij}. \tag{A.11}$$

When there is set of matrices $\{\mathbf{C}_l\}$ we will denote a matrix element by

$$(\mathbf{C}_l)_{ij} \tag{A.12}$$

so that the index l denoting the matrix is not confounded with the column and row indices i, j, resp.. The transposed of a matrix will be denoted with the usual ^{T} as superscript.

Appendix B

Some Theory on Reaction Rates

We consider the master equation for surface kinetics 3.3. We use a symbolic notation

$$\partial_t \mathbf{p} = \mathbf{\Gamma} \mathbf{p}, \tag{B.1}$$

where entries in $\mathbf{p}$ are the probabilities for finding a certain adsorbate configuration. The linear operator $\mathbf{\Gamma}$ depends linearly on the rate constants w_i (RC) (compare section 3.1). Now we want to find out how the stationary probability $\mathbf{p}_{\text{stat}}$ changes when the vector of RCs $\mathbf{w}$ is multiplied by an arbitrary number $\lambda \neq 0$. We have

$$0 = \mathbf{\Gamma}(\mathbf{w})\mathbf{p}_{\text{stat}}, \tag{B.2}$$

$$0 = \mathbf{\Gamma}(\lambda \mathbf{w})\mathbf{p}_{\text{stat}}(\lambda) = \lambda \mathbf{\Gamma}(\mathbf{w})\mathbf{p}_{\text{stat}}(\lambda). \tag{B.3}$$

We can see, that $\mathbf{p}_{\text{stat}}(\lambda)$ does not depend on λ. Thus $\mathbf{p}_{\text{stat}}$ is a homogeneous function of degree zero of the rate constants[13]. The stationary reaction rates s_K can be expressed as

$$s_K = \mathbf{K}^T \mathbf{p}_{\text{stat}} \tag{B.4}$$

where $\mathbf{K}$ depends linearly on $\mathbf{w}$ (compare equation 3.15). It thus follows immediately that the reaction rate is homogeneous of grade one and

$$s_K = \sum_i \frac{\partial s_K}{\partial w_i} w_i \tag{B.5}$$

holds as long the turn-over frequency is differentiable. Thus

$$\sum_i X^i_{\text{rc},K} = 1 \tag{B.6}$$

holds for the Degree of Rate Control (DRC) defined by eq. 3.16.

A widely used concept in empirical chemical kinetics is that of reaction orders. A stationary reaction rate is expressed as

$$s_K = \tilde{k}_K \prod_{\alpha}^{N_{\mathrm{spec}}} (p_{\mathrm{s}}^{\alpha})^{r_K^{\alpha}} \tag{B.7}$$

for a range of reaction conditions, where r_K^{α} is the reaction order of s_K with respect to p_{s}^{α}. The empirical rate constant $\tilde{k}_K$ is supposed to be independent of the partial pressures. Using the chain rule and eq. 3.18 it follows

$$r_K^{\alpha} = \left(\frac{\partial \ln s_K}{\partial \ln p_{\mathrm{s}}^{\alpha}} \right)_{T, p^{\beta} (\beta \neq \alpha)} = \sum_K X_{\mathrm{rc},K}^{i,\alpha} \tag{B.8}$$

where the sum runs over all elementary reactions which are an adsorption of species α and $X_{\mathrm{rc},K}^{i,\alpha}$ are the corresponding DRCs. A constant sensitivity pattern leads obviously automatically to constant reaction orders.

Appendix C

Tests for Stagnation Flow solver

C.1 Isothermal non-reactive stagnation flow

In the case of an isothermal flow with no chemical reactions (i.e. there will be no diffusion) the low Mach number equations reduce to the incompressible Navier-Stokes equations. Of course this translates for the stagnation flow equations, since they are just special cases of the LMA. The stagnation flow problem arising

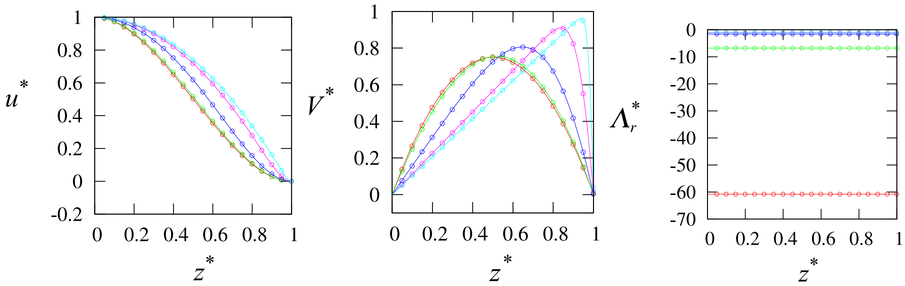

Figure C.1: Left: Scaled axial velocity u^* as a function of the scaled spatial coordinate z^*. Obtained by solving the full stagnation flow problem (chap. 5, circles) and the incompressible stagnation flow equations (eq. C.1,lines). The colors correspond to different Reynolds numbers: $Re = 0.1$ (red), $Re = 1$ (green), $Re = 10$ (blue), $Re = 100$ (purple), $Re = 1000$ (cyan). Middle: same as left but the reduced radial Velocity V^* is displayed. Right: same as left but the scaled pressure curvature Λ_r^* is displayed.

from the incompressible Navier-Stokes equations can be reduced

$$\begin{aligned}
&\frac{d}{dz^*}u^* = -2V^*,\\
&\frac{d}{dz^*}V^* = A^*,\\
&\frac{d}{dz^*}A^* = \frac{1}{Re}(u^*A^* + (V^*)^2 + \Lambda_r^*),\\
&\frac{d}{dz^*}\Lambda_r^* = 0,\\
&\text{with the boundary conditions}\\
&u^*(0) = 1,\ V^*(0) = 0,\ u^*(1) = 0,\ V^*(1) = 0,
\end{aligned} \tag{C.1}$$

with $z^* = z/L$, $u^* = u/u_{\mathrm{inl}}$, $V* = VL/u_{\mathrm{inl}}$, $\Lambda_r^* = \Lambda_r L^2/u_i n l^2/\rho$. Obviously the Reynolds number $Re = \rho u_{\mathrm{inl}} L/\mu$ is the only free parameter and the diversity of flow problems (i.e. different inlet velocities, viscosities, densities) can be represented in terms of Re. Thus a certain flow configuration can be tackled by calculating Re and solving eqn. C.1. In the end the desired fields are obtained by inverting the the definitions of u^*, V^* etc.. The boundary value problem C.1 is solved with the **COLNEW** software[3]. Variables and equation were not scaled in the actual calculation and all numerical settings were identical to those employed in the solution of the general stagnation flow equations (see 5.2) except that we do not supply an initial guess and use the default option instead. In figure C.1 results obtained by solving C.1 are compared to the solutions obtained by solving the full stagnation flow equations (see chapter 5) with $TOF = 0$. For the later case the inlet boundary conditions were fixed $p_{\mathrm{inl}}^{\mathrm{CO}}$ =2atm, $p_{\mathrm{inl}}^{\mathrm{O}_2}$ =1atm, $p_{\mathrm{inl}}^{\mathrm{CO}_2} = 10^{-5}$atm, and T_{inl} =600K and varying $u_{\mathrm{inl}} \in 1.57[10^{-4}, 10^{-3}, 10^{-2}, 10^{-1}, 10^{0}, 10^{1}]$. In conjunction with $L = 1cm$ this results in flows with $Re \in [0.1, 1, 10, 100, 1000]$. Both solutions - incompressible and full stagnation flows - agree within the numerical accuracy as it should be case. Since both equation were independently implemented this serves as a test for the proper implementation and numerical solution of the general stagnation flow equations 5.1-2.32.

C.2 Non-Convective Stagnation Flow

In the limit $u_{\mathrm{inl}} \to 0$ we expect that the velocity vanishes everywhere. The species and the energy balance reduce to the mere requirement of constant heat and mass fluxes

$$\begin{aligned}
j_z^{\alpha}(z) &= -m_\alpha \nu_\alpha \mathrm{TOF}(p^\beta(z = L), T(z = L)),\\
q_z(z) &= \frac{\kappa_{\mathrm{solid}}}{d}\left(T(z = L) - T_{\mathrm{cat}}\right)
\end{aligned} \tag{C.2}$$

where we have used the boundary conditions 5.15 and 5.18. Note that in the above equation only the knowledge of the TOF is required to obtain all three

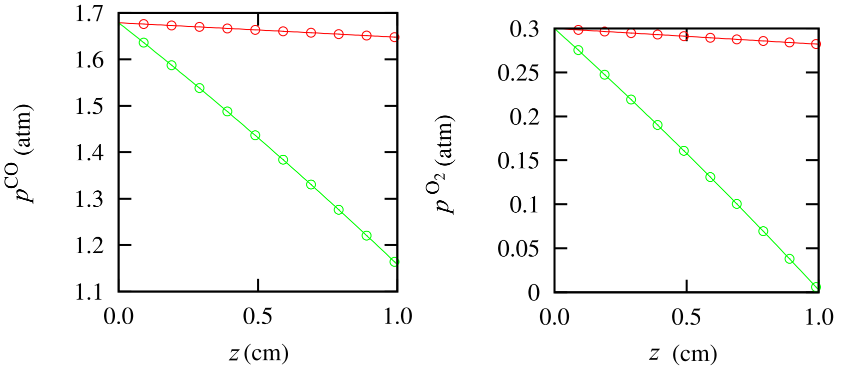

Figure C.2: Isothermal boundary conditions and no convection: displayed are both solutions of the transport problem obtained by the reduced theory (lines) and the full stagnation flow problem (chap. 5, circles) Left: CO partial pressure. Right: O_2 partial pressure.

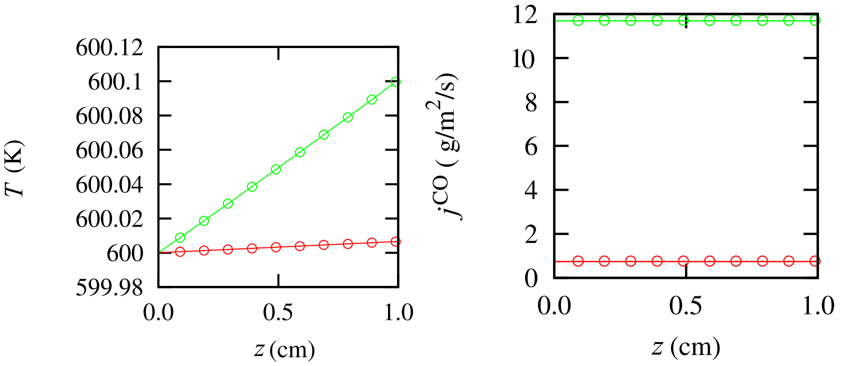

Figure C.3: Same as C.2 but temperature is displayed left and the diffusive mass flux of CO is displayed in the right panel.

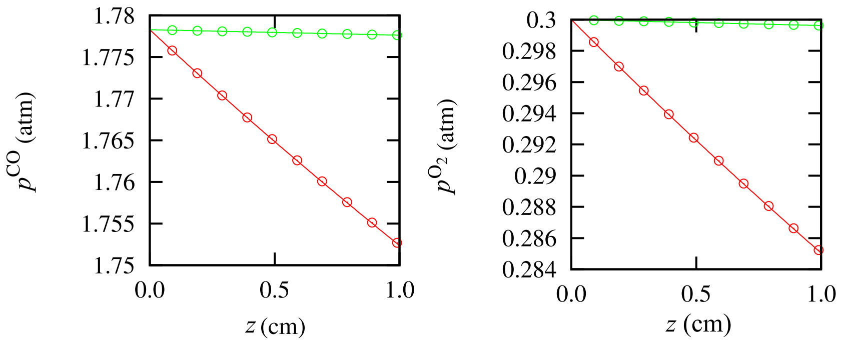

Figure C.4: Adiabatic boundary conditions: displayed are both solutions of the transport problem obtained by the reduced theory (lines) and the full stagnation flow problem (chap. 5, circles) Left: CO partial pressure. Right: O_2 partial pressure.

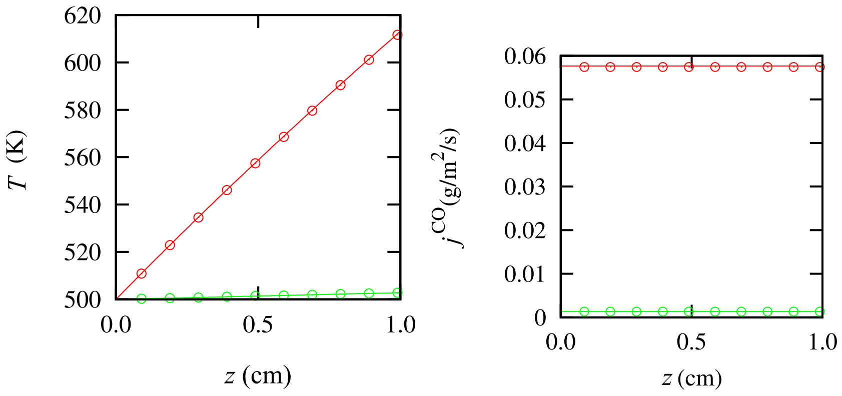

Figure C.5: Same as C.4but temperature is displayed left and the diffusive mass flux of CO is displayed in the right panel.

mass fluxes. Together with the Stephan-Maxwell equations 2.45 and the relation for the heat flux 2.28 the the stagnation flow equations reduces to the boundary value problem

$$\frac{d}{dz}s_{\mathrm{CO}_2} = 0, \tag{C.3}$$

$$\frac{d}{dz}q_z = 0, \tag{C.4}$$

$$\frac{d}{dz}T = \frac{1}{\kappa}(-q + \sum_{\alpha} h^{\alpha} m_{\alpha} \nu_{\alpha} r_{\mathrm{CO}_2}, \tag{C.5}$$

$$\frac{d}{dz}p^{\alpha} = s_{\mathrm{CO}_2} RT \sum_{\beta} (X^{\alpha}\nu^{\beta} - X^{\beta}\nu^{\alpha})/D^{\alpha\beta}_{\mathrm{bin}}, \tag{C.6}$$

$$\text{with the BC} \tag{C.7}$$

$$p^{\alpha}(z=0) = p^{\alpha}_{rminl},\ T(z=0) = T_{\mathrm{inl}}, \tag{C.8}$$

$$s_{\mathrm{CO}_2}(z=L) = \mathrm{TOF}(p^{\beta}(z=L), T(z=L)), \tag{C.9}$$

$$q_z(z=L) = \frac{\kappa_{\mathrm{solid}}}{d}\left(T(z=L) - T_{\mathrm{cat}}\right), \tag{C.10}$$

which is numerically solved with the solver **COLNEW**[3]. The partial pressures are scaled with their values at the inlet. Temperature is represented as for the stagnation flows. The reaction rate s_{CO_2} is expressed in multiples of $s_{\mathrm{scal}} = -\frac{D^{\mathrm{eff,inl}} Y^{\mathrm{inl}}_{\alpha}}{L\nu^{rmCO} m^{rmCO}}$ and q in multiples of $\kappa_{\mathrm{inl}} T_{\mathrm{scale}}/L - \sum_{\alpha} h^{\alpha} s_{\mathrm{scal}} m^{\alpha} nu^{\alpha}$. All settings have been chosen identical to those used to solve the stagnation flow equations.

The tests are performed for $L = 1$cm, $p^{\mathrm{O}_2}_{\mathrm{inl}} = 0.3$atm, $p^{\mathrm{CO}_2}_{\mathrm{inl}} = 10^{-5}$atm. As in chapter 5 we consider the isothermal case $T_{\mathrm{inl}} = T_{\mathrm{cat}} = 600$K with $D =$ 1mm, we set the CO partial pressure to $p^{\mathrm{CO}}_{\mathrm{inl}}$ =1.67 atm. Here the coupled transport-surface reaction problem has two solutions, which are both displayed in the figures C.2 and C.3. We mimic the isolated case ($T_{\mathrm{inl}} = 500$K, $q_{\mathrm{cat}} = 0$) by setting $T_{\mathrm{cat}} = 500$K and $D = 100$m in the above equations. We choose $p^{\mathrm{CO}}_{\mathrm{inl}}$ =1.67 atm. The results are shown in the figures C.4 and C.5. In all cases the deviation between both employed theories (full stagnation flow and reduced theory) is within the numerical accuracy.

Bibliography

[1] P. Alfeld. Scattered data interpolation in three or more variables. In Tom Lyche and Larry L. Schumaker, editors, *Mathematical Methods in Computer Aided Geometric Design*, pages 1–34. Academic Press, 1989.

[2] T. Arima. Numerical methods for chemically reacting fluid flow computation under low Mach number approximation. *Tokyo Journal of Mathematics*, 29(1):167–198, 2006.

[3] U. Ascher, J. Christiansen, and R.D. Russell. Collocation softare for boundary value ode's. *ACM Transactions Math Software*, 7:209, 1981.

[4] U. Ascher and R. Spiteri. Collocation software for boundary value differential-algebraic equations. *SIAM Journal on Scientific Computing*, 15:938, 1994.

[5] P. W. Atkins. *Physical Chemistry.* Oxford University Press, 6th edition, 2001.

[6] J. Behler, S. Lorenz, and K. Reuter. Representing molecule-surface interactions with symmetry-adapted neural networks. *Journal of Chemical Physics*, 127:014705, 2007.

[7] F. Behrendt. Experimentelle und numerische Beschreibung katalytischer Zünd- und Verbrennungsprozesse. Univerität Heidelberg.

[8] J. B. Bell. AMR for low Mach number reacting flow. *Adaptive Mesh Refinement-Theory and Applications*, pages 203–221, 2005.

[9] R.B. Bird, W.E. Stewart, and E.N. Lightfood. *Transport Phenomena.* Wiley, 1st edition, 1960.

[10] M. Born and J. R. Oppenheimer. Zur Quantentheorie der Molekeln. *Ann. Phys.*, 84:457, 1927.

[11] A. B. Bortz, M. H. Kalos, and J. L. Lebowitz. A new algorithm for Monte Carlo simulation of ising spin systems. *Journal of Computational Physics*, 17(1):10–18, 1975.

[12] M. Braack and T. Richter. Stabilized finite elements for 3D reactive flows. *International journal for numerical methods in fluids*, 51(9-10):981–999, 2005.

[13] I. N. Bronstejn and K. A. Semendjaev. *Taschenbuch der Mathematik.* Teubner, 1979.

[14] C. T. Campbell. Micro- and macro-kinetics: their relationship in heterogeneous catalysis. *Topics Catalysis*, 1:353, 1994.

[15] S Chapman and T.G. Cowling. *The mathematical theory of non-uniform gases.* Cambridge University Press, 3rd edition, 1970.

[16] A. Chatterjee and D. G. Vlachos. An overview of spatial microscopic and accelerated kinetic Monte Carlo methods. *Journal Computer-Aided Material Design*, 14:253308, 2007.

[17] I. Chorkendorff and H. Niemantsverdriet. *Concepts of Modern Catalysis and Kinetics.* Wiley-VCH, 2003.

[18] L.D. Cloutman. A selected library of transport coefficients for combustion and plasma physics applications. Technical Report UCRL-ID-139893, Lawrence Livermore National Laboratory, 2000.

[19] M. E. Coltrin, R. J. Kee, and G. H. Evans. A mathematical model of the fluid mechanics and gas-phase chemistry in a rotating disk chemical vapor deposition reactor. *Journal of the Electrochemical Society*, 136(3):819–829, 1989.

[20] M. E. Coltrin, R. J. Kee, and F. M. Rupley. SURFACE CHEMKIN (version 4.0):a fortran package for analyzing heterogeneous chemical kinetics at a solid-surface gas-phase interface. Technical Report SAND90-8003B, Sandia National Laboratories, 1990.

[21] C.F. Curtiss and J.O. Hirschfelder. Transport properties of multicomponent gas mixtures. *Journal of Chemical Physics*, 17:550, 1949.

[22] C. "de Boor". *A practical guide to splines.* Springer, 1978.

[23] O. Deutschmann. Computational fluid dynamics simulation of catalytic reactors. In G. Ertl, H. Knözinger, F. Schüth, and J Weinkamp, editors, *Handbook of Heterogeneous Catalysis.* Wiley-VCH, Weinheim, 2 edition, 2008.

[24] O. Deutschmann, R. Schmidt, F. Behrendt, and J. Warnatz. Numerical modeling of catalytic ignition. In AR Burgess and FL Dryer, editors, *Twenty-sixth Symposium (International) on Combustion, Vol. 1 & 2*, pages 1747–1754, 1996.

[25] O. et al. Deutschmann. *DETCHEM User Manual 2.0.* University of Karlsruhe, 2005.

[26] J. A. Dumesic. Rates of catalytic reactions. In G. Ertl, H. Knzinger, F. Schth, and J. Weitkamp, editors, *Handbook of Heterogeneous Catalysis*, pages 1445–1462. Wiley-VCH, 2008.

[27] J. A. Dumesic, D. F. Rudd, and L. M. Aparicio. *The microkinetics of heterogeneous catalysis*. ACS professional reference book. American Chemical Society, Washington, DC, 1993.

[28] T. Engel and G. Ertl. Molecular-beam investigation of catalytic-oxidation of CO on Pd(111). *Journal of Chemical Physics*, 69(3):1267–1281, 1978.

[29] A. Ern and V. Giovangigli. *Multicomponent Transport Algorithms*. Springer, 1st edition, 1994.

[30] G. Ertl. Oscillatory kinetics and spatiotemporal self-organization in reactions at solid-surfaces. *Science*, 254(5039):1750–1755, 1991.

[31] G. Ertl and P. RAU. Chemisorption and catalytic reactions of oxygen and carbon monoxide on a Palladium(110) surface. *Surface Science*, 15(3):443–&, 1969.

[32] G. H. Evans and R. Greif. Forced flow near a heated rotating disk: A similarity solution. *Numerical Heat Transfer, Part A: Applications*, 14:373–387, 1988.

[33] D. Ferizović, L. K. Hussey, Y.-S. Huang, and M. Muñoz. Determination of the room temperature thermal conductivity of RuO_2 by the photothermal deflection technique. *Applied Physics Letters*, 94(13):131913, 2009.

[34] J.H. Ferziger and H.G. Kaper. *Mathematical theory of transport processes in gases*. North-Holland, 1st edition, 1972.

[35] K. A. Fichthorn and W. H. Weinberg. Theoretical foundations of dynamic Monte-Carlo simulations. *Journal of Chemical Physics*, 95(2):1090–1096, 1991.

[36] E. Fick. *Einführung in die Grundlagen der Quantenmechanik*. Akademische Verlagsgesellschaft Franfurt am Main, 1972.

[37] D. Frenkel and B. Smit. *Understanding molecular simulation : from algorithms to applications*. Academic Press, 1996.

[38] C. W. Gardiner. *Handbook of Stochastic Methods*. Springer, 3rd edition, 2003.

[39] R Gatignol and R Prud'homme. *Mechanical and thermodynamical modeling of fluid interfaces*. Number 58 in Series on advances in mathematics for applied science. World Scientific, 2001.

[40] D. T. Gillespie. A general method for numerically simulating the stochastic time evolution of coupled chemical reactions. *Journal of Computational Physics*, 22(4):403–434, 1976.

[41] D. W. Goodman, C. H. F. Peden, and M. S. Chen. CO oxidation on ruthenium: The nature of the active catalytic surface. *Surface Science*, 601(19):L124–L126, 2007.

[42] D.W. Goodman, C.H.F. Peden, and M.S. Chen. Reply to comment on "co oxidation on ruthenium: The nature of the active catalytic surface" by h. over, m. muhler, a.p. seitsonen. *Surface Science*, 601(23):5663–5665, 2007.

[43] H. Grabert. *Projection Operator Techniques in Nonequilibrium Statistical Mechanics.* Springer, 1st edition, 1982.

[44] P. Hänngi, P. Talkner, and M. Borkovec. Reaction rate theory: fifty years after kramers. *Review of Modern Physics*, 62(2):252–341, 1990.

[45] E. W. Hansen and M. Neurock. Modeling surface kinetics with first-principles-based molecular simulation. *Chemical Engineering Science*, 54(15-16):3411–3421, 1999.

[46] J. Harl and G. Kresse. Accurate bulk properties from approximate many-body techniques. *Physical Review Letters*, 103(5):056401 , 2009.

[47] B. Hendriksen and J. Frenken. CO oxidation on Pt(110): Scanning tunneling microscopy inside a High-Pressure flow reactor. *Physical Review Letters*, 89(4), 2002.

[48] A. C. Hindmarsh. ODEPACK, a systematized collection of ode solvers. In "R. S. Stepleman et al.", editor, *Scientific Computing*, volume 1 of *IMACS Transactions on Scientific Computation*, pages 55–64. North-Holland, 1983.

[49] J.O. Hirschfelder, C.F. Curtis, and R.B. Bird. *Molecular Theory of Gases and Liquids.* Wiley, 1st edition, 1954.

[50] P. Hohenberg and W. Kohn. Inhomogeneous electron gas. *Phys. Rev. B*, 136:864, 1964.

[51] J. Honerkamp. *Stochastic Dynamical Systems: Concepts, Numerical Methods, Data Analysis.* Wiley-VCH, 1993.

[52] Q.-M. Hu, K. Reuter, and M. Scheffler. Towards an exact treatment of exchange and correlation in materials: Application to the CO adsorption puzzle and other systems. *Physical Review Letters*, 98(17):176103, 2007.

[53] R. Imbihl. Nonlinear dynamics on catalytic surfaces: The contribution of surface science. *Surface Science*, 603(10-12, Sp. Iss. SI):1671–1679, 2009.

[54] O. R. Inderwildi. *Multiscale Modelling for Automotive Exhaust-Gas Aftertreatment From the Quantum Chemistry to the Engineering Level.* PhD thesis, Ruprecht-Karls-Universität Heidelberg , 2005.

[55] A. P. J. Jansen. An introduction to Monte Carlo simulations of surface reactions. arXiv:cond-mat/0303028v1, February 2008.

[56] K. F. Jensen, S. T. Rodgers, and R. Venkataramani. Multiscale modeling of thin film growth. *Current Opinion in Solid State and Materials Science*, 3(6):562 – 569, 1998.

[57] R. J. Kee, M. E. Coltrin, and P. Glarborg. *Chemically Reacting Flows.* Wiley, Hoboken NJ, 2003.

[58] R. J. Kee, J. A. Miller, G. H. Evans, and G. Dixon-Lewis. Model of the structure and extinction of strained, opposed flow, premixed methane-air flames. In *Twenty-Second Symposium (International) on Combustion*, pages 1479–1494, 1989.

[59] R. J. Kee, F. M. Rupley, J. A. Miller, M. E. Coltrin, J. F. Grcar, E. Meeks, H. K. Moffat, A. E. Lutz, G. Dixon-Lewis, M. D. Smooke, J. Warnatz, G. H. Evans, R. S. Larson, R. E. Mitchell, L. R. Petzold, W. C. Reynolds, M. Caracotsios, W. E. Stewart, P. Glarborg, C. Wang, and O. Adigun. CHEMKIN collection, release 3.6. Technical report, Reaction Design, Inc., San Diego, CA, 2000.

[60] A. Kendoush. Theory of stagnation region heat and mass transfer to fluid jets impinging normally on solid surfaces. *Chemical Engineering and Processing*, 37(3):223228, 1998.

[61] R. Kissel-Osterrieder. *Ein Konzept zur Schlieung von Druck- und Strukturlücke in der heterogenen Katalyse.* PhD thesis, Ruprecht-Karls-Universität Heidelberg, 2000.

[62] R. Kissel-Osterrieder, F. Behrendt, and J. Warnatz. Detailed modeling of the oxidation of CO on platinum: A Monte Carlo model. *Proceedings of the Combustion Institute*, 27:2267, 1998.

[63] W. Kohn and L. J. Sham. Self-consistent equations including exchange and correlation effects. *Phys. Rev. A*, 140:1133, 1965.

[64] L.P. Lebedev and M.J. Cloud. *Tensor Analysis.* World Scientific, 1st edition, 2003.

[65] I. Levine. *Quantum Chemistry.* Prentice-Hall, Inc., 2000.

[66] R. L. Liboff. *Kinetic Theory.* Springer, 3rd edition, 2003.

[67] D. R. Lide (ed.). *Handbook of Chemistry and Physics.* CRC, 76th edition, 1995.

[68] P.J. Linstrom and W.G. Mallard, editors. *NIST Chemistry WebBook, NIST Standard Reference Database Number 69.* National Institute of Standards and Technology, December 2009.

[69] I. Liu. *Continuum Mechanics.* Springer, 1st edition, 2002.

[70] H. Lynggaard, A. Andreasen, C. Stegelmann, and P. Stoltze. Analysis of simple kinetic models in heterogeneous catalysis. *Progress in Surface Science*, 77:71, 2004.

[71] M. Maestri, D. G. Vlachos, A. Beretta, G. Groppi, and E. Tronconi. A C-1 microkinetic model for methane conversion to syngas on Rh/Al2O3. *AIChE Journal*, 55(4):993–1008, 2009.

[72] A. Majda and J. Sethia. The derivation and numerical solution of the equations for zero Mach number combustion. *Combustion Science and Technology*, 42(3 & 4):185, 1985.

[73] D. Majumder and L. J. Broadbelt. A multiscale scheme for modeling catalytic flow reactors. *AIChE Journal*, 52(12):4214–4228, 2006.

[74] A. L. Marsh1, F. H. Ribeiro, and G. A. Somorjai. Single crystal surfaces. In G. Ertl, H. Knzinger, F. Schth, and J. Weitkamp, editors, *Handbook of Heterogeneous Catalysis*, page 1259. Wiley-VCH, 2008.

[75] M. Marsman, A. Grueneis, J. Paier, and G. Kresse. Second-order Moller-Plesset perturbation theory applied to extended systems. I. Within the projector-augmented-wave formalism using a plane wave basis set. *Journal of Chemical Physics*, 130(18), 2009.

[76] D. Marx and J. Hutter. *Ab initio molecular dynamics : basic theory and advanced methods.* Cambridge Univ. Press, 2009.

[77] R. I. Masel. *Chemical Kinetics and Catalysis.* Wiley-Interscience, 2001.

[78] S. Matera and K. Reuter. First-principles approach to heat and mass transfer effects in model catalyst studies. *Catalysis Letters*, 133:156, 2009.

[79] H. Meskine, S. Matera, M. Scheffler, K. Reuter, and H. Metiu. Examination of the concept of degree of rate control by first-principles kinetic Monte Carlo simulations. *Surface Science*, 603(10-12, Sp. Iss. SI):1724–1730, 2009.

[80] A. Messiah. *Quantum Mechanics*, volume 1 & 2. North-Holland, 1970.

[81] I. Müller. Rational thermodynamics of mixtures of fluids. *Thermodynamics and Constitutive Equations*, page 89184, 1985.

[82] I. Müller. *Thermodynamics.* Pitman Publishing, 1st edition, 1985.

[83] J. K. Nørskov, M. Scheffler, and H. Toulhoat. Density functional theory in surface science and heterogeneous catalysis. *MRS Bulletin*, 31:669, 2006.

[84] National Institute of Standards and Technology. NIST Computational Chemistry Comparison and Benchmark DataBase. online.

[85] H. Over, Y. D. Kim, A. P. Seitsonen, S. Wendt, E. Lundgren, M. Schmid, P. Varga, A. Morgante, and G. Ertl. Atomic-scale structure and catalytic reactivity of the RuO_2(110) surface. *Science*, 287(5457):1474–1476, 2000.

[86] H. Over, M. Muhler, and A. P. Seitsonen. Comment on "CO oxidation on ruthenium: The nature of the active catalytic surface" by d. w. goodman, c. h. f. peden, m. s. chen. *Surface Science*, 601(23):5659–5662, 2007.

[87] C.H.F. Peden and D.W. Goodman. Kinetics of CO oxidation over Ru(0001). *Journal of Physical Chemistry*, 90(7):1360–1365, 1986.

[88] S. Raimondeau and D. G. Vlachos. Recent developments on multiscale, hierarchical modeling of chemical reactors. *Chemical Engineering Journal*, 90(1-2):3 – 23, 2002.

[89] P. B. Rasmussen, B. L. M. Hendriksen, H. Zeijlemaker, H. G. Ficke, and J. W. M. Frenken. The "Reactor STM": A scanning tunneling microscope for investigation of catalytic surfaces at semi-industrial reaction conditions. *Review of Scientific Instruments*, 69(11):3879–3884, 1998.

[90] F. Reif. *Statistische Physik und Theorie der Wärme*. de Gruyter, 2nd edition, 1985.

[91] X Ren, P. Rinke, and M. Scheffler. Exploring the random phase approximation: Application to CO adsorbed on Cu(111). *Physical Review B*, 80(4), 2009.

[92] R. J. Renka. Algorithm 661: QSHEP3D; quadratic Shepard method for trivariate interpolation of scattered data. *ACM Transactions on Mathematical Software*, 14:151, 1988.

[93] R. J. Renka. Multivariate interpolation of large sets of scattered data. *ACM Transactions on Mathematical Software*, 14:139, 1988.

[94] K. Reuter. First-principles kinetic Monte Carlo simulations for heterogeneous catalysis: Concepts, status and frontiers. In O. Deutschmann, editor, *Modeling Heterogeneous Catalytic Reactions: From the Molecular Process to the Technical System*. Wiley-VCH, Weinheim,, 2009.

[95] K. Reuter, D. Frenkel, and M. Scheffler. The steady state of heterogeneous catalysis, studied by first-principles statistical mechanics. *Physical Review Letters*, 93:116105, 2004.

[96] K. Reuter and M. Scheffler. Oxide formation at the surface of late 4d transition metals: insights from first-principles atomistic thermodynamics. *Applied Physics A-Materials Science & Processing*, 78(6):793–798, 2004.

[97] K. Reuter and M. Scheffler. First-principles kinetic Monte Carlo simulations for heterogeneous catalysis: Application to the CO oxidation at $RuO_2(110)$. *Physical Review B*, 73:045433, 2006.

[98] K. Reuter, C. Stampfl, M. V. Ganduglia-Pirovano, and M. Scheffler. Atomistic description of oxide formation on metal surfaces: the example of ruthenium. *Chemical Physics Letters*, 352(5-6):311–317, 2002.

[99] M. Rieger, J. Rogal, and K. Reuter. Effect of surface nanostructure on temperature programmed reaction spectroscopy: First-principles kinetic Monte Carlo simulations of CO oxidation at $RuO_2(110)$. *Physical Review Letters*, 100:016105, 2008.

[100] J. Rogal. *Stability, Composition and Function of Palladium Surfaces in Oxidizing Environments.* PhD thesis, FU Berlin, 2006.

[101] E. Rusli, T. O. Drews, D. L. Ma, R. C. Alkire, and R. D. Braatz. Robust nonlinear feedback-feedforward control of a coupled kinetic Monte Carlo-finite difference simulation. *Journal of Process Control*, 16(4):409–417, 2006.

[102] I. Samohýl. *Thermodynamics of Irreversible Processes in Fluid Mixtures.* Teubner, 1st edition, 1987.

[103] I. Samohýl. Thermodynamics of mixtures of reacting and non-reacting fluids with heat conduction, diffusion and viscosity. *Int. J. Non-Linear Mechanics*, 32:241, 1997.

[104] I. Samohýl. Thermodynamics of reacting mixtures of any symmetry with heat conduction, diffusion and viscosity. *Arch. Rational Mech. Anal.*, 147:1, 1999.

[105] R. Schaback. Reconstruction of multivariate functions from scattered data. online, January 1997.

[106] H. Schade. *Tensoranalysis.* deGruyter, 1st edition, 1997.

[107] F. Schüth, B. E. Henry, and L. D. Schmidt. Oscillatory reactions in heterogeneous catalysis. *Advances in Catalysis*, 39:51, 1993.

[108] C. Stampfl, H. J. Kreuzer, S. H. Payne, and M. Scheffler. Challenges in predictive calculations of processes at surfaces: surface thermodynamics and catalytic reactions. *Applied Physics A-Materials Science & Processing*, 69(5):471–480, 1999.

[109] A. Stierle and A. M Molenbroek. Novel in situ probes for nanocatalysis. *MRS Bulletin*, 32:1001, 2007.

[110] D. R. Stull and H. Prophet. *JANAF Thermochemical Tables.* U.S. Bureau of Standards, Washington D.C., 2 edition, 1971.

[111] I. Szabo and N. Ostlund. *Modern Quantum Chemistry.* Dover Publications, Inc., 1989.

[112] B. Temel, H. Meskine, K. Reuter, H. Metiu, and M. Scheffler. Does phenomenological kinetics provide an adequate description of heterogeneous catalytic reactions? *Journal of Chemical Physics*, 126:204711, 2007.

[113] C. A. Truesdell. Mechanical basis of diffusion. *J. Chem. Phys.*, 37:2336, 1962.

[114] C. A. Truesdell. *Rational Thermodynamics.* Springer, 2nd edition, 1984.

[115] N. G. van Kampen. *Stochastic Processes in Physics and Chemistry.* Elsevier, 1981.

[116] R. A. van Santen and J. W. Niemantsverdriet. *Chemical Kinetics and Catalysis.* Fundamental and Applied Catalysis. Plenum Press, 1995.

[117] A. Varshney and A. Armaou. Multiscale optimization using hybrid PDE/kMC process systems with application to thin film growth. *Chemical Engineering Science*, 60(23):6780–6794, DEC 2005.

[118] D. G. Vlachos. Multiscale integration hybrid algorithms for homogeneous-heterogeneous reactors. *AIChE Journal*, 43(11):3031, 1997.

[119] P. von Rague Schleyer, editor. *Encyclopedia of computational chemistry, 2: E - L.* Wiley, 1998.

[120] A. F. Voter. Introduction to the kinetic Monte Carlo method. In *Radiation Effects in Solids*, page 1–23. Springer, 2007.

[121] M. Votsmeier. Efficient implementation of detailed surface chemistry into reactor models using mapped rate data. *Chemical Engineering Science*, 64(7):1384–1389, 2009.

[122] J. Wang, C.Y. Fan, K. Jacobi, and G. Ertl. The kinetics of CO Oxidation on $RuO_2(110)$: Bridging the pressure gap. *Journal of Physical Chemistry B*, 106:3422, 2002.

[123] C.R. Wilke. A viscosity equation for gas mixtures. *Journal of Chemical Physics*, 18:517, 1950.

[124] K. Wilmański. The thermodynamical model of compressible porous material with the balance equation of porosity. *Transport in Porous Media*, 1(32):21–47, January 1998.

[125] K. Wilmański. *Thermomechanics of Continua*. Springer, 1st edition, 1998.

[126] K. Wilmański. *Continuum Thermodynamics. Part I: Foundations*. World-Scientific, 1st edition, 2008.

[127] D. Zubarev, Vladimir M., and G. Röpke. *Statistical Mechanics of Nonequilibrium Processes*, volume 1 & 2. Akademie Verlag, 1996.

[128] C. Zuppa. Error estimates for modied local Shepards interpolation formula. *Applied Numerical Mathematics*, 49:245259, 2004.